UNIVERSITY OF TWENTE.

Faculty of Electrical Engineering, Mathematics & Computer Science

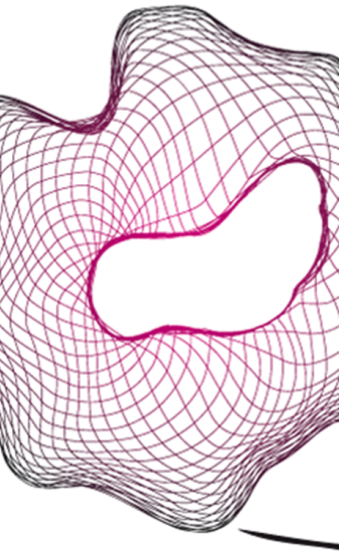

Low frequency DBS-evoked potentials in patients with epilepsy: a sensor and source space analysis

Jill Bay

Master Thesis

Clinical Neurophysiology (CNPH)

01/04/2024 - 09/12/2024

Graduation Committee:
Dr. rer. nat. M.C. Piastra
Dr. ir. T. Heida
Dr. M.C. Tjepkema-Cloostermans

Biomedical Signals and Systems Group
Faculty of Electrical Engineering,
Mathematics and Computer Science
University of Twente
P.O. Box 217
7500 AE Enschede
The Netherlands

Acknowledgements

I feel grateful for the opportunity to work on this project, the things I learned, and the support that I encountered along the way. This project has been an incredible learning experience, including some challenges (and breakthroughs).

First, I would like to thank my daily supervisor, Maria Carla. Your enthusiasm for this project inspired me and was infectious and motivated me throughout. The weekly meetings were not only invaluable in guiding me, but also brought a much-needed sense of positivity. I also want to thank Ciska Heida, the chair of my committee, for taking the time to read my thesis and providing constructive feedback to help refine my work. Finally, I want to thank Marleen Tjepkema-Cloostermans, who joined the committee later in the process, yet still made time to review my thesis and attend my colloquium. All your involvement and support were appreciated.

A big thanks to the Clinical Neurophysiology (CNPH) group! Working together with such welcoming and supportive students has been a privilege. From insightful discussions to small talks and the much-needed coffeebreaks, your support made this enjoyable and invaluable.

Abstract

This study examined low-frequency anterior nucleus of the thalamus (ANT)-deep brain stimulation (DBS) to study the effects of DBS parameters on the evoked potentials (evoked potential (EP)s) in patients with drug-resistant epilepsy (drug-resistant epilepsy (DRE)). The focus was on how DBS parameters (DBS amplitude, DBS contact, and DBS implantation) modulate EPs characterized by EP latency, EP magnitude, and source location. The aim was to investigate the underlying mechanisms of low-frequency ANT-DBS and its impact on related neural networks.

Data were obtained from two subjects participating in the EANSkE study. electroencephalograph (EEG) recordings and T1- and T2-weighted images from two patients were analyzed using advanced preprocessing and source reconstruction techniques. Template subtraction was applied to reduce the DBS artifact, and dipole fitting was used to determine the location at the source level. The effects of DBS amplitude and DBS contact were found through Global Mean Field Power (GMFP) plots, topographical maps, and source-level dipole reconstructions. Anatomical labels for the reconstructed dipoles were assigned using the Brainnetome atlas, providing a detailed location of the source of the corresponding EP components.

The results demonstrated that low-frequency ANT-DBS evokes clear EP components at four latencies: 3-10 ms, 19-26 ms, 37-58 ms, and 55-117 ms. Stimulated deeper (C0 and C1) contacts and higher DBS amplitude produced higher magnitude responses. Source reconstruction revealed a temporal movement of dipoles along structures related to the Papez circuit, e.g. the thalamus, cingulate gyrus, superior frontal gyrus, and basal ganglia. However, some variability was observed in source locations and EP amplitudes, particularly with stimulated superficial (C2 or C3) contacts, or lower DBS amplitude stimulation.

While the findings provide valuable insights, the study also includes limitations. The small sample size, inherent challenges in source reconstruction accuracy, and simplifying assumptions constrain the generalizability of the results. Despite these limitations, the results indicate the importance of DBS parameters in modulating neural activities. Recommendations for future research are comparing low-frequency ANT-DBS results with high-frequency, comparing the dipole fitting results with beamforming or sequential dipole fitting, and comparing the locations of the DBS-evoked responses to epileptic activity maps. This study offers an understanding of the electrophysiological effects of low-frequency ANT-DBS. It emphasizes the potential to influence seizure networks through targeted neuromodulation. These findings contribute to the growing body of evidence on ANT-DBS and provide a basis for further research to optimize the DBS therapy and improve therapeutic outcomes for patients with DRE.

Contents

List of acronyms

AED	anti-epileptic drug
DRE	drug-resistant epilepsy
DBS	deep brain stimulation
VNS	Vagus nerve stimulation
RNS	responsive neurostimulation
ANT	anterior nucleus of the thalamus
EEG	electroencephalograph
MRI	magnetic resonance imaging
EP	evoked potential
FEM	Finite element method
SANTE	Stimulation of the Anterior Nucleus of the Thalamus for Epilepsy
EANSkE	Evaluation of ANT-DBS Neuromodulation with Sensing Electrodes
GMFP	Global Mean Field Power
SNR	signal-to-noise ratio
ECD	equivalent current dipole
CSF	cerebrospinal fluid
STN	sub-thalamic nucleus
RV	residual variance

Chapter 1

Introduction

1.1 Epilepsy

Epilepsy is one of the most common neurological diseases worldwide [1], defined as a neurological disorder by any of the following criteria: 1) at least two unprovoked (or reflex) seizures occurring more than 24 hours apart; 2) one unprovoked (or reflex) seizure with a high probability of additional seizures (at least 60% of the next 10 years); or 3) a diagnosis of an epilepsy syndrome [2]. An estimated 55 million people worldwide are affected by this chronic disease, with each year more than 150,000 diagnoses [3]. A seizure disrupts the regular brain activity caused by excessive neural activity. Both increased action potential firing rates and increased synchronous firing cause this excessive neural activity. Seizures are classified by their onset: focal, generalized, or unknown. A focal seizure begins in one specific part of the brain (e.g., the seizure focus), with the possibility of propagating to other areas of the brain. Neurons positioned in the seizure focus experience high-frequency bursts of action potentials, and, meanwhile, hypersynchronization occurs of the neuronal population [4]. This abnormal activity is usually restricted to the area in which it originated, but during a seizure it can spread due to the failure of inhibitory mechanisms. A generalized seizure starts in both hemispheres when there is no clear seizure focus. The mechanisms underlying this seizure type are not yet well understood. Generalized seizures involve hyperexcitability of neurons throughout the cortex and abnormal behavior in neural networks that connect the thalamus to the cortex [5].

The type of epilepsy a patient has notably influences the treatment approach. The primary treatment modality for epilepsy is anti-epileptic drug (AED). These are typically prescribed after two unprovoked seizures or after a single unprovoked seizure with an increased risk of a second unprovoked seizure [6]. Most AEDs can be used for all types of epilepsy. Certain types of epilepsy, such as temporal lobe epilepsy, require more invasive treatments when seizures persist despite medication, whereas other syndromes, like absence epilepsy, are often well-managed with AEDs alone. Approximately 30%-40% of epilepsy patients do not respond to AEDs [7]. In this case, we speak of DRE, epilepsy that is resistant to medical drugs. People with DRE that have focal epilepsy might, in this case, benefit from surgical resection of the specific brain region if the focal area is not vital for the patient [5]. If surgical resection is not possible or was not effective, invasive neuromodulation techniques can be the following treatment option for DRE. Electrical pulses are delivered to peripheral nerves or targeted brain regions in response to increased rhythmic activity to prevent seizure initiation and/or propagation. The stimulatory pulses can be delivered at a predetermined time (open-loop) or in response to detected seizures (closed-loop). Three such neuromodulation techniques have been approved as epilepsy treatment: Vagus nerve stimulation (VNS), responsive neurostimulation (RNS), and DBS. All three are depicted in Figure 1.1. With VNS (depicted in green), the left vagus nerve

is stimulated via coiled electrodes surgically implanted around the nerve at the height of the neck [8]. RNS (depicted in red) is based on continuously monitoring intracranial EEG at the area of suspected seizure onset [9]. When a possible seizure is detected, a short burst of high-frequency electrical stimulation will be delivered on-site. DBS (depicted in blue) delivers a predetermined, open-loop program of electrical pulses to deep brain structures via implanted electrodes [10]. The variability in patient response to DBS for epilepsy remains largely unexplained, and the exact mechanisms through which DBS reduces seizures are still not well understood.

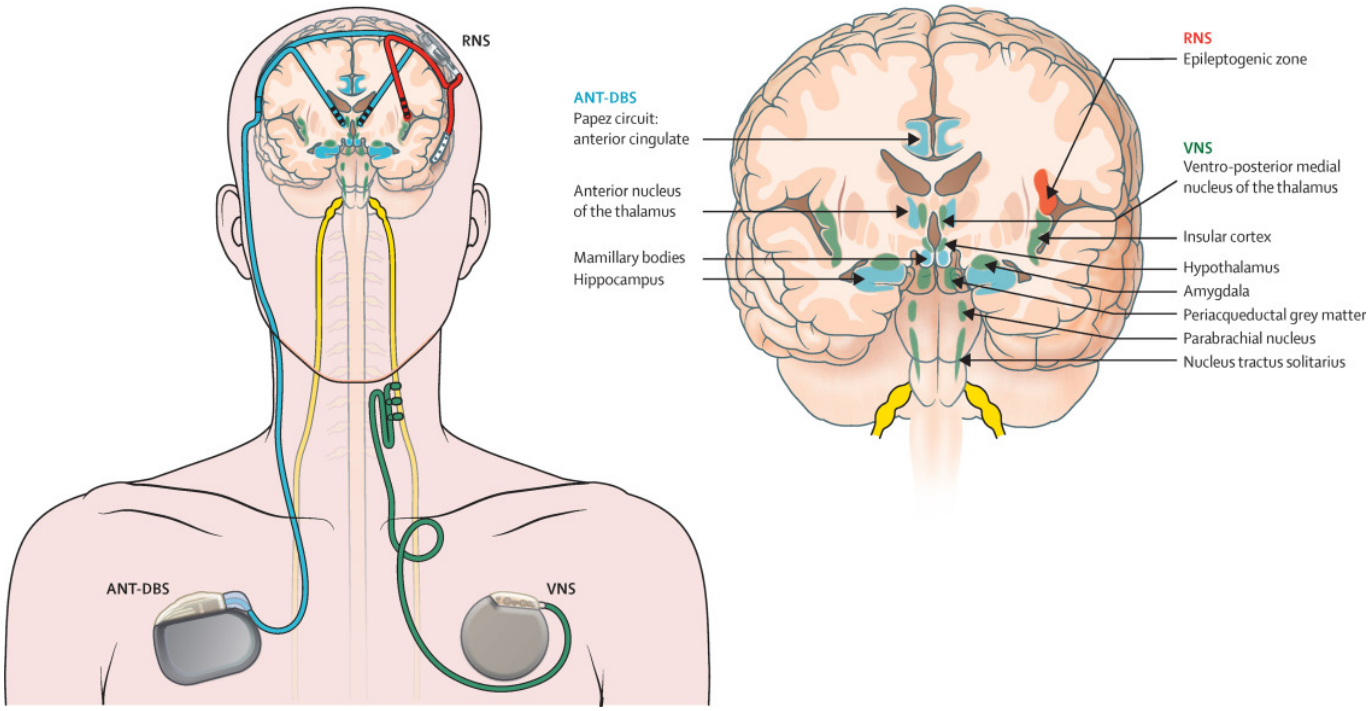

Figure 1.1: On the left panel, a schematic representation of neuromodulation techniques used in epilepsy treatment is visualized [9]. The brain regions involved in the neuromodulation technique are highlighted on the right panel. Blue, green and red represent ANT-DBS, VNS, and RNS, respectively.

1.2 Deep Brain Stimulation (DBS)

Since the 1930s, neuromodulation has been used to explore brain functions and identify potential targets for ablative therapies [11]. This exploratory work laid a foundation that in the late 1980s led to the development of DBS as a treatment for movement disorders, specifically Parkinson's disease [12]. Since then, its application has expanded to include a variety of conditions, including epilepsy [13], depression [14], and obsessive-compulsive disorder [15]. In epilepsy, several target areas have been identified due to their specific roles in seizure networks and their involvement in neural circuits related to seizure propagation. These areas include the anterior nucleus of the thalamus (ANT), the centromedian nucleus of the thalamus (CMT) and the hippocampus. Stimulation of the ANT, a key structure in the Papez circuit, has been primarily targeted for focal epilepsy. The ANT is thought to modulate the spread of seizure activity through its role in integrating and relaying excitatory and inhibitory inputs between the thalamus and cortex. This was supported by the Stimulation of the Anterior Nucleus of the Thalamus for Epilepsy (SANTE) trial, which demonstrated significant seizure reduction in patients with focal epilepsy treated with ANT-DBS [16], [17].

The centromedian nucleus of the thalamus (CMT) has been targeted for generalized epilepsy due to its role in thalamocortical circuits and its involvement in regulating cortical synchronization. This target has been particularly beneficial for patients with generalized tonic-clonic seizures and absence epilepsy, where thalamocortical dysrhythmia is a hallmark feature [18]. The hippocampus is also a key structure in temporal lobe epilepsy, the most common form of focal epilepsy. Hippocampal DBS aims to suppress hyperexcitability in this region, reducing seizure onset and propagation. This target is often chosen when seizures originate from the mesial temporal structures and when surgical resection is not feasible or desirable [18]. Since ANT-DBS is an approved treatment for focal epilepsy and aligns with the goals of this work, we will focus on ANT-DBS from now on.

ANT-DBS delivers a predetermined (open-loop) program of electrical pulses to deep brain structures via implanted electrodes (in the ANT) connected to a pulse generator. This is depicted in blue in Figure 1.1. DBS uses an implantable pulse generator, typically placed under the skin in the chest [19]. This device delivers targeted electrical stimulation to the lead implanted in the ANT. The shape of this stimulus is defined by stimulation parameters, such as the frequency, burst duration, stimulus amplitude, and pulse width [20]. Optimal values for these parameters are patient-specific and are found by trial and error. The clinical standards for using DBS as epilepsy treatment are as follows: high-frequency stimulation ($\geq$ 100 Hz), current amplitude $\geq$ 1V [21].

Research has shown that activity within the Papez circuit, visualized in Figure 1.2, is increased in patients with epilepsy [22]. The Papez circuit is involved in ANT-DBS, also visualized in Figure 1.2. This neural circuit consists of the hippocampus, thalamus, cingulate gyrus, and parahippocampal gyrus and is known for its key role in spatial memory and emotion [23]. It is also believed to be involved in seizure generation and propagation [22], [24], however its precise role in seizure propagation remains a topic of ongoing research. The Papez circuit is structured around two parallel loops: the cingulum bundle and the fornix [25]. The cingulum bundle forms a large loop connecting the prefrontal projections of the cingulate gyrus with the hippocampus in the parahippocampal gyrus of the temporal lobe. Projections from the hippocampus travel to the mammillary bodies via the fornix, which then connect to the ANT through the mammillothalamic tract. The loop completes as the ANT projects to the cingulate gyrus.

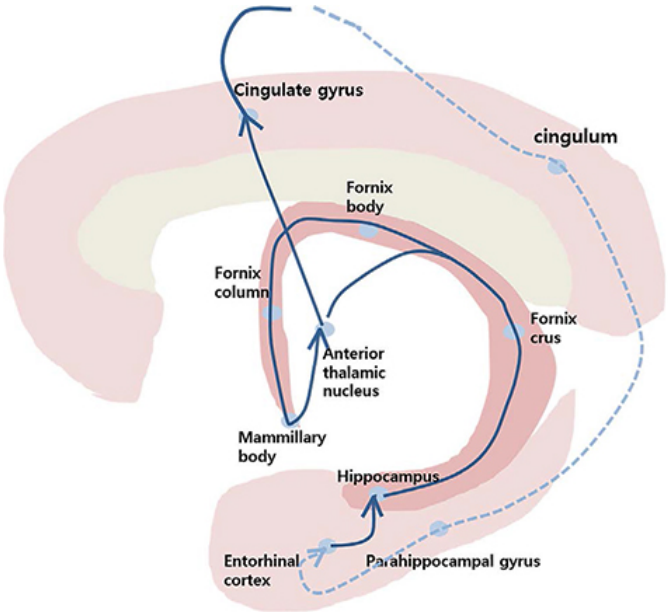

Figure 1.2: Schematic of the pathways included in the Papez circuit [26]. This circuit connects the hippocampus with the cingulate gyrus via the anterior nucleus of the thalamus.

The exact mechanism by which DBS reduces seizure activity is not yet completely understood. Previous research demonstrated that neurostimulation can help disrupt seizure propagation [**?**], [27], or can raise the overall seizure threshold [27]. It seems that patients with partial seizures tend to have a better response to ANT-DBS than patients with generalized epilepsy [28]. A widely accepted theory suggests that an imbalance between excitatory and inhibitory neural activity causes seizures [5], [29], [30]. One hypothesis proposes that ANT-DBS works by restoring this balance between inhibition and excitation [31]. Another possible explanation is that ANT-DBS decreases seizure frequency by disrupting or desynchronizing the network's activity [32].

Research on specifically ANT-DBS as epilepsy treatment is scarce. One study performed ANT-DBS and measured EPs within the circuit of Papez. They concluded that fine-tuning of the contact position of the electrode could improve the efficacy [17]. Another study applied 2 Hz DBS in the ANT, which resulted in strong EPs at 35 and 38 ms after the DBS peak [33]. EPs offer a functional assessment of neural activity (in this case, especially within the circuit of Papez), potentially enhancing the efficacy of ANT-DBS in treating DRE by optimizing the therapeutic approach. Another study compared low-frequency with high-frequency DBS and demonstrated a significantly better seizure reduction for low-frequency ANT-DBS [34]. This emphasizes the need for research regarding low-frequency ANT-DBS.

1.2.1 EEG and DBS

EEG is a powerful diagnostic tool, enabling clinicians to detect abnormal neural activity associated with epileptic seizures. Beyond diagnosis, continuous EEG monitoring can guide the effectiveness of AEDs or help tailor DBS settings by identifying the evoked responses. An EP is a time-locked electrical response of the nervous system to a specific external stimulus, with an amplitude of several microvolts [35]. Unlike random spontaneous activity, EPs are stimulus-specific and reproducible, making them a tool for analyzing neural activity. In epilepsy, EPs serve an important role in understanding and assessing the brain's abnormal electrical activity. This abnormal electrical activity can disrupt the normal sensory processing, often reflected in altered EPs. EPs are a valuable tool in epilepsy research, offering non-invasive means to explore neural activity and evaluate therapeutic efficacy of DBS. By analyzing the location of the EP, clinicians can assess how different brain regions contribute to the generation or propagation of seizures [10]. This can be particularly valuable when planning treatment.

1.3 Source Reconstruction

Source reconstruction is a technique in EEG analysis, enabling the localization of neural activity by unraveling the complex interactions of electrical signals measured on the scalp. Understanding this process starts with the superposition principle, which explains that the overall electrical potential recorded on the scalp is the cumulative effect of multiple active neural sources [37]. When neurons exhibit synchronized activity, it results in current flow throughout the conductive tissues of the head. This process, called volume conduction, enables the spread of electrical currents from the source inside the brain to the scalp. On the scalp EEG, this can be measured by differences in electrical potential between different channels, as depicted in Figure 1.3. To make sense of these signals, topographical maps are created by recording these potentials, representing the spatial distribution of the electrical activity generated by the underlying neural populations at specific points in time [38]. However, because EEG signals are a mix of multiple neural sources, the spatial source of the activity is not directly observable [39]. Source reconstruction aims to reverse the ef-

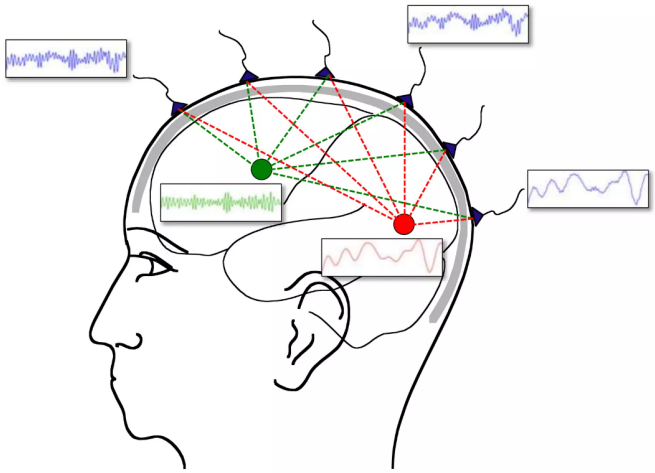

Figure 1.3: Superposition principle of EEG source activity [36]. Activity from both sources (red and green) will be visible at the EEG channels at the scalp.

fects of volume conduction and accurately localize the underlying brain activity coming from the sources. Figure 1.4 gives a general overview of the structure of EEG source reconstruction, including the forward and inverse models.

1.3.1 Processing of Anatomical Data

The first step of the source reconstruction pipeline involves generating a head model, depending on the chosen methodology. The head model can range from a simplified sphere to a highly detailed patient-specific model that accurately reflects the anatomical and electrical properties of the individual's head.

In this study, we opted for a volumetric head model generated through a finite element method (FEM) approach. This method provides accurate representation of the anatomical and electrical properties by accounting for tissue conductivities and detailed geometries of the scalp, skull, and brain. The choice of FEM-based modeling was driven by its ability to handle complex head anatomies and provide higher precision in estimating the spread of neural currents. Using an MRI-based head model was critical for constructing a patient-specific representation, ensuring that the source localization accurately reflects the individual anatomy.

The anatomical features (geometry of the sphere, or scalp, skull, and brain) are combined with electrical properties, including the conductivities of different tissue types (scalp, skull, and brain). These features are needed for modeling how the electric currents generated by the neural sources spread through the head. The EEG electrodes can be aligned and projected onto the surface of the head model. This is referred to as the sensor model and contains information about the spatial configuration of the EEG sensors detecting the activity from the neural sources. Finally, a source model is generated by creating a grid of points within the brain where potential sources of neural activity are estimated.

1.3.2 Processing of Functional Data

Preprocessing the functional scalp-EEG data is an essential step to reduce potential artifacts and enhance the consistency of subsequent analyses by time-locking. Without preprocessing, high-amplitude artifacts could mask the underlying neural signals, leading to distorted results.

In our EEG recordings, the DBS artifact is present, caused by the electrical pulses delivered by the DBS

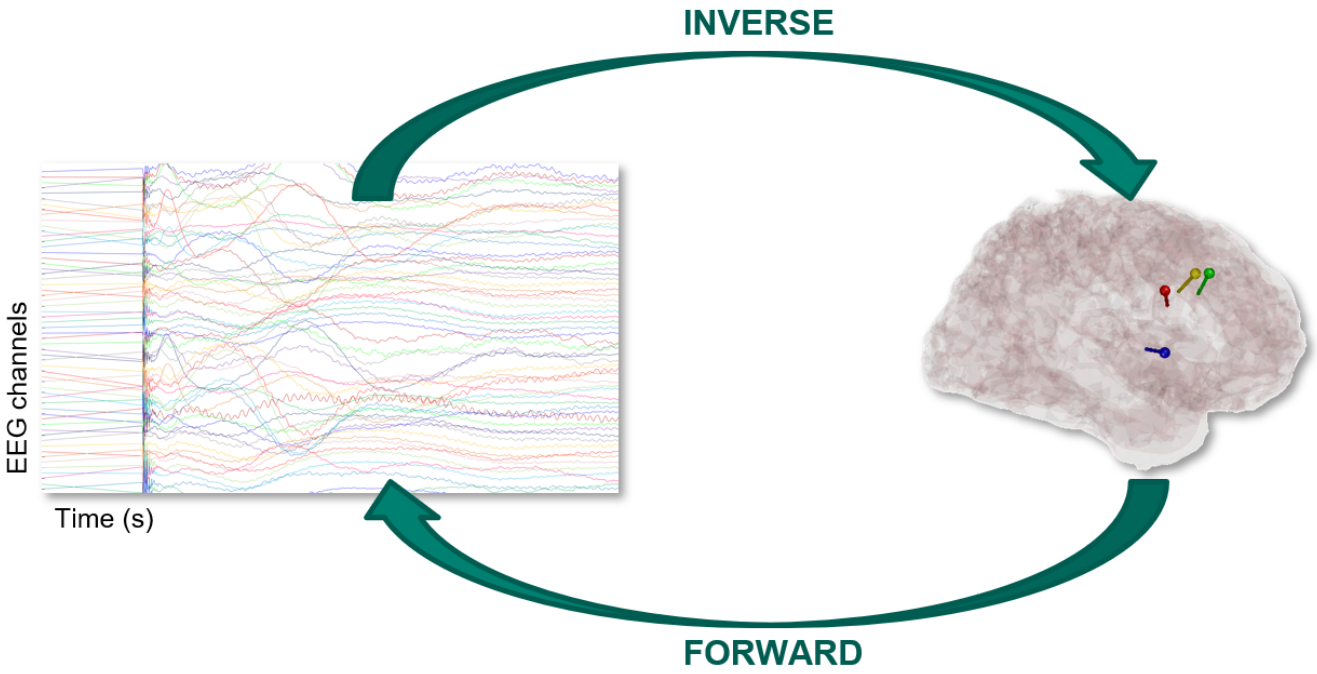

Figure 1.4: Diagram illustrating the EEG forward/inverse problem. To go from the real scalp-EEG (left) to the estimated source in the brain (right), we have to solve the inverse problem. However, to find the solution to this model, we first have to solve the forward model: estimate all the sources in the brain that can model the real EEG.

device. Template subtraction is one method used to reduce this artifact while preserving the possible underlying brain activity. This technique involves creating a time-locked template of the artifact by averaging the EEG signals across multiple stimulation pulses (assuming the artifact is consistent across pulses) [40]. The resulting template is then subtracted from the raw EEG signal. Although this method does not remove the artifact entirely, it reduces its amplitude while preserving the underlying neural activity [41].

Following the artifact reduction, the EEG signal can be analyzed by computing the GMFP, which is the root mean square of the EEG signals across all channels. The GMFP is calculated as follows:

$$\mathrm{GMFP}(t) = \sqrt{\frac{\left[\sum_i^K \left(V_i(t) - V_{\mathrm{mean}}(t)\right)^2\right]}{K}}, \tag{1.1}$$

where t is time, $V_i(t)$ is the voltage at channel i, $V_{mean}(t)$ is the average voltage across all channels, and K is the number of channels. To visualize the spatial distribution of the neural activity, EEG topography can be used. EEG topography is a visual representation of the distribution of electrical activity across the scalp, typically shown as a two-dimensional map [42]. The voltage recorded by the EEG channels is projected onto the 2D surface of the scalp. The potential values between the channels are interpolated to create a smooth map of the activity measured at the scalp.

1.3.3 Forward Model

The forward model is essential for linking neural activity within the brain to the electrical potentials measured on the scalp, forming the foundation of EEG source reconstruction. It simulates how electrical activity in the brain (the sources) generates the potentials that are measured at the scalp via EEG, based on the biophysical properties of the head [43]. The forward model is based on the quasi-static approximation of

Maxwell's equations, which assumes that electromagetic field changes are slow enough to neglect inductive effects. This simplification reduces the equations to focus on the steady-state conduction of electric fields, leading to the Poisson equations that describes how neural activity generates potentials measurable at the scalp:

$$\nabla \cdot (\sigma \nabla \Phi = -\nabla \cdot \mathbf{J}_s, \tag{1.2}$$

where σ is the conductivity of the different tissues in the head, Φ is the scalar electric potential, and $\mathbf{J}_s$ is the current source density generated by the neural activity. The Neumann boundary conditions are applied at the outer surface of the head, stating that there is no current flow normal to the surface:

$$\sigma \nabla \Phi \cdot \mathbf{n} = 0, \tag{1.3}$$

where $\mathbf{n}$ is the unit normal vector to the head's surface.

The Poisson equation (Eq. 1.2) is solved numerically using computational methods. One approach is the Finite element method (FEM), which divides the head model into a mesh of finite elements to handle its complex geometry and varying tissue conductivities [44]. Other methods, such as the boundary element method (BEM), may also be applied depending on the requirements of the analysis. By modeling the propagation of potentials through the head, the forward model provides the foundation for reconstructing the neural sources responsible for the measure scalp EEG signals. In this work, we used a FEM-based approach for solving the forward model. FEM was chosen due to its ability to handle the intricate geometries

Equivalent Current Dipole

In source reconstruction, neural activity is often modeled using simplified source representations, such as the equivalent current dipole (ECD). The ECD approximates the electrical activity generated by neural populations in the brain, where the complex distribution of neural currents is represented by one or more point-like dipoles [39]. These dipoles reflect the effect of synchronous neural activity within a localized region and act as a point source with defined orientation, location, and magnitude, providing a practical approximation of the distributed activity.

1.3.4 Inverse Model

Where the forward model generally describes how neural activity in the brain generates the electrical potentials at the scalp, the inverse model estimates the neural sources (position, orientation, and strength) that are responsible for these observed signals [39]. Unlike the forward problem, which is well-defined, the inverse problem is ill-posed, meaning that there is no unique solution due to the infinite number of source configurations that can explain the recorded EEG data. This problem arises because the EEG recordings represent a superposition of signals from multiple neural sources, each contributing to the measured potential (Figure 1.3). To address this challenge, various techniques apply constraints and assumptions to estimate biologically plausible source distributions. In this study, we applied the dipole fitting method to localize neural activity.

Dipole fitting

The dipole fitting method is a parametric approach used in EEG source reconstruction to identify the best-fitting dipole(s) that account for the recorded neural activity [39], [45]. It is based on the ECD model and

involves finding the optimal dipole position, orientation, and strength by minimizing the difference between the observed data and the signals predicted by a dipole model. Dipole fitting is particularly effective when the sources are expected to be focal, as it provides a practical solution to the ill-posed inverse problem under specific assumptions.

1.4 Objectives

This thesis aims to explore the effects of ANT-DBS on evoked potentials (EPs), focusing on how different stimulation parameters influence electrophysiological responses. The primary objective is to investigate whether and how DBS-induced EPs can be observed and characterized on both the sensor and source levels. The following research questions guide this exploratory study:

1. Do we see DBS-induced evoked potentials on the sensor level?
2. How are these evoked potentials modulated by DBS contact, DBS amplitude, and DBS implantation in both the sensor level and source level?

The expectation is that EPs will be visible in the EEG data. Specifically, early EP components are assumed to originate within the Papez circuit due to its anatomical connectivity and hypothesized involvement in ANT-DBS [17], [33], [46]. While the precise relationship between the Papez circuit and seizure generation remains a topic of ongoing research, its relevance to epilepsy-related networks makes it a plausible source of early EP components.

Furtheremore, the expectation is that EPs will be visible in the EEG data, allowing for characterization of the neural responses. Based on prior studies, the following assumption can be made regarding DBS amplitude: higher DBS amplitude are expected to result in larger EP amplitudes due to increased activation of the neural tissue. Other aspects, regarding the effect of DBS contact and implantation on the EPs, remain exploratory due to a lack of specific literature. This thesis aims to provide preliminary insights into these factors, serving as a foundation for future research.

Chapter 2

Methods

2.1 Data Selection

Data is obtained from the Evaluation of ANT-DBS Neuromodulation with Sensing Electrodes (EANSkE) study [47]. Figure 2.1 provides an overview of the data collection and protocol. The dataset included T1- and T2-weighted magnetic resonance imaging (MRI) scans (pre-operative where available), CT scans post-implantation, and EEG measurements at different time points. Specifically, we analyzed data from bilaterally implanted DBS electrodes across two patients (DBS011 and DBS014): implantation 1 (DBS011, right shaft), implantation 2 (DBS011, left shaft), implantation 3 (DBS014, right shaft), and implantation 4 (DBS014, left shaft). Two datasets were used for analysis: EEG recordings `s000840` from patient `DBS011` and `s000842` from patient `DBS014`, as well as corresponding T1- and T2-weighted images and CT scans.

The first EEG was measured before implantation to establish a baseline. After implantation, three additional EEG measurements were performed at specified intervals (2 months, 12 months, and 24 months after implantation). During these post-implantation sessions, a specific stimulation protocol was implemented. This protocol included both high- and low-frequency (6 Hz) stimulation. For low-frequency stimulation, adjustments were made to the DBS contact (C0, C1, C2, C3) and the DBS amplitude (high = 5V or low = 2.5 V). In this study, only the effects of low-frequency DBS were analyzed, focusing on the variations in stimulation parameters.

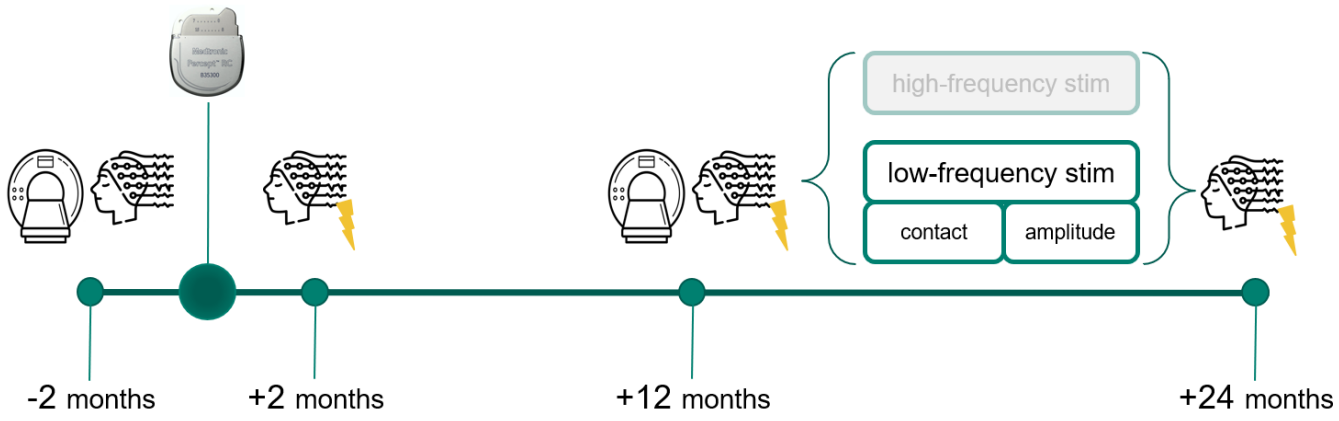

Figure 2.1: Overview of the protocol of the EANSkE study. MRI scans are made once before and once after DBS implantation. Four EEG measurements are performed, one baseline (before implantation) and three times after implantation during the DBS.

For the low-frequency stimulation (6 Hz), the DBS contact (C0, C1, C2, C3), DBS amplitude (high/low), and the DBS implantation (left/right) were modified. This protocol is reflected in the EEG signal, for example, as visible in the M2 channel shown in Figure 2.2. Monopolar stimulation was used, with the implanted pulse generator serving as the anode and a single electrode contact point (C0, C1, C2, C3) programmed as a cathode.

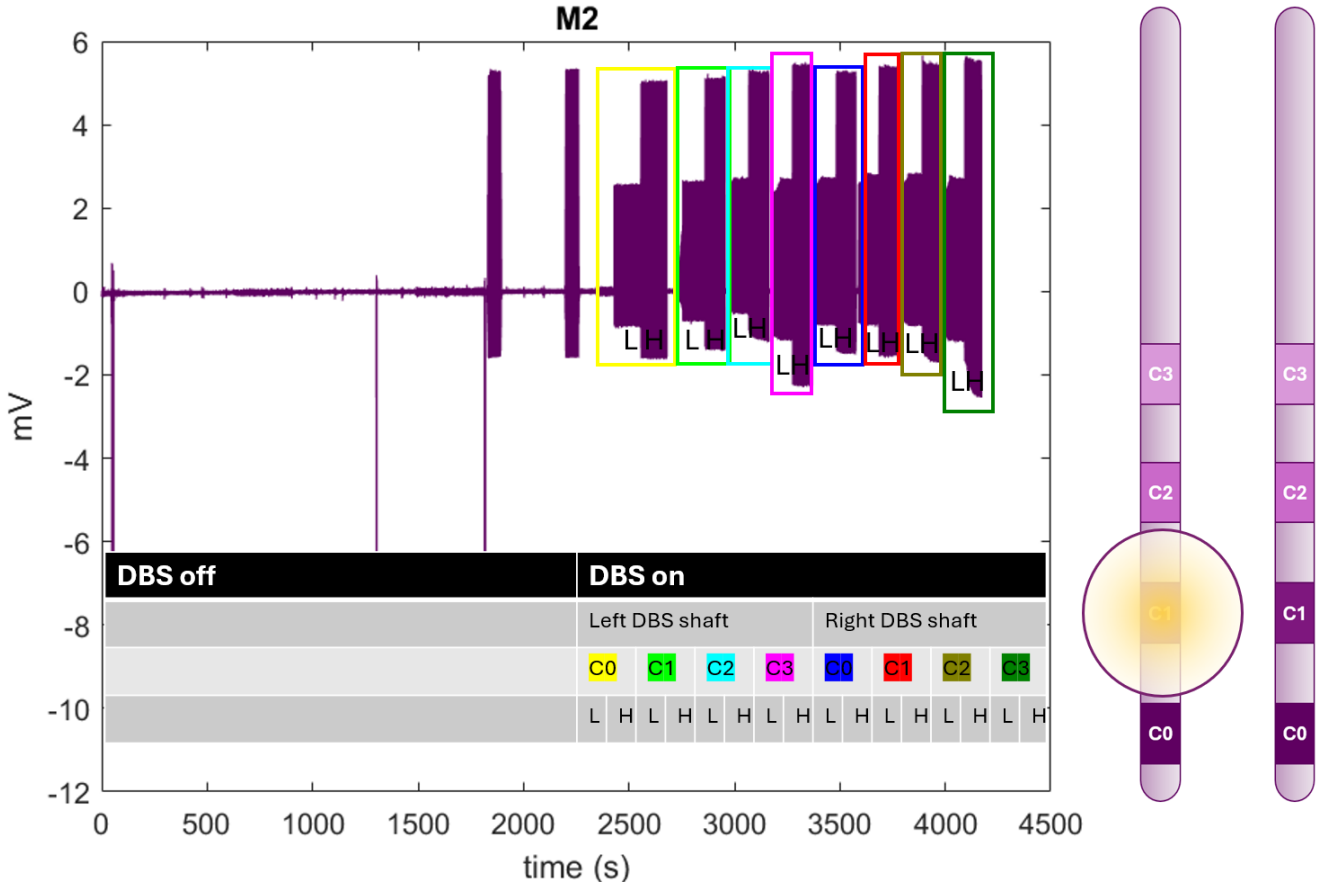

Figure 2.2: Left: the EEG signal from the M2 channel, showing segments corresponding to different DBS stimulation settings as defined by the protocol. **Right**: a schematic of the DBS implantation, highlighting the four electrode contacts (C0, C1, C2, C3).

2.1.1 Materials

The EANSkE study uses the Medtronic Model 3389 leads connected to the Medtronic Percept PC Neurostimulator with BrainSense Technology. A 64-channel cap with a 10/20 configuration was used for the EEG measurement.

Code is available through the

2.2 Source Reconstruction

Figure 2.3 visualizes the source reconstruction pipeline. All processing is done using MATLAB © (R2022b) using the FieldTrip (20240326) software toolbox [36]. All analyses are done in native space (`ras` coordinate system), except if stated otherwise.

2.2.1 Processing of Anatomical Data

The first step of the source reconstruction pipeline is processing anatomical and spatial data to generate a head model, align the EEG electrodes, and create a source model, each of which will be discussed in this section. Before generating the head model, we removed facial features from the T1- and T2-weighted MRI to anonymize the dataset.

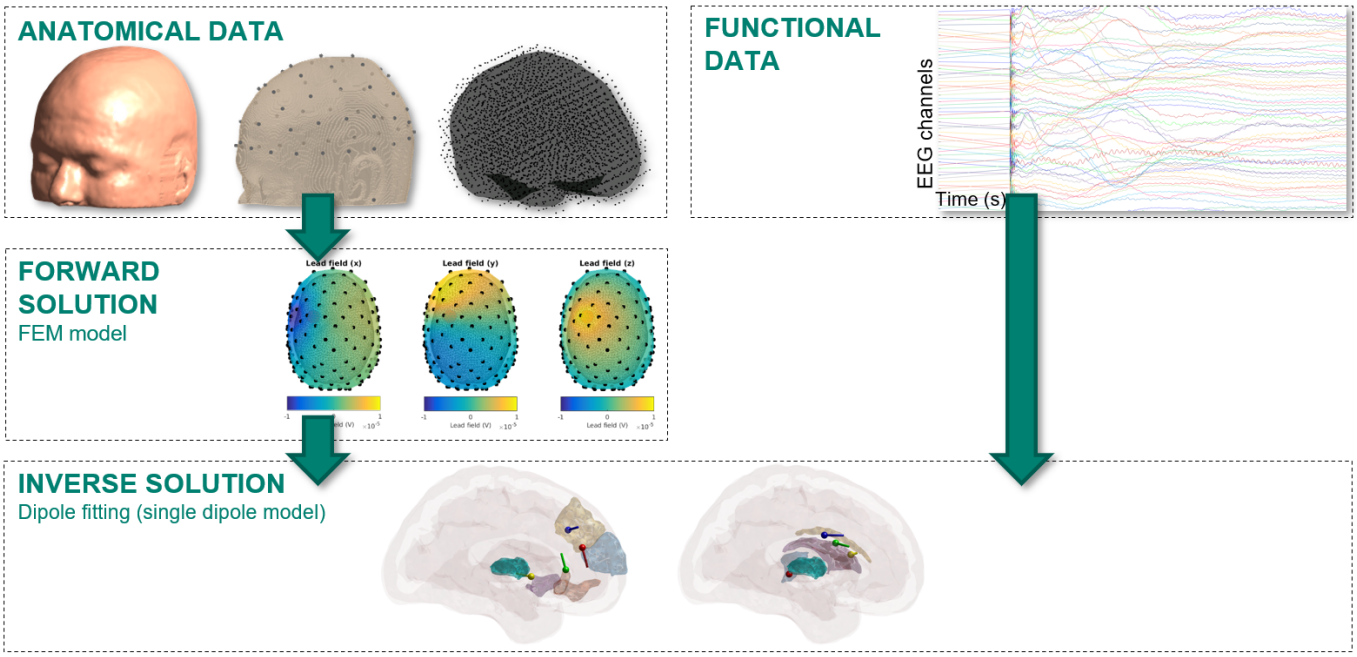

Figure 2.3: Source reconstruction pipeline. Pre-processing of the T1- and T2-weighted data results in the head model, sensor alignment, and source model. These components are used to calculate the forward solution numerically using the FEM method. The leadfield, describing the relation between the source activity within the brain and the EEG measurements, is derived from the forward solution. The inverse solution is then calculated using the pre-processed EEG data and the leadfield. The method used is dipole fitting.

Head Model

The T1- and T2-weighted MRI images are used as input for the SimNIBS © function `charm` for generating the head model [48]. This process involves segmenting the anatomical data to identify different tissue types within the head, including: gray matter, white matter, cerebrospinal fluid (CSF), scalp, eyeballs, compact bone, spongy bone, blood, and muscle. We labeled regions not assigned to a specific tissue type (representing air or small gaps) as an additional tissue with conductivity 1e-6 S/m for physical plausibility and to use for further modeling. Following segmentation, we generated a 3D tetrahedral volumetric mesh, with all tetrahedral elements assigned to the corresponding tissue label from the segmentation. We generated the head model by assigning specific conductivity values (Table 2.1) to each tissue compartment in the tetrahedral mesh, using the *SimBio* method implemented in FieldTrip. This head model provides the foundation for the FEM calculations in the forward model.

Table 2.1: Segmented tissue structures and corresponding conductivity values, based on SimNIBS [48].

Segmented Tissue	Conductivity Values (S/m)
White Matter	0.126
Gray Matter	0.275
CSF	1.654
Holes	1e-6
Scalp	0.465
Eye Balls	0.5
Compact Bone	0.008
Spongy Bone	0.025
Blood	0.6
Muscle	0.16

Sensor Alignment

A template 10-20 electrode configuration, adapted for use with the TMSi EEG cap, was loaded and manually aligned to the subject-specific head model to generate the sensor model. This template is personalized for the specific EEG cap that was used in this study. To minimize spatial error between the electrodes and the scalp, we projected the aligned sensors directly onto the scalp of the head model before performing the forward computations.

Source Model

The source model is generated by calculating the centroids (geometric centers) of each tetrahedral element in the head model, and by selecting only those located in the gray matter. Selecting only gray matter sources ensures that the dipole sources are placed in anatomically realistic locations where neural activity is likely to originate. To accommodate computational limitations and time constraints, the source model was reduced to 30% of the original sources, resulting in a final source model that included $\pm$350.000 sources.

2.2.2 Pre-processing of Functional Data

The functional EEG data was pre-processed in several steps to prepare the signal for the source reconstruction, where the continuous EEG signals from all channels (10-20 electrode system) were included. First, we re-referenced the data to the common average to ensure that each channel's signal was compared to the global activity across all channels. We applied demeaning to all channels to remove any baseline shifts in the data, centering the data around zero and improving the signal-to-noise ratio (SNR) for subsequent analyses. We visually inspected the data to identify the DBS artifact. Peaks corresponding to the DBS artifacts were detected using the M2 channel and were based on amplitude threshold ($\geq$ 1.5 μV) and minimum peak distance ($\geq$ 5 samples). Once the DBS peaks were detected, we defined trials around each peak, with a window extending 30ms before and 145 after the DBS pulse. The pre-stimulus period serves as a baseline and 30 ms is long enough to establish a stable baseline without taking prior neural activity into account. The post-stimulus period includes the expected responses to the DBS. In 145 ms, both early and late EP components can be captured. Following the trial definition, we visually inspected the data for remaining artifacts. We manually rejected channels or trials with clear noise to ensure that only clean data were used for

subsequent analyses. We excluded the EMG channels from further analysis, because they do not measure brain signal. We performed time-lock analysis on the epoched data to extract the time-locked averages for each channel. Baseline correction was applied using a pre-stimulus window of -30ms to -5ms to remove any low-frequency drifts or baseline shifts in the data. This results in a set of average signal across trials, showing the response to DBS at each EEG channel. To summarize the overall brain response to DBS, the GMFP was calculated across all channels and the topography at a preset time point.

Template Subtraction

The template subtraction method is based on a previous paper, where linear interpolation is applied to the initial part of the signal, and template subtraction is used in the last part [40]. We created the template by averaging the M1 and M2 channels from the passive recovery phase until the end of the epoch. Then, the relative error (*RE*) between the individual EEG channels and the artifact template was calculated. We found the scaling factor (*SF*) by subtracting *RE* from 1 and is then multiplied by the template. We then subtracted this *SF* from the EEG data. Finally, we applied linear interpolation to the pre-stimulus period (-30 to 0 ms) of the signal right before the artifact. For stimulation at the second DBS shaft implantation, an artifact was observed at 83ms after the DBS peak. This artifact was distinct from the primary DBS artifact and affected the signal visibly. To address this, we applied linear interpolation within the time window $[82.75, 86]$ ms after the DBS peak to remove this second artifact.

Selection of EPs

The selection of the EP latencies for analysis was based on the GMFP plots. We visually inspected the plots individually, to identify peaks or features that resemble peaks, such as a broad fluctuation. The identified peaks were noted down, documenting the specific EP latencies. These latencies were subsequently used in further analysis to examine the spatial and temporal dynamics of the EPs.

2.2.3 Forward Model

We chose the FEM method to numerically solve the quasi-static Maxwell's equations for each source position, which is implemented into the *SimBio* method used to generate the head model [44]. We, then, calculated the forward solution, called the leadfield matrix. Calculating the leadfield matrix for this source model required approximately 8 hours of computation. We used the calculated leadfield matrix to solve the inverse problem and reconstruct the dipole sources.

2.2.4 Inverse Model

Dipole Fitting

To solve the inverse model and find the optimal dipole position, orientation, and strength, the function `ft_dipolefitting` was used, which initiated a grid search to find the approximate location and was followed by linear optimization to refine the parameters and minimize the residual variance between the modeled and measured (EEG) data. We calculated a single dipole per selected EP, with the underlying assumption that a single dipole can explain the EEG data at each time point.

Anatomical Labels of the Dipoles

The FSL segmentation and the Brainnetome atlas were used to assign anatomical labels to the dipoles. The FSL segmentation is an automatic segmentation consisting of 55 tissues containing subcortical as well as gray and white matter structures. The Brainnetome atlas contains a more detailed parcellation with 246 distinct (sub)cortical regions, ensuring more accurate anatomical labeling.

The Brainnetome atlas is not in the native coordinate system but in the MNI (Montreal Neurological Institute) coordinate system. In order to use this atlas, we had to transform the dipole coordinates from native to MNI space. First, a mask was created of all structures included in the Brainnetome atlas, which was then converted to a volumetric mesh. We applied a transformation matrix to map the dipole coordinates from native to MNI space. Finally, the MNI coordinates of the dipoles were mapped to the Brainnetome atlas voxel space to assign anatomical labels corresponding to the regions in the atlas. We cross-verified the labels using both the FSL segmentation and the Brainnetome atlas to support the transformation to the MNI coordinate system and ensure accuracy.

2.3 Presentation of the Results

The data consisted of: implantation 1 (DBS011 stimulating right DBS shaft), implantation 2 (DBS011 stimulating left DBS shaft), implantation 3 (DBS014 stimulating right DBS shaft), and implantation 4 (DBS014 stimulating left DBS shaft). For each implantation, the stimulation was performed at both high- and low-amplitude DBS and across all four electrode contacts (C0, C1, C2, and C3).

Before the analysis, the data were selected based on their GMFP plots. The effects of the DBS amplitude (high vs. low) were analyzed across 10 parameter configurations: implantation 1 (stimulation at C0, C1, and C2 for both high and low amplitude), implantation 3 (stimulation at C0, C1, C2, and C3 for both high and low amplitude), and implantation 4 (stimulation at C0, C1, and C2 for both high and low amplitude, and C3 for high amplitude). The data from implantation 2 (all configurations), as well as implantation 1 (stimulation at C3 under both high and low amplitude) were excluded from further analysis, because the GMFP showed weak responses below 1 μV which is less reliable for further interpretation.

Further selection on topographies ensured suitability for the dipole fitting method. Finally, we evaluated the dipoles using the RV, calculated using the following formula:

$$\mathrm{rv} = \frac{\sum_{i=1}^{N}(d_{1,i} - d_{2,i})^2}{\sum_{i=1}^{N} d_{1,i}^2}, \tag{2.1}$$

where N is the total number of data points, i is the index for each point, $d_{1,i}$ represents the measured data, and $d_{2,i}$ represents the modeled data. If the residual variance is high, this indicates that the dipole did not sufficiently explain the data.

To present the results of the effects of DBS on the EPs, this section is structured according to the key aspects: EP components, Papez circuit, DBS amplitude, DBS contact, DBS implantation.

EP Components

The GMFP plots were used to provide an overview of the EP magnitude and the EP latency on the sensor level. Topographic maps displayed the spatial distribution on the scalp at the specific time points. At the source level, reconstructed dipoles were visualized and mapped onto the Brainnetome atlas to associate

dipole locations with specific brain regions. Highlighted subregions indicated the anatomical location of the dipole sources.

Papez Circuit

To investigate whether the reconstructed dipoles followed a sequential pattern, we analyzed the dipoles that were reconstructed across the entire time series for each implantation. The temporal dynamics of the reconstructed dipole movement and clustering were then used to assess the pathway that was followed.

DBS Amplitude

To investigate the effects of high- and low-amplitude DBS, the GMFP plots, topographic maps, and source-level dipole reconstructions were compared across conditions. Changes in EP magnitude and EP latency, as well as the dipole location and orientation were analyzed for both amplitudes to assess how DBS amplitude influences evoked responses.

DBS Contact

Stimulations at different contacts (C0, C1, C2, and C3) were analyzed to evaluate the effects of contact location on EP. The GMFP plots, topographies, and source-level data were used to determine differences in EP latency and EP magnitude, and the source locations.

DBS Implantation

Data from four implantations across two patients were analyzed. Each implantation was assessed for EPs. GMFP plots, topographies, and the reconstructed source locations were analyzed to study the effect of the DBS implantation on the evoked responses.

2.4 Validation

Several methods were applied to validate the source reconstruction results. To validate the accuracy of the source reconstruction (the dipole fitting method), the dipole corresponding to the DBS artifact was computed. We determined the exact location of the DBS electrodes using Lead-DBS, which provides precise anatomical localization of the electrode contacts and is known to be within the ANT [49]. This is visualized in Figure 2.4. We then compared the reconstructed dipole location to the exact electrode location computed by Lead-DBS by calculating the Euclidean distance between the centroid of the DBS contact and the dipole.

To validate the latency of the EP components observed in the source-reconstructed signal, we analyzed the neural pathway derived from the reconstructed dipoles across the entire time series. The pathway of neural activity was determined by tracking the sequence of reconstructed dipoles within the time window 30.5 - 79 ms after the DBS artifact. This included identifying the transitions between key regions, such as the thalamus and the superior frontal gyrus, based on the anatomical labels through the Brainnetome atlas. We calculated the Euclidean distance between successive dipoles locations along the pathway, and determined the total pathway length by summed these distances. The observed timing for the reconstructed source to propagate along the pathway was determined by measuring the time difference. The conduction

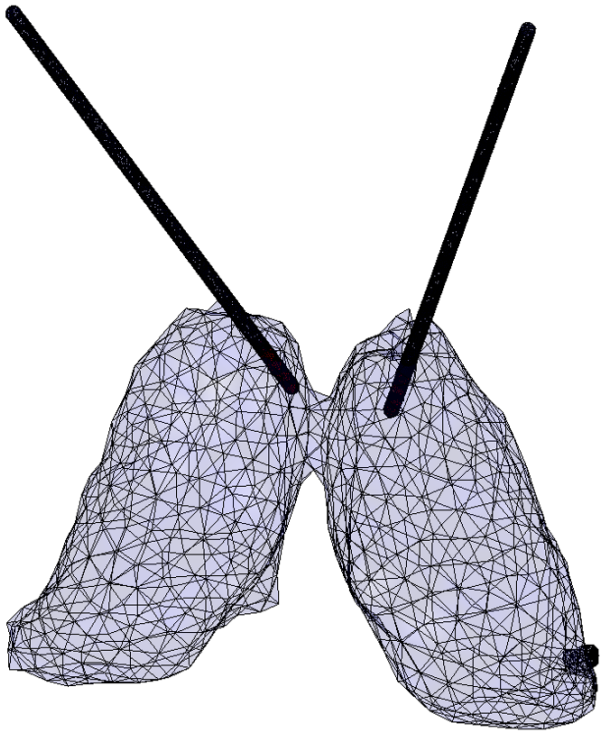

Figure 2.4: Left: visualization of bilateral DBS electrodes within the segmented thalamus. Right: same image, rotated and zoomed in, to show the contacts highlighted in red along each lead.

velocity for each pathway segment was calculated using the formula $v = \frac{\text{distance}}{\text{time}}$. We compared the observed conduction velocities against known physiological values to confirm the plausibility of the EP latencies.

To validate that sources within deeper brain structures can generate measurable scalp-EEG signals, we estimated the dipole strength required to produce the observed potentials at a specific EEG channel. The Euclidean distance between the dipole source and the EEG channel was calculated. An estimate for average conductivity is used $\sigma = 0.33$ S/m. We calculated the dipole strength using the formula $Q = \frac{\Phi \cdot r}{\sigma}$, where Q is the dipole strength (Am), Φ is the measured potential at the EEG channel (V), r is the Euclidean distance between the dipole and the scalp channel (m), and σ is the conductivity (S/m). We compared the dipole strength then to a suggested dipole moment to assess plausibility.

Chapter 3

Results

This chapter provides an overview of the analysis pipeline and the outcomes of varying DBS parameters. It starts with a detailed walkthrough of the analysis pipeline, using a single parameter configuration (implantation 1: high amplitude stimulation at C0) as an illustrative example. Then, the focus will shift to the key findings across all analyzed configurations. This includes a detailed exploration of EP components, the dipoles and related Papez circuit, and the effects of varying the DBS amplitude, contact, and implantation side. Parameter-specific results are summarized to highlight trends and variations, with supporting and data provided in Appendices D, **??**, and E.

3.1 Processing of the Anatomical Data

Following segmentation of the anatomical data using the SimNIBS function `charm`, the T1- and T2-weighted MRI scans were processed to identify distinct tissue types within the brain and surrounding structures. Figure 3.1 illustrates the segmentation outcome for subject 11, where the major anatomical structures are distinguished. Although the scans were anonymized, default facial features remain visible. These are generic and distinct from the subject's actual facial features, to guarantee anonymity while preserving anatomical accuracy.

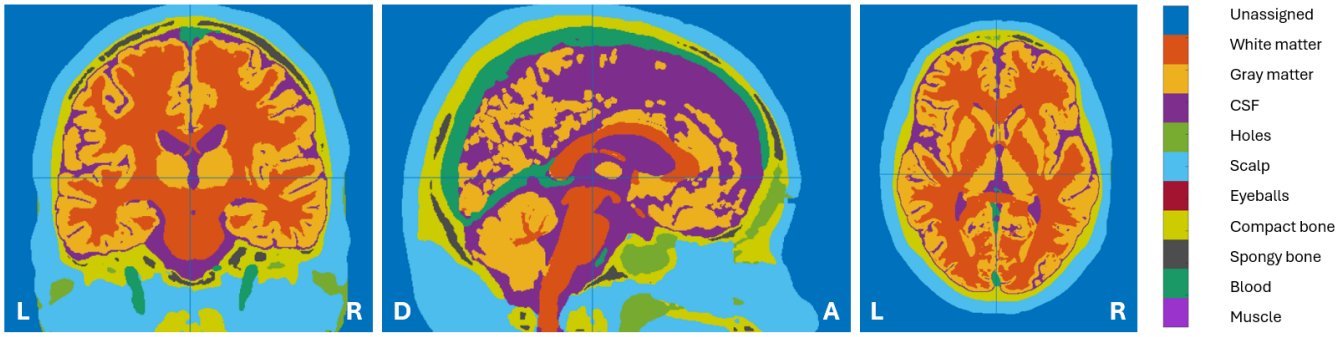

Figure 3.1: Segmentation of subject 11 using the T1- and T2-weighted MRI scan based on the SimNIBS.

3.2 Processing of the Functional Data

In Figure 3.2, the processed EEG signals are presented, with blue lines representing the individual EEG channel responses and the red line indicating the GMFP. The data were preprocessed as described in the

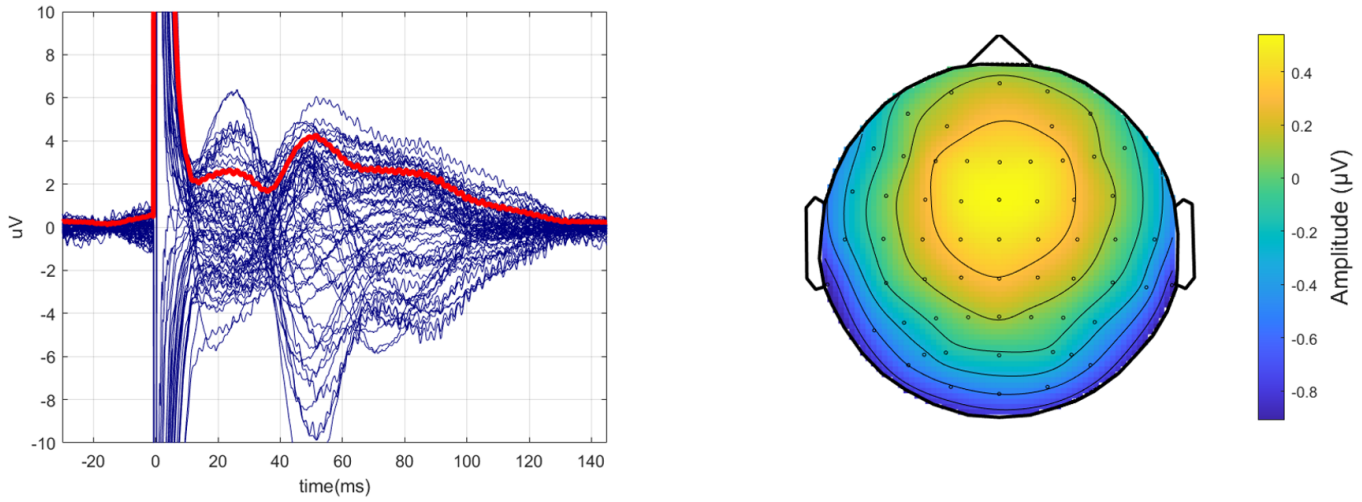

Figure 3.2: Left: GMFP of the EEG signal including the DBS artifact, so before artifact reduction. Individual channel signals are shown in blue, and the GMFP across the channel is highlighted in red. **Right**: topographical plot of the EEG amplitude distribution at 1 ms. Warmer colors indicate higher amplitude values, showing the centralized artifact distribution on the scalp.

Methods section (2.2.2, including trial selection, baseline correction, and averaging over trials. The data reveal a prominent artifact, around $t = 0$, that exceeds the amplitude of the physiological neuronal signals. An EP with multiple long-latency components is observed at different latencies: 20 ms, 53 ms, and 78 ms after the DBS peak. The topography at $t = 1$ ms in Figure 3.2 (right) shows the DBS artifact's spatial characteristics measured across the scalp.

After applying the template subtraction, the DBS artifact is reduced, revealing an additional short-latency EP component at $t = 10$ ms, depicted in Figure 3.3. The previously observed components (at 20 ms, 53 ms, and 78 ms) remain unaffected by the template subtraction. The topography at $t = 1$ shows a different spatial pattern compared to the topography including the DBS artifact.

In Figure 3.4, the topographies of the EP components at each latency are visualized. These topographies illustrate distinct spatial distributions compared to the initial artifact map at 1 ms (3.2 right). The observed spatial distributions at 10 ms, 20 ms, 53 ms, and 78 ms reflect the progression of the neuronal response over time.

3.3 Forward Model

The leadfield matrix was computed to map the relationship between dipole sources within the brain and the EEG potentials measured by the scalp-EEG. The leadfield describes how a unit-strength dipole at a given location and orientation on the scalp-EEG. Figure 3.5 shows the leadfield generated for a single selected dipole location within the brain and modeled for three orthogonal orientations (x, y, and z). The leadfield matrix contains scalar values representing the potentials at each EEG channel resulting from this unit-strength dipole.

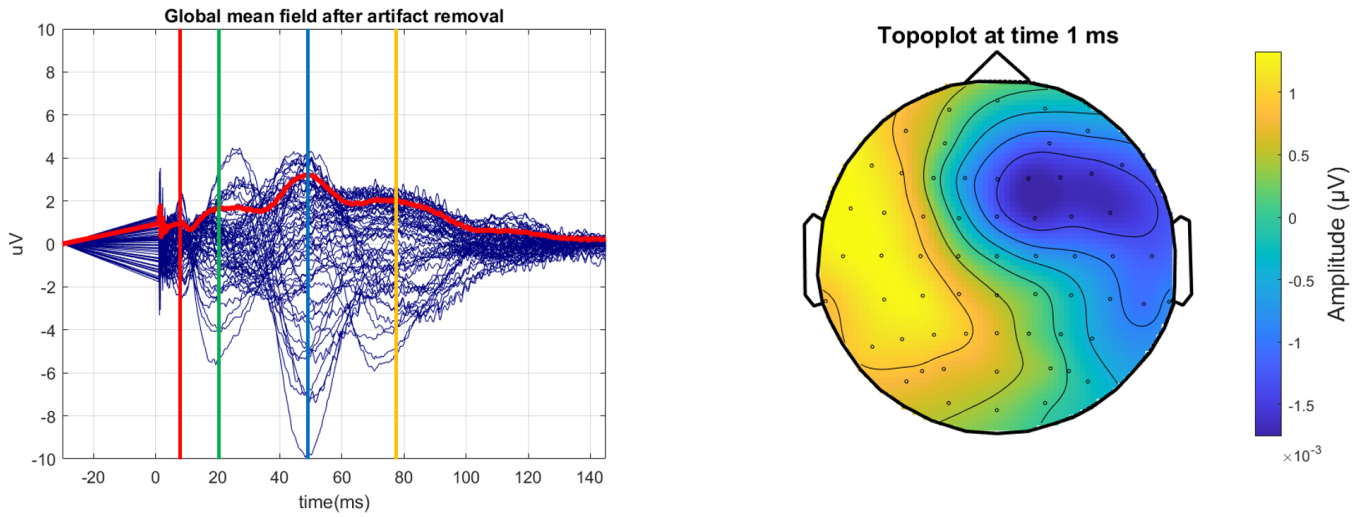

Figure 3.3: (**left**) GMFP of the EEG signal after artifact reduction. Individual EEG channel signals are shown in blue, and the GMFP is highlighted in red. Vertical lines highlight the key latency markers at which EP components occur: red (10 ms), green (20 ms), blue (53 ms), and yellow (78 ms). (**right**) Topographical map of EEG amplitude at 1 ms. Warmer colors represent higher amplitude values.

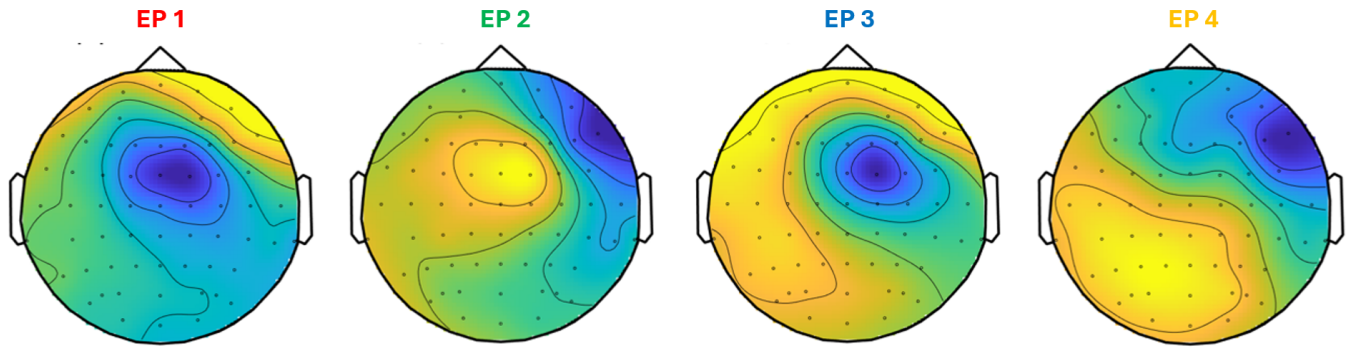

Figure 3.4: Topographical maps of the four EP components identified in the GMFP in Figure 3.3 after artifact attenuation.

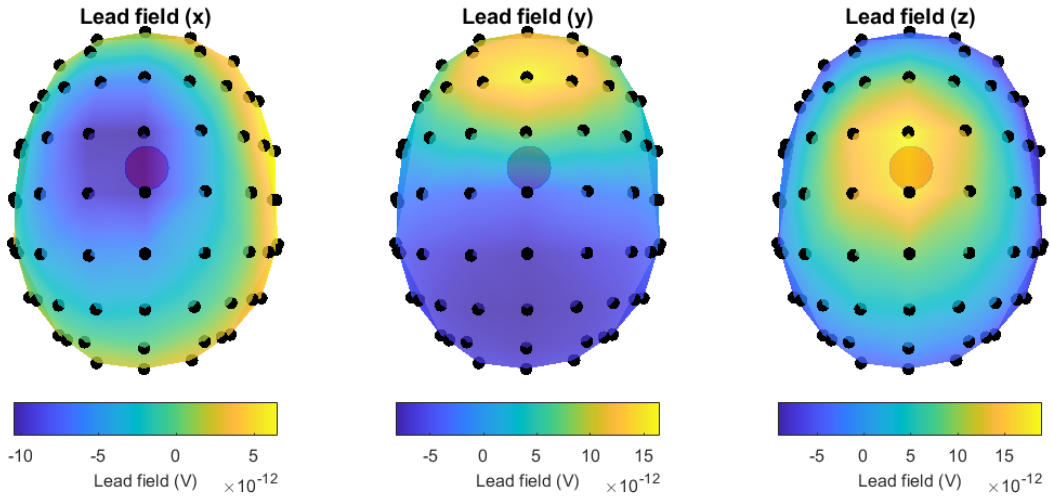

Figure 3.5: Topographical maps of the lead field components for a unit-strength dipole at a selected location, oriented along the x- (left), y- (middle), and z-axis (right). The maps depict the distribution of scalar potentials (in volts) across the scalp as recorded by the EEG channel.

3.4 Inverse Model

The dipole fitting method localized the dipole sources responsible for the observed EEG, providing information on their position, orientation, and strength within the gray matter.

Table 3.1: Anatomical labels of the reconstructed dipoles corresponding to each DBS contact and EP component, based on SimNIBS segmentation, FSL segmentation, and the Brainnetome Atlas.

Contact	EP	SimNIBS	FSL Segmentation	Brainnetome Atlas
C0	**EP 1**	Gray Matter	Right Cerebral Cortex	Right Cingulate Gyrus rostroventral area 24
	EP 2	CSF	Right Cerebral Cortex	Right Superior Frontal Gyrus medial area 9
	EP 3	Gray Matter	Right Cerebral Cortex	Right Basal Ganglia, Nucleus Accumbens
	EP 4	Gray Matter	Left Cerebral Cortex	Left Superior Frontal Gyrus dorsolateral area 8

Table 3.1 summarizes the anatomical labels assigned to the reconstructed dipoles for each DBS contact and EP component, derived from the SimNIBS segmentation, FSL segmentation, and the Brainnetome atlas. SimNIBS segmentation, containing ten different tissue types, primarily identifies tissues as gray matter, or cerebrospinal fluid (CSF). The FSL segmentation consistently, containing 55 tissue types, categorizes the surrounding areas as various cerebral structures, including the right and left cerebral cortex and white matter (WM) regions. The Brainnetome atlas provides more detailed anatomical labels for cortical and subcortical regions and comprises 246 labels. This atlas includes specific areas of the superior frontal gyrus, cingulate gyrus, basal ganglia, and thalamus. Some EP components do not have identifiable labels within the Brainnetome atlas.

Figure 3.6 illustrates the locations of the reconstructed dipole sources in the brain, displayed in the lateral, coronal, and sagittal views. Each dipole was assigned an anatomical label using the Brainnetome atlas, and the corresponding surface mesh of the assigned region was generated. These surface meshes, representing (sub)cortical structures, are visualized together with the overall cortical surface. The dipoles corresponding to the four EP components are color-coded: the first EP component (red) is located in the right cingulate gyrus, the second (green) in the right superior frontal gyrus, the third (blue) in the right nucleus accumbens, and the fourth (yellow) in the left superior frontal gyrus. The temporal progression of the EP components is visualized in this figure from early (red) to late (yellow).

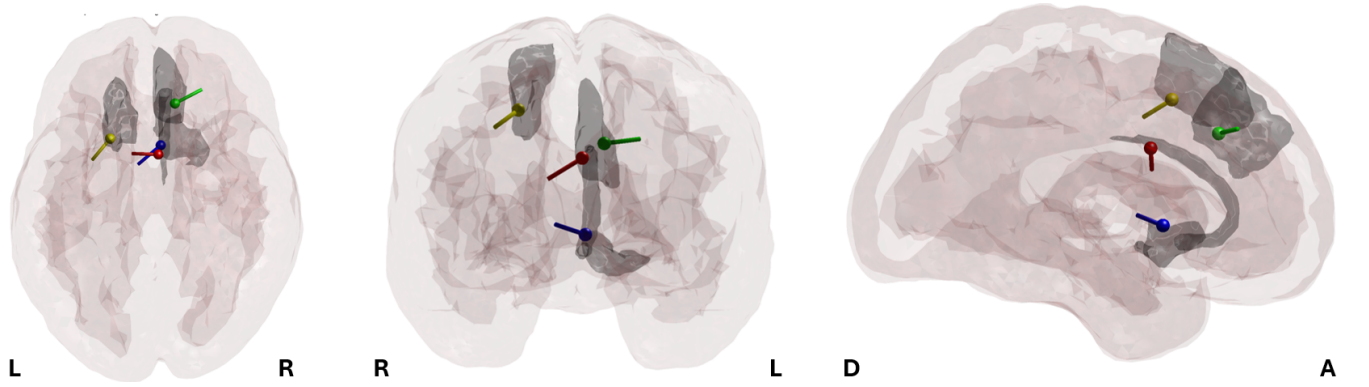

Figure 3.6: Visualization of the reconstructed dipole source locations (red, green, blue, yellow) in response to DBS stimulation, including the meshes of the cortical structures (black). Left, middle, and right correspond to lateral, coronal, and sagittal views, resp.

3.5 Presentation of the Results

The DBS parameters (amplitude, stimulating contact, and implantation side) were varied and compared across conditions. This section highlights the key findings from the analyses of the DBS parameters. Examples of parameter configurations are presented, and the overall results across all data are summarized. Additional figures of all parameter configurations are provided in Appendices D, C, and E.

A clear overview of the GMFP plots together with the topographical maps at the different EP latencies is visualized in Appendix C. In general, all topographies are smooth, and appear to be visually dissimilar from the DBS artifact (Figure 3.2, left). It should be noted that the colorbar is not fixed across the different topographies, resulting in intensity representation. As a result, although the color patterns may visually appear comparable across maps, the actual intensity values are not directly comparable.

The reconstructed dipoles are plotted within a mesh including the (sub)cortical regions of the Brainnetome atlas, in Appendix E. Figure 3.7 contains the color coding of the dipoles: EP component 1 (red), 2 (green), 3 (blue), and 4 (yellow). The brightness of each color corresponds to the specific stimulating contact: the brightest color represents stimulating C0. Each lighter shade signifies a more superficial contact point, with stimulating C3 being the lightest shade (most transparent) dipole.

Contact	Evoked potential				
		EP 1	EP 2	EP 3	EP 4
	C0	Dipole	Dipole	Dipole	Dipole
	C1	Dipole	Dipole	Dipole	Dipole
	C2	Dipole	Dipole	Dipole	Dipole
	C3	Dipole	Dipole	Dipole	Dipole

Figure 3.7: Table including the color coding of the reconstructed dipoles.

The final dataset for analysis included configurations with GMFP responses $> 1\mu$V). The following parameter configurations were included: implantation 1, stimulation at C0, C1, and C2 for both high and low amplitude; implantation 3, stimulation at contacts C0, C1, C2, and C3 for both high and low amplitude; and implantation 4, stimulation at contacts C0, C1, and C2 for both high and low amplitude and C3 for high amplitude.

EP components

The general latencies across parameter configurations are EP component 1 at 3-10 ms; EP component 2 at 19-26 ms; EP component 3 at 37-58 ms; and EP component 4 at 51-117 ms. The EP latencies are summarized in tables per parameter configuration in Appendix A.

In general, the sources at the defined EP latencies are located around the thalamus. This is best visible in implantation 1 (stimulating C0 contact at high DBS amplitude), visualized in Figure 3.8. The behavior is broad and extends to the cortical structures (the cingulate gyrus and superior frontal gyrus). For implantation 3 and 4, the behavior is mainly constrained to the subcortical regions (basal ganglia and thalamus). This is visualized in Figure 3.9, where the sources are located within the basal ganglia (EP component 3 located within the cingulate gyrus). The pre-frontal regions of the thalamus are highlighted in cyan, to resemble the ANT that is located within these regions.

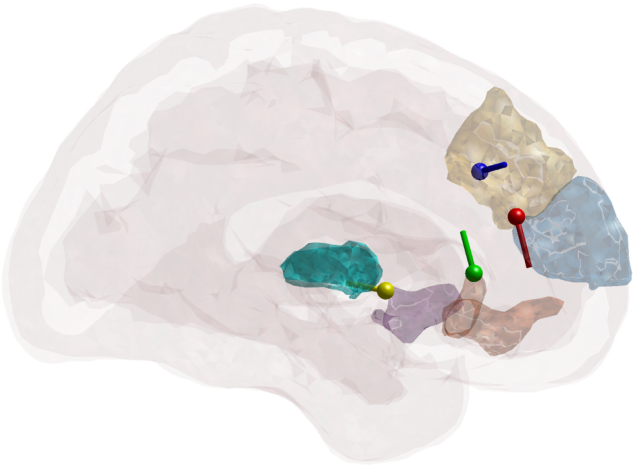

Figure 3.8: Brain mesh including the reconstructed dipoles (red-green-blue-yellow) corresponding to the EP components (1-2-3-4) of implantation 1 (C0 high amplitude). The regions highlighted include the thalamus, cingulate gyrus, and superior frontal gyrus. In cyan, the pre-frontal regions of the thalamus are visualized.

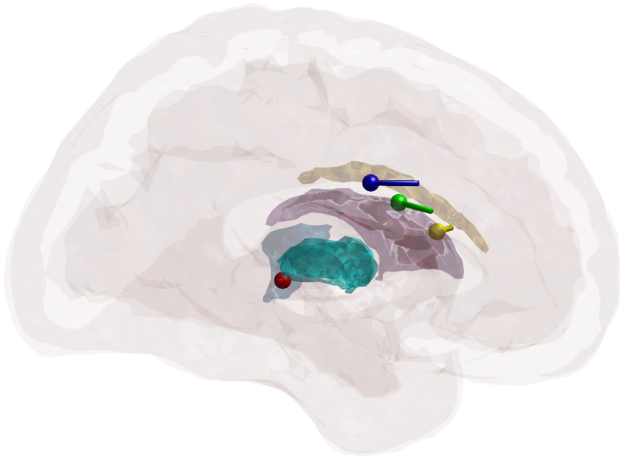

Figure 3.9: Brain mesh including the reconstructed dipoles (red-green-blue-yellow) corresponding to the EP components (1-2-3-4) of implantation 3 (C1 high amplitude). The regions highlighted include the thalamus, caudate nucleus, and cingulate gyrus. In cyan, the pre-frontal regions of the thalamus are visualized.

Papez Circuit

In Figure 3.10, all reconstructed dipoles across the entire time series for implantation 1 (stimulation at C1 with high amplitude) are visualized. The clustering of dipoles around specific anatomical regions is visible, with distinct colors representing the clusters within different structures. The dipoles show a clear temporal and spatial pattern, clustering primarily around the thalamus and adjacent regions related to the Papez circuit. A sequential activation pattern over time is indicated: right thalamus (30-37 ms) $\rightarrow$ right cingulate gyrus (37-43 ms) $\rightarrow$ right superior frontal gyrus (43-58 ms) $\rightarrow$ right cingulate gyrus (58-63 ms) $\rightarrow$ right caudate nucleus (63-65 ms) $\rightarrow$ right thalamus (65-70 ms) $\rightarrow$ right nucleus accumbens (70-79 ms) $\rightarrow$ left ventral caudate ($80-88$ ms) $\rightarrow$ left cingulate gyrus ($88-97$ ms) $\rightarrow$ left superior frontal gyrus ($97-103$ ms) $\rightarrow$ left dorsal caudate ($112-116$ ms) $\rightarrow$ left thalamus ($117ms$). After the first 80 ms after the DBS peak, the dipoles are located in the exact same structures, but in the left hemisphere. Note that there are

some time points in between the left superior frontal gyrus (79 - 103 ms) and the left dorsal caudate (112 - 116 ms). This is because between 103 - 112 ms the dipole location switches between those two regions. For all other time windows, the dipoles are clustered within this structure.

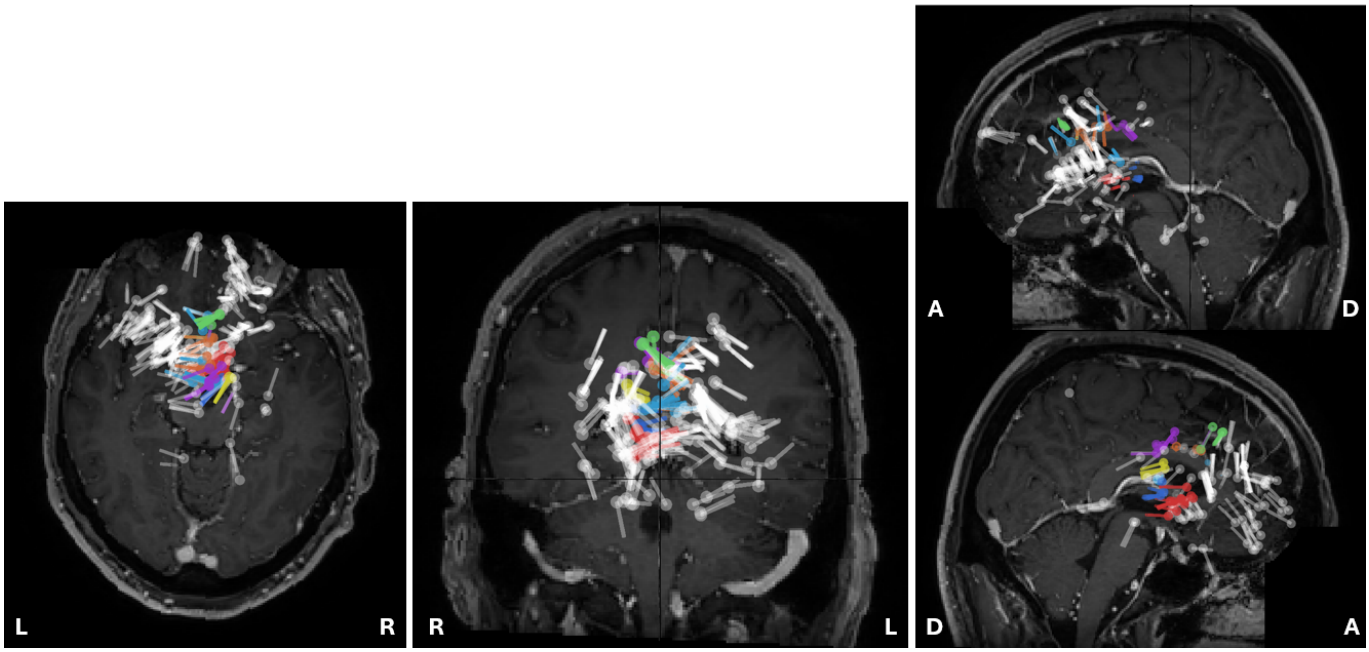

Figure 3.10: Plot of all reconstructed sources over the entire time-series for implantation 1 (stimulating C1 contact at high amplitude), overlaid on the T1-weighted image for axial (left), coronal (middle), and sagittal (right). The dipole colors teal, orange, green, purple, yellow, blue, and red correspond to clusters within the thalamus, cingulate gyrus, superior frontal gyrus, cingulate gyrus, caudate nucleus, thalamus, and nucleus accumbens, respectively. White corresponds to not-clustered dipoles.

The dipoles across the entire time-series were plotted for implantation 1, 3, and 4 (stimulating C1 contact at high amplitude). The results of the movement of the dipole source over time is depicted in Figure 3.11. For implantation 3, the dipole locations do not follow such a distinct pattern as with implantation 1, but they are clustered in the following (sub)cortical structures over time: left/right thalamus, left/right cingulate gyrus, left/right dorsal caudate, right superior frontal gyrus, and right nucleus accumbens. Implantation 3 shows the temporal dipoles from Figure 3.11 (middle) for time window 55-105 ms. For implantation 4, the anatomical labels corresponding to the clustered dipoles also form a pattern: within the time period of 30 - 110 ms after the peak, all dipoles are clustered in the left dorsal caudate. Other regions where the dipoles are clustered are left/right cingulate gyrus, left superior frontal gyrus and left/right thalamus. The time window selected for implantation 4 is 1-118 ms.

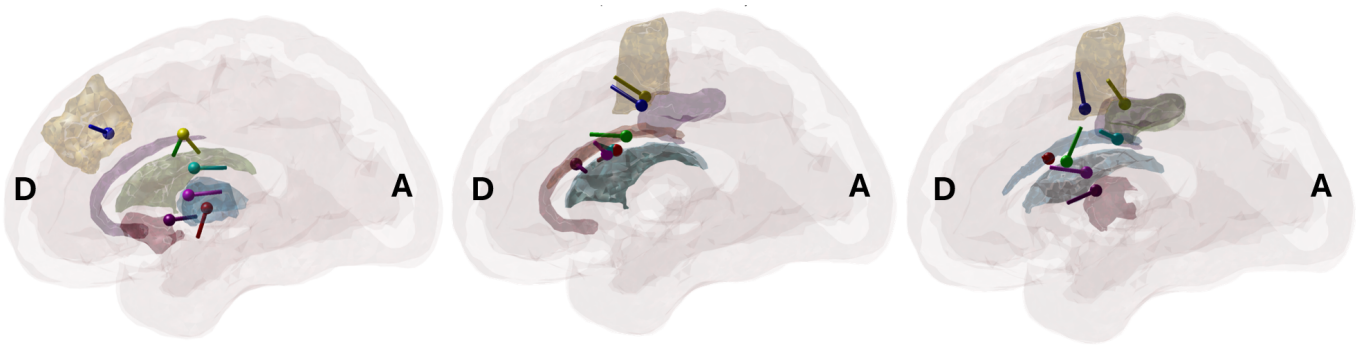

Figure 3.11: The clustered source reconstructed dipoles reduced to one dipole per cluster for implantation 1 (left), 3 (middle), and 4 (right). The colors show the temporal evolution in the following order: red-green-blue-yellow-cyan-magenta-purple.

Figure 3.12 illustrates the GMFP and RV values for implantations 1, 3, and 4 (stimulation at C1 with high amplitude). The RV values represent the goodness-of-fit of every reconstructed dipole over the entire time-series. For implantation 1, the clustered dipole sources are found within the time period of 30.5 - 79 ms. The RV values are all (≤ 0.2) within this period. For implantation 3, the RVs are ≤ 0.2 for the entire time-series. For implantation 4, the RV values are ≤ 0.1 for the majority of the time-series, with a small peak around 15 ms up to RV $= 0.2$.

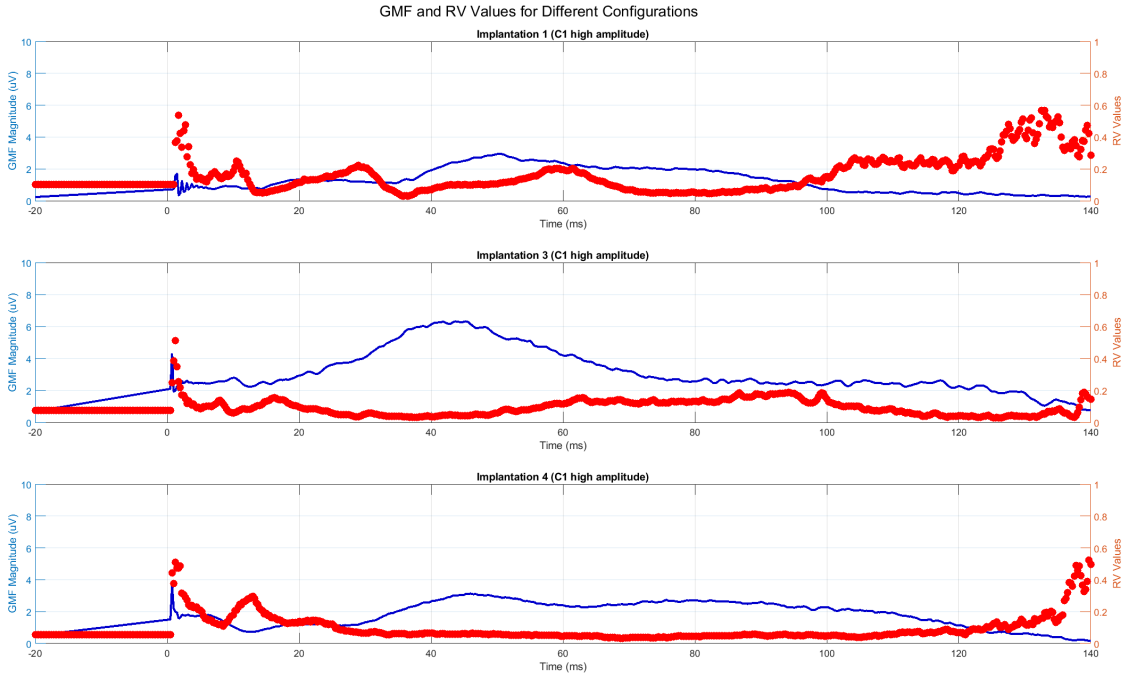

Figure 3.12: GMFP together with the RV across implantation 1 (top), 3 (middle), and 4 (bottom).

The RV per reconstructed dipole source are summarized in Appendix B per parameter configuration.

DBS amplitude

The effects of DBS amplitude (high vs. low) on the GMFP were analyzed across all four implantations (2 implantations per subject), and their GMFPs are visualized in Appendix **??**. These figures demonstrate that

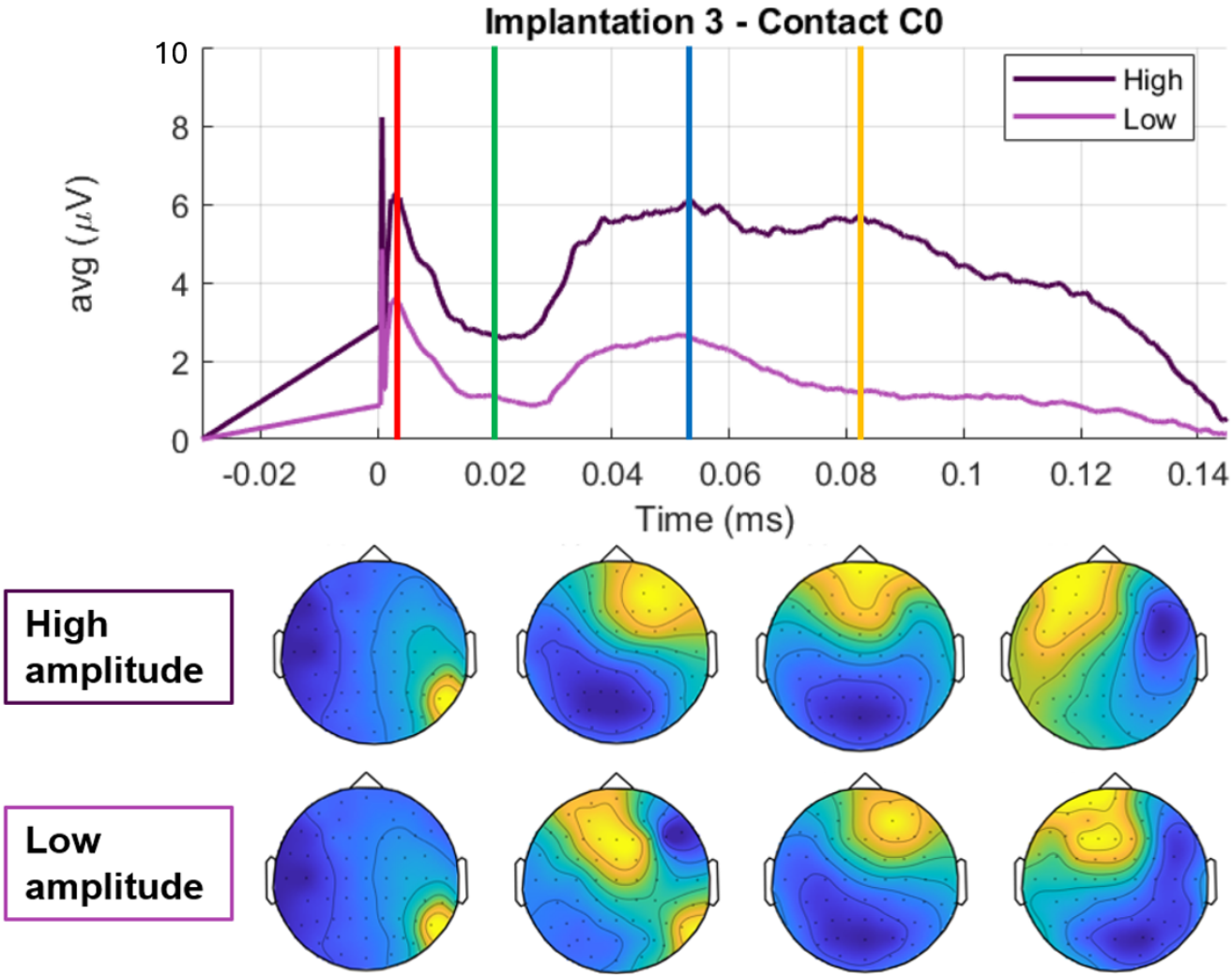

Figure 3.13: Top: GMFP plot for implantation 3 (stimulation at C0) at high (purple) and low (pink) amplitude DBS. Marker lines indicate the EP components at different latencies. Bottom: topographical maps show measured potential at the scalp at these latencies.

the DBS amplitude does not affect the EP latency; there are no shifts in latencies between the high and low amplitude stimulation.

In the same figures, it is visible that the high DBS amplitude generally produced a more extensive response magnitude across all contacts, but especially at the deeper contacts (C0 and C1). For the more superficial contacts (C2 and C3), the low amplitude stimulation evoked such a small magnitude response, making it barely distinguishable from noise (C.1 implantation 1 - contact C2 and C.2 implantation 3 - contact C2 and implantation 4 - contact C3).

The results indicate that, in general, higher DBS amplitude consistently increases the EP magnitude across all analyzed configurations (10/10). Additionally, DBS amplitude showed to have no effect on the EP latency in the majority of the configurations (8/10). Exceptions are observed at implantation 1 (stimulation at C0) and implantation 3 (stimulation at C3). The topographies, in general, show dissimilar patterns (27/40).

Figure 3.13 visualizes the GMFP of implantation 3 (stimulation at C0) for high vs low DBS stimulation. The EP components at the different latencies are indicated by the vertical lines. This figure illustrates that the EP latency is not modulated by the DBS amplitude. Furthermore, the data indicate that a higher DBS amplitude evokes a higher magnitude response than the low amplitude stimulation. The topographies

below the GMFP plot illustrate the spatial distribution of the EP components at different latencies. The topographies for EP component 1 and 3 show similar spatial distributions, while those for 2 and 4 show distinct patterns.

Reconstructed dipole source analysis showed that high amplitude DBS resulted in sources within the subcortical regions (27), such as the caudate nucleus (18) and the thalamus (5), based on Tables F.1, F.3, F.4, F.5. Sources within the cortical structures (17) were located within the cingulate gyrus (9) and the superior frontal gyrus (4). In contrast, low amplitude DBS resulted in a more balanced distribution with 18 sources located within the cortical structures, such as the cingulate gyrus (11) and 20 sources located within subcortical regions, such as the caudate nucleus (16).

The results indicate that for 7/40 cases, the source location remained consistent between high and low DBS amplitude, with all other parameters fixed. The locations were similar for the following parameter configurations: implantation 3 (C1 EP component 2, C2 EP component 1), and implantation 4 (C0 EP component 1, 2, and 3, C1 EP component 3, and C2 EP component 3). However, for the remaining cases, the source location differed.

Comparing the topographies in D.5 and D.6 reveals that the topographies appear visually similar for stimulation at C0 (EP component 1, 2, and 4) and at C1 (EP 1 and 2). For these cases, the response measured at the scalp was similar in spatial distribution. In Figure 3.14, the reconstructed dipole sources corresponding to stimulation at C0 and C1 are visualized. The dipoles that are bright-colored correspond to high DBS amplitude, and the light-colored dipoles to low amplitude. This figure illustrates that the red dipoles (EP component 1) appear to have similar location and orientation, as well as the blue dipoles (EP component 3). The yellow dipoles (EP component 4) appear have a similar location for C0 at high amplitude and C1 at low amplitude. Although the topographies of EP component 2 exhibit similarities, the dipole source locations are not.

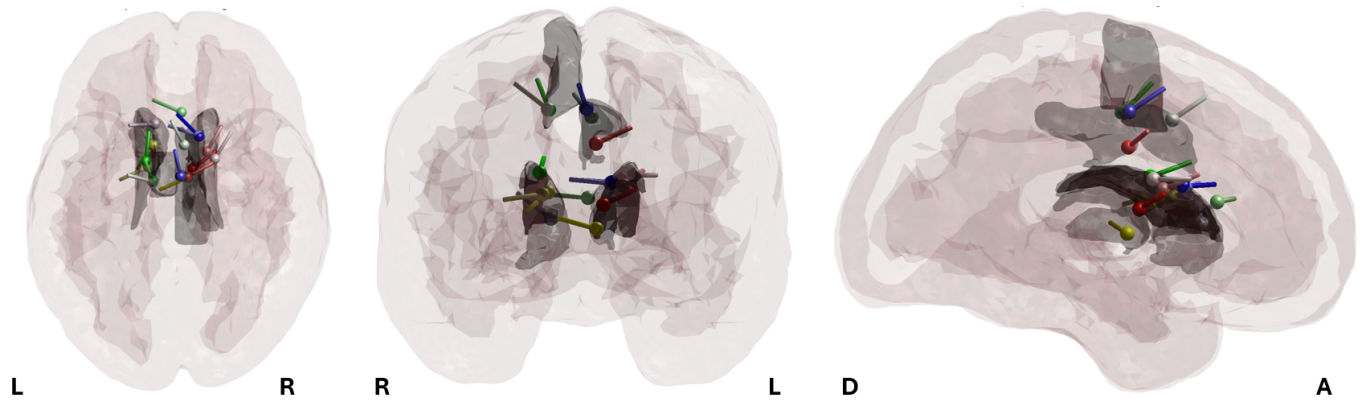

Figure 3.14: Brain mesh including the dipoles for C0 and C1 high stimulation (brighter colored dipoles) and low stimulation (lighter shade dipoles). Red, green, blue and yellow correspond to EP component 1, 2, 3, and 4, respectively.

DBS contacts

In general, the results indicate that stimulation at deeper DBS contacts (C0 and C1) evoke higher magnitude responses, compared to stimulation at the more superficial contacts (C2 and C3) (4/6). Additionally, the stimulating DBS contact influences the EP latency (6/6). This latency variation arises from distinct GMFP trends, where at least two GMFP curves (corresponding to different stimulating contact), show similar trends. The other GMFP plots show a dissimilar pattern, thereby contributing to the differences in latency

across contacts. The topographies indicate consistent spatial patterns across most DBS contacts. Specifically, the topographies corresponding to stimulating C0 and C1 contacts (occasionally including stimulation at C2), were visually similar per EP component. Stimulation at C3 often showed a distinct spatial distribution. This similarity in topographies for deeper contacts and dissimilarity for stimulating C3 contact was observed in 5 out of 6 cases.

Figure 3.15 illustrates the sensor-level responses for implantation 1 at high amplitude, showing the GMFP on top and the corresponding topographies below. The latencies of the evoked potentials are summarized in Table 3.2. The GMFP at stimulating C0 and C1 shows visually similar amplitude and latencies. The topographies further indicate this similarity, where stimulation at C0 and C1 shows comparable spatial patterns across the EP components. Stimulation at C2, however, produces a noisier response, which is reflected in a less smooth topography. Despite this, the EP latencies appear similar to those of stimulation at C0 and C1. In contrast, stimulation at C3 results in remarkable reduced GMFP amplitude and distinct topographic maps, which differ visually from those of the other contacts. The similarities between EP components 1 and 2 for stimulation at C0 and C1 are visualized in greater detail in Figure 3.16.

Table 3.2: Latency values (ms) for each EP component across contacts.

	EP 1	**EP 2**	**EP 3**	**EP 4**
C0	8.25	19.5	48.5	71.25
C1	9	20	50.35	68
C2	7.25	20	40.25	87.5
C3	8.75	20.25	35.5	67.75

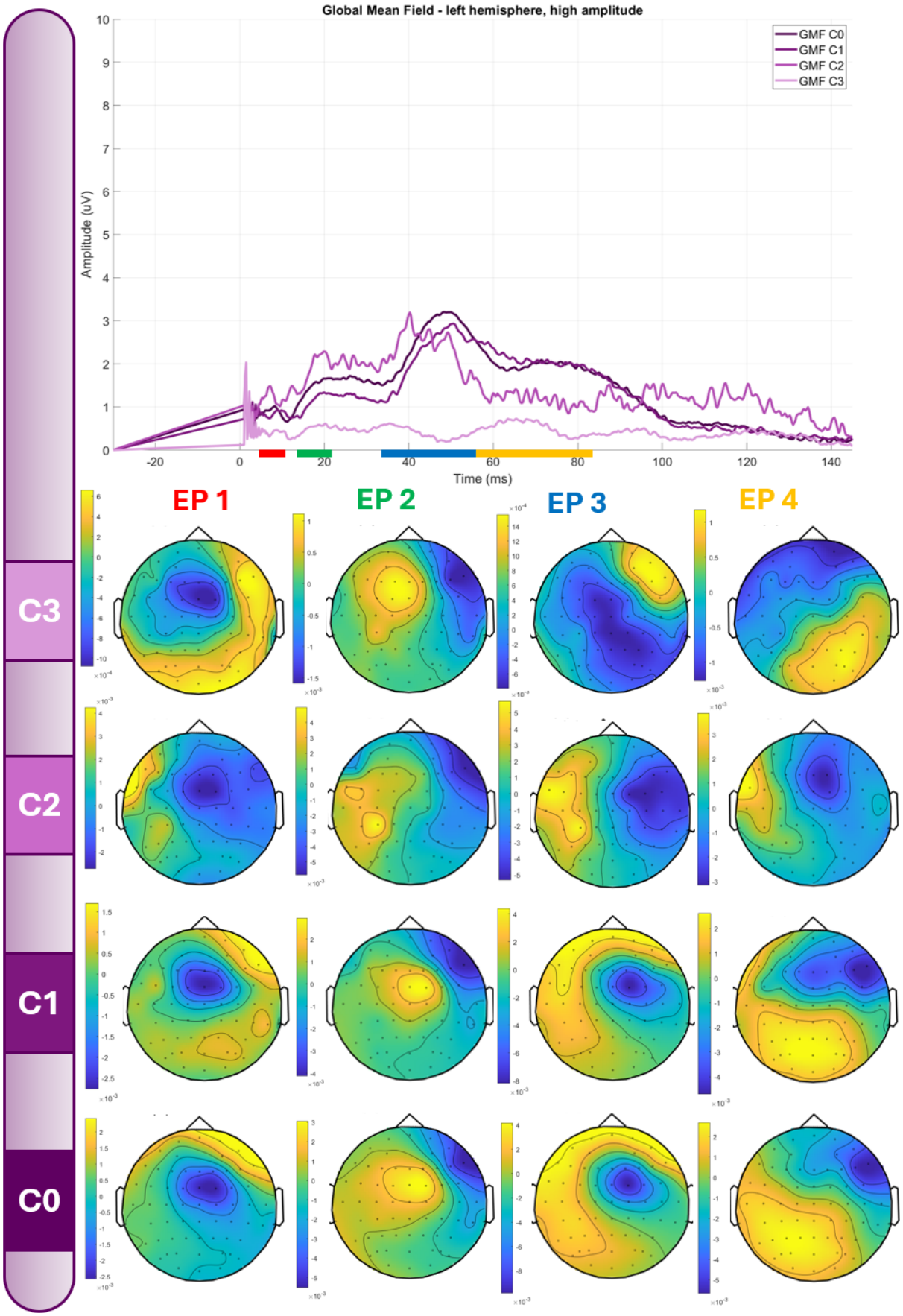

Figure 3.15: GMFP plot and topographic maps of the EP components for implantation 1 (high amplitude). The GMFP plot shows the amplitude of the responses over time for each contact (C0, C1, C2, and C3), with distinct intervals highlighting for latencies: 1 (red), 2 (green), 3 (blue), and 4 (yellow). Below the plot are the corresponding topographies for each EP component across different contacts, demonstrating the spatial distribution of the activation on the scalp. The colorbar indicates the measured potential in mV and is different for every topography.

Reconstructed dipole source analysis revealed distinct locations for each stimulating DBS contact across the EP components. For stimulation in C0, the sources were primarily located within the subcortical regions (12), such as the caudate nucleus (6) and thalamus (4). Cortical structures (8) included the cingulate gyrus (3) and the superior frontal gyrus (2), among other regions. A more balanced distribution was observed for stimulation at C1, with 10 subcortical sources (of which 7 within the caudate nucleus) and 9 cortical sources (of which 4 in the middle frontal gyrus). Reconstructed sources from stimulating contact C2 were primarily located within subcortical regions (11), such as the caudate nucleus (8). Cortical structures included 7 sources in total, with 4 located in the cingulate gyrus. Stimulation at contact C3 showed more cortical sources (10), within the cingulate gyrus (6) than subcortical sources (7), within the caudate nucleus (4).

The data revealed that 14/24 cases (58%) show consistent source locations across different stimulating DBS contacts, with DBS amplitude and implantation kept constant. The majority (10/14) were sources located within the caudate nucleus. Furthermore, high DBS amplitude (9) showed more consistent source locations compared to low amplitude (5).

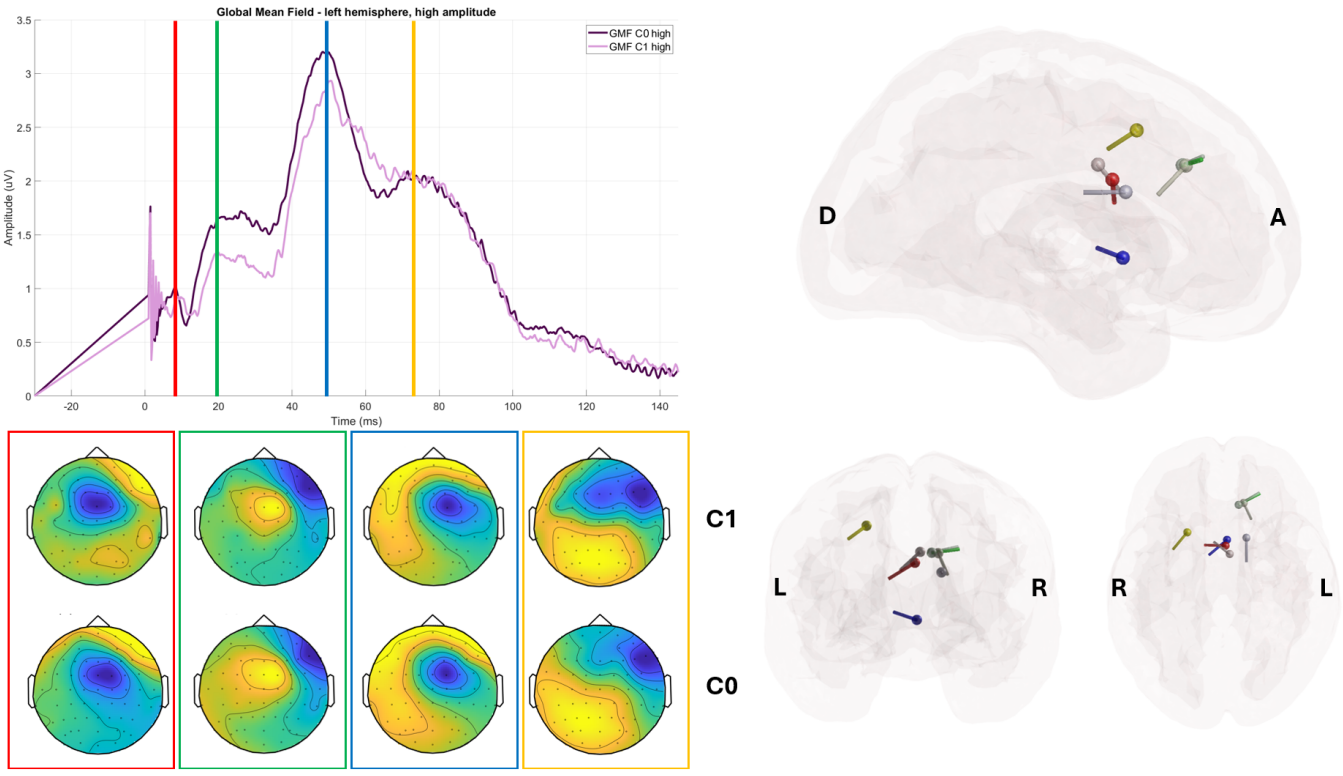

Figure 3.16: Relevant results of implantation 1 (C0/C1 high amplitude). **Top left**: GMFP of C0 (dark) and C1 (light) and corresponding EP components (1-2-3-4) in (red-green-blue-yellow). **Bottom left**: topographies corresponding to the EP components for C0 (bottom row) and C1 (top row). **Right**: reconstructed dipole sources of C0 (bright colors) and C1 (light colors).

Figure 3.16 illustrates the GMFP of high-amplitude stimulating implantation 1 at C0 and C1 and the topographies corresponding to the latencies of the indicated EP components. In the right, the corresponding dipole plot is visualized. The trend of the GMFP is similar, evoking responses at the same latencies and the topographies appear to be visually similar. The dipoles corresponding to EP component 1 (red) and 2 (green) appear to have a similar location and orientation for both stimulating contacts. Although the topographies of EP component 3 (blue) and 4 (yellow) appear to be visually similar, their source locations and orientation are dissimilar.

DBS Implantation

The effect of DBS implantation on the EP components was analyzed across both subjects, revealing that the majority of the implantations evoked responses ($> 1\mu$V). Figures C.3 and C.4 illustrate the evoked responses for patient DBS011 and patient DBS014, respectively. For DBS011, the stimulating DBS implantation (left) did not evoke any responses that exceeded this threshold, for both high and low DBS amplitude. Stimulation in the right DBS implantation consistently produced evoked responses across all parameter configurations.

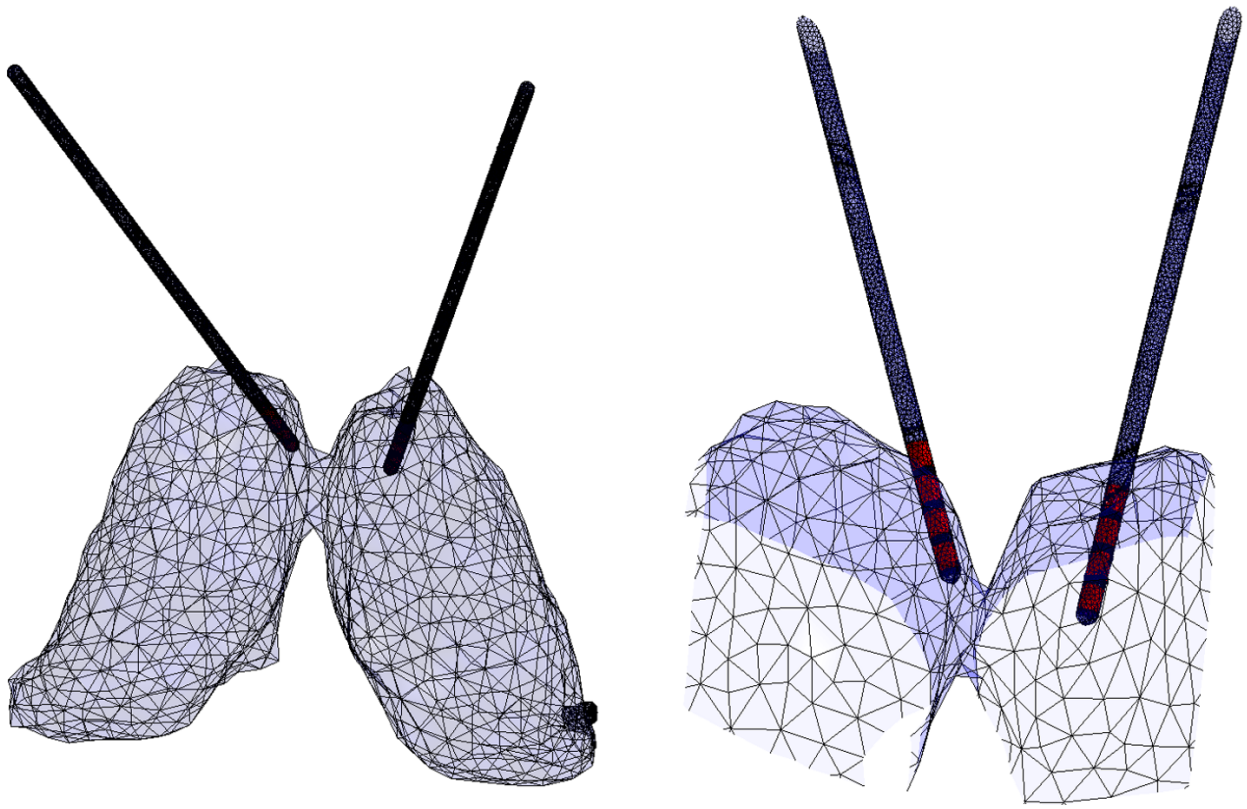

Figure 3.17: Left: visualization of the DBS within the thalamus for subject DBS011.Right: same image, rotated and zoomed in, highlighting the contacts in red.

Figure 3.17, visualizing the DBS leads within a thalamus mesh for patient DBS011, provides insight into the relation between electrode placement and the EP magnitude. For the right DBS lead, the electrode was positioned directly within the thalamus, with all contacts entirely inside the thalamus. In contrast, the left DBS lead was placed more superficially, with contact C3 placed outside the thalamus.

For the second patient, DBS014, a reduced response was also noted for the stimulating left DBS implantation. Figure 3.18 illustrates the placement of the DBS leads within the thalamus for subject DBS014. Although the exact mesh was not available for this patient, we manually plotted the electrode coordinates within the thalamus mesh. The right DBS electrode appears to be more centrally placed within the thalamus, while the left electrode appears to be close to the border.

The DBS implantation influences both the EP latency and magnitude. stimulating right DBS shaft implantations (implantation 1 & 3) consistently resulted in earlier EP latencies and higher magnitudes across all configurations. In contrast, the stimulating left DBS shaft implantations (implantation 4) produced slightly delayed EP latencies and lower magnitudes, with no responses exceeding 1μV (except for implantation 4, stimulating C0 with high amplitude).

The effect of DBS implantation on source location was analyzed by comparing the distribution of cortical and subcortical activations across different implantation sites. The results demonstrate that the stimulating DBS implantation influences the source location. stimulating implantation 1 showed the highest cortical activation (15/24), primarily located in the cingulate gyrus (6) and superior frontal gyrus (6). stimulating implantation 3 showed a more balanced distribution with 12 cortical and 18 subcortical sources, mainly located in the caudate nucleus (14) and cingulate gyrus (6). stimulating implantation 4 showed primarily sources in the subcortical structures (20/28), within the caudate nucleus (15). The data revealed that 35/54 cases showed a subcortical source location, while the remaining sources were located in the cortical structures (with other parameters kept constant).

For half of the cases (17/32), the source location is consistent through the stimulating DBS implantation. For cases where a left and right DBS implantation were compared, the opposite hemisphere relative to the stimulation site was analyzed for a valid comparison.

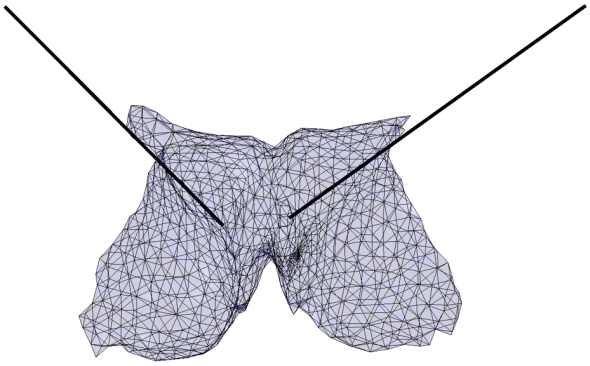

Figure 3.18: Visualization of the DBS leads within the thalamus for subject DBS014.

3.6 Validation

To validate the sensitivity of the source reconstruction method, we have reconstructed the source of the DBS artifact (at $t = 0$). The results are depicted in Figures 3.19 and 3.20. For DBS011, we can see that the dipole is close to the stimulation site. The Euclidean distance between the centroid of the dipole source to the centroid of the C0 contact of the DBS lead is 14.7 mm for DBS011, and 37.1 mm for DBS014.

To validate the latency of the EP components, we analyzed the neural path of the reconstructed source and estimated the latency based on an average conduction velocity. The distance from the reconstructed dipole source within the thalamus to the one in the superior frontal gyrus was calculated to be 104.8 mm, and the time required for this was 6 ms in the source reconstruction. This corresponds to an estimated conduction velocity of $v = \frac{104.8mm}{6ms} = 17.47m/s$. The return pathway from the superior frontal gyrus back to the thalamus covered a total distance of 134.54 mm in 7 ms, yielding an estimated conduction velocity of $v = \frac{134.54mm}{7ms} = 19.22m/s$.

To validate that sources within deeper brain structures can result in a measurable scalp-EEG signal, we estimated the dipole strength needed for the measured signal. A dipole located at $[-0.977523]$ (thalamus) shows a measured potential at the CP5 channel of $4.5 \cdot 10^{-6}$ V. The effective conductivity σ_{eff} was estimated to be 0.383 S/m. The Euclidean distance between the reconstructed dipole and the CP5 channel was calculated to be 88.16 mm. The corresponding dipole strength was calculated to be $1.68 \cdot 10^{-7}$ Am.

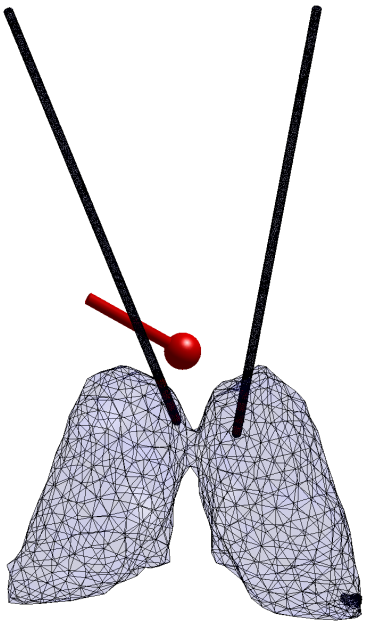

Figure 3.19: Mesh of the thalamus including the DBS leads and the reconstructed dipole source at $t = 0$ for DBS011(implantation 1, stimulating at C0 for high amplitude).

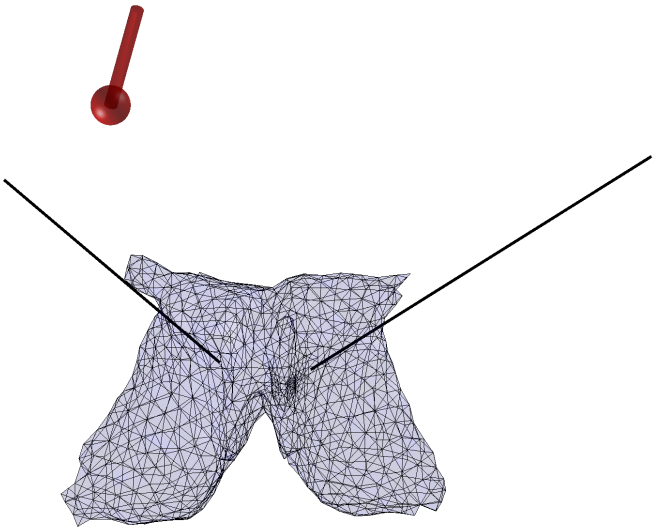

Figure 3.20: Mesh of the thalamus including the DBS leads and the reconstructed dipole source at $t = 0$ for DBS014 (implantation 3, stimulating at C0 for high amplitude).

Chapter 4

Discussion

This research aimed to explore the effects of low-frequency DBS on evoked potentials in patients with epilepsy, specifically by examining how variations in DBS parameters (DBS contact, DBS amplitude, and DBS implantation) modulate the sensor and source space of the evoked potentials, in terms of EP latency, EP magnitude and reconstructed source location.

EP components

Using a combination of EEG signal analysis and source reconstruction techniques, we identified four latency intervals for EP components: 3-10 ms, 19-26 ms, 37-58 ms, and 55-117 ms. These latencies correspond to different neural structures that are related to the Papez circuit. Additionally, we observed that variations in DBS amplitude and DBS contact influence both the magnitude and spatial distribution of the responses. Overall, the findings demonstrated inter- and intra-individual variation in both latency and source location, which could result from the precise electrode placement or assumptions about the volume conduction characteristics of surrounding tissue. These variations highlight the importance of precise electrode placement and the need for further studies to refine patient-specific modeling of evoked potentials in low-frequency DBS.

Literature on evoked responses of ANT-DBS is scarce; however, research on sub-thalamic nucleus (STN)-DBS indicated early responses at 3 ms and 10 ms after the DBS artifact [40], [50] and late responses at 18-25 ms latency [50]. Although these findings align with the latencies observed in this study, it is important to note that the mechanisms and networks involved in STN-DBS differ from those associated with ANT-DBS. Longer-latency EPs have been found in ANT-DBS research at 35/38 ms and 65 ms [33].

Papez Circuit

The precise relationship between the Papez circuit and seizure generation remains a topic of ongoing research; however, its anatomical connectivity and role in thalamocortical and limbic pathways suggest it might be influenced by ANT-DBS. The findings of this study demonstrate that reconstructed dipoles following ANT-DBS cluster within these regions, indicating activation of neural pathways associated with the circuit.

For implantation 1 (stimulating C1 at high amplitude), the reconstructed dipoles revealed a clear pattern following structures from the Papez circuit. The sequence of activation (thalamus, cingulate gyrus, superior frontal gyrus, caudate nucleus, thalamus, nucleus accumbens) suggests that the DBS activates neural pathways associated with the thalamocortical pathway and limbic circuit. The temporal and spatial patterns

aligns with the anatomical connectivity of the Papez circuit, further supporting the hypothesis that ANT-DBS modulates this pathway. The reconstructed dipoles follow a circular movement around the thalamus, as found in previous research in low-frequency ANT-DBS [41]. The RV for these dipoles were all ≤ 0.2 with some dipoles ≤ 0.1. A previous study suggests a RV threshold of 0.1 [51]. This implies that most reconstructed dipoles were reliable, however, some require cautious interpretation. The sequential pattern observed in this implantation supports that DBS influences the Papez circuit, but further studies are needed to confirm these findings.

For implantation 3 and 4 (stimulating C1 at high amplitude), the reconstructed dipoles were less distinct in their temporal and spatial organization compared to implantation 1. While the dipoles are clustered within the structures associated with the Papez circuit (thalamus, cingulate gyrus, superior frontal gyrus, and caudate nucleus), they did not follow a sequential pattern as clearly as in implantation 1. The RV values are all ≤ 0.2, with some optimal values ≤ 0.1 during the GMFP peak between 30-50 ms. This implies that the reconstructed dipoles corresponding within this time window were a good fit on the data.

Interestingly, for implantation 4, the dipoles during a time window of 30-110 after DBS artifact, were primarily clustered within the left dorsal caudate. Most dipoles showed an RV ≤ 0.1, reflecting a high reliability. This clustering of the dipoles within the basal ganglia, suggests that subcortical regions outside the Papez circuit may also be involved in the network dynamics influenced by ANT-DBS. It has been hypothesized that the basal ganglia are involved in the propagation and termination of focal onset seizures originating in the frontal and temporal lobes [52]. A previous study on thalamus and basal ganglia involvement in focal epilepsy showed high thalamic epileptogenicity in 20% of the patients and for the caudate nucleus high epileptogenicity in 9% of the patients [53]. This indicates that the location of seizure generation has inter-individual variability. Some researchers suggest that the basal ganglia play a role in inhibiting seizure spread by influencing the feedback pathways to the cortex [54].

DBS amplitude

Our findings indicate that DBS amplitude has an effect on the magnitude of the EPs, but does not influence their latency. Across all configurations analyzed, the latencies of the EPs remained consistent between high- and low amplitude DBS, aligning with previous research on STN-DBS that reported no latency shifts with changes in amplitude [55], [56]. This consistency suggests that DBS-induced responses at specific latencies are determined by fixed pathways that are unaffected by DBS amplitude.

High-amplitude DBS produced larger magnitude responses compared to low-amplitude stimulation. This finding is supported by prior studies demonstrating a positive correlation between DBS amplitude and the magnitude of responses [46], [57], [58]. The high-amplitude DBS likely activates a larger population of neurons, resulting in greater response magnitudes. Conversely, low-amplitude DBS evoked responses with low magnitude, particularly at the more superficial contacts (C2 and C3).

Interestingly, our results indicate both similarities and dissimilarities in the topographies between high- and low-amplitude DBS measured through scalp-EEG. These (dis)similarities are also present in the locations of the reconstructed dipole sources.

It has been argued that the topographies depend on DBS amplitude and inter- and intra-individual variation [46]. Furthermore, an animal study on ANT-DBS showed that the stimulation current is a relevant parameter. They indicated that a low amplitude (200 μA) results in no effect, and an amplitude that is too high (1000 μA) has a proconvulsant effect, meaning it decreases the latency of the seizures rather than increasing it [28].

One possible explanation for the differences in the topographies, reconstructed dipole source location,

and orientation between high- and low-amplitude DBS could be related to the SNR. At low amplitude, the SNR is generally lower because the magnitude of the evoked response is lower, and therefore, the signal is more susceptible to interference from background noise. The source reconstruction algorithm might then struggle to find the source location and orientation accurately. The high amplitude stimulation evokes, in general, a more robust response, which might be less affected by noise (high SNR).

DBS contact

Our findings indicate that DBS contact influences both the EP magnitude and the topographies, as well as the latency in certain cases. Stimulation at deeper contacts (C0 and C1) consistently produced higher magnitude responses compared to stimulation at more superficial contacts (C2 and C3) (4/6). Prior research suggests that the evoked response amplitude was significantly different between stimulation contacts [55]. This suggests that deeper contacts, that are positioned well in the ANT, effectively activate a neural network, while the superficial contacts may engage different pathways or smaller populations. This pattern can be explained by the anatomical positioning of the contacts relative to the target area, the ANT. The C0 and C1 are placed deeper within the target region than C2 and C3 positioned closer to the surface or outside of it (Figure 3.17). These differences in placement are likely to influence the evoked responses.

The results also revealed that the DBS contact influences the EP latency (6/6). Variations in the latencies came from distinct GMFP trends, where at least two GMFP curves (corresponding to different stimulating contacts) showed similar patterns, while others showed dissimilar patterns. Our findings partly align with previous research that suggests that the peak latency did not vary between stimulating contacts [55]. A possible explanation for the differences in evoked responses per stimulating contact could be the exact placement of the contacts. If the superficial contacts are placed on the border or outside the ANT, they might evoke different neurons and pathways, which could cause variations in EP latency. Previous research on STN-DBS in Parkinson's disease suggests that different neural circuits have different temporal latencies [59].

Our findings showed a consistent pattern in the topographies for C0-C1 (and sometimes C2) and (sometimes C2 and) C3 stimulation across all conditions. One possible explanation could be that the C0 and C1 contacts are placed deep within the ANT and that contacts C2 and C3 are placed more superficial, or even outside the ANT. Previous research suggests that differences in the evoked responses inter- and intra-individual can be due to variations in the placement of the DBS electrode [60].

Reconstructed dipole source analysis provided additional insights into the distribution of activation across cortical and subcortical regions. Consistent source locations across different contacts were observed in 58% of the cases, with the majority of these consistent sources located within the caudate nucleus. This consistency is more evident for contacts in close proximity (C0 and C1). Contacts that are further apart (C0 and C3) are more likely to evoke responses from distinct locations.

DBS Implantation

Our results revealed that the anatomical placement of the DBS leads notably influences the EP magnitude, with responses being stronger and more persistent for the ones positioned deep and straight within the thalamus. In both subjects, the right DBS implantation produced consistent responses across all configurations, while the left implantation either failed to evoke responses (for subject DBS011) or showed reduced responses (for subject DBS014). This is likely related to the placement of the DBS leads within the thalamus (Figure 3.17 and 3.18). A study on ANT-DBS stated that suboptimal placement can reduce efficacy and lead to greater variability in neural activation [**?**]. Similarly, previous research on STN-DBS has shown

that electrode placement within the target area is critical for effective responses [59]. We have seen that suboptimal placement reduce both EP latency and EP magnitude. These results indicate the importance of precise surgical placement to maximize the efficacy of low-frequency ANT-DBS.

Validation

The validation of the source reconstruction method provided important insights into its accuracy and reliability. The reconstructed dipole sources for the DBS artifact demonstrated spatial accuracy in proximity to the target area; on average 25.9 mm. This might limit the interpretability of the evoked potentials and its source locations. This highlights the need for improving the method's sensitivity. Achieving greater localization precision is relevant for interpreting the DBS-induced evoked potentials.

The estimated conduction velocities between reconstructed sources were 17.47 m/s for the path from thalamus to the superior frontal gyrus (through the cingulate gyrus) and 19.22 m/s for the return to the thalamus (through the cingulate gyrus and caudate nucleus). These values fall within the range of conduction velocities for myelinated axons [61]. This supports the phsyiological plausibility of the reconstructed sources and the corresponding EP latencies.

Finally, the calculated dipole strength of $1.68 \cdot 10^{-7}$ Am (168 nAm) for a source located in the thalamus aligns with values reported in the literature [62], [63]. They propose that a dipole strength on the order of 10 nAm is required for measurable scalp-EEG signals. The dipole strength we calculated differs one order of magnitude with this value. This supports the plausibility of the reconstructed source and its possibility to be measured by scalp-EEG.

4.1 Limitations and Recommendations

This study presents an exploratory analysis of low-frequency DBS in epilepsy, focusing on the evoked responses generated by varying stimulation parameters. While these findings contribute valuable insights, several limitations must be acknowledged to consider the results and suggest future research.

The first limitation is the small sample size (n = 2), which might limit the generalizability of the findings, especially regarding the inter- and intra-individual variability of the results. As the new protocol of the EANSkE study just started, more data will be available in the future to validate these findings and inter-individual variability. A larger sample size is essential to validate these findings and explore statistical relationships between the DBS parameters and the results.

Additionally, the DBS artifact is removed by applying template subtraction and assuming that the mastoid electrodes (M1 and M2) do not capture that much neural activity [40]. If those electrodes do capture relevant neural activity, this information is lost by subtracting the template. This could be solved by determining the template based on electrodes that are placed farther from the brain and do not measure neural activity.

The assumptions in the forward model, including isotropic conductivity, could possibly present another limitation. While the current model assumes uniform average conductivity values across tissue types, white matter conductivity is known to be anisotropic. This simplification could lead to inaccuracies in the forward model and subsequent source reconstruction [64]. Research using experimental data from visual stimulation found that realistic white matter anisotropic conductivity distributions did not significantly improve the localization of dipoles [65]. Given this, while the inclusion of anisotropic conductivity might theoretically provide a more accurate forward model, its practical impact on source reconstruction in the context of DBS-induced evoked potentials remains uncertain. Future research could investigate whether anisotropic

models provide significant benefits. Additionally, the head model is based on the T1- and T2 images of the subject; however, the EEG electrodes are manually aligned based on a standard template and introduce a level of inaccuracy. A 3D scan including the coordinates of the EEG electrodes could be a solution, enhancing the spatial accuracy and improving the overall sensitivity of the source reconstruction pipeline [66]. Furthermore, the current head model does not include the DBS leads and its conductivity. The electrode may influence the electrical field distribution and therefore also the evoked responses. Including the DBS in the model would improve the model and interpretation of the stimulation effects.

A fundamental limitation lies in the challenges associated with the EEG source reconstruction, which is inherently ill-posed. While using a single equivalent dipole model, this approach simplifies neural activity and assumes that a single dipolar source can explain the EEG measured signals. In reality, neural activity can be complex, and multiple brain regions are likely activated simultaneously, which cannot be captured by this single dipole model. A possible solution could be to apply different inverse models and compare the results to check for accuracy. Beamforming is another inverse method that constructs a spatial filter that can estimate the activity of sources across the brain volume. The accuracy of the dipole localization could be assessed by comparing the results from beamforming with the dipole fitting results.

The relative position of the DBS leads to the ANT has an impact on the observed evoked responses. Future studies should investigate the precise relationship between lead position and the evoked responses, in combination with the efficacy, to optimize the DBS outcomes.

While this study focuses on the DBS-induced evoked responses, it does not include the clinical outcomes of the patients, such as seizure reduction. Including these outcomes would provide a better understanding between the effects of the DBS parameters and the clinical efficacy. This could also guide the development of more patient-specific DBS-protocols.

Another limitation is that the topographic maps, visualized in Appendix D, are snapshots of a specific time point rather than an average over a time window. The evoked potentials are determined as the peaks of the GMFP plot, and since these peaks do not always align precisely, the EPs across conditions may capture different stages of the response. This could lead to misleading comparisons. An average topographic map over a standardized time window could improve the consistency in comparing the topographies across conditions. This would smooth the variability in peak timing and provide a more stable topography.

While this study solely focuses on low-frequency stimulation, comparing these findings with high-frequency DBS would be valuable, since high-frequency is the clinical standard. High-frequency DBS has effectively reduced seizure frequency by modulating neural circuits, such as the Papez circuit. Contrasting the effects of low- and high-frequency ANT-DBS could further elaborate on the underlying mechanisms and optimize treatment in epilepsy. Additionally, previous research suggest a potential overlap between the DBS-induced evoked potentials and the epileptic activity maps [41]. Such overlaps might represent a mechanism where DBS interacts with the seizure networks. Extending this approach to include the epileptic activity maps could offer a more detailed understanding of the interactions between the DBS and the epileptic networks. Future research could integrate these epileptic activity maps with the DBS maps to improve the development of predictive markers for patient-specific ANT-DBS treatment.

Sequential dipole fitting is an alternative inverse method used to model the temporal dynamics of neural activity. This approach assumes that a single equivalent current dipole can explain early EP components. As the activity evolves and becomes more widespread over time, additional dipoles are introduced to account for the later response components, allowing for the estimation of their spatial positions. Finally, the activity of all dipoles is re-estimated to refine the model and enhance its accuracy in representing the underlying neural processes. Although the documentation on this method is scarce, this approach could offer more

insights into how DBS impacts the brain over time.

Chapter 5

Conclusion

This study examined low-frequency ANT-DBS to study the effects of DBS parameters on the evoked potentials (EPs) in patients with drug-resistant epilepsy (DRE). The focus was on how DBS parameters (DBS amplitude, DBS contact, and DBS implantation) modulate EPs characterized by EP latency, EP magnitude, and source location. The aim was to investigate the electrophysiological mechanisms of low-frequency ANT-DBS and its impact on related neural networks.

The analysis revealed distinct EP components at four latencies: 3-10 ms, 19-26 ms, 37-58 ms, and 55-117 ms. The observed responses indicated modulation of neural activity along structures related to the Papez circuit, e.g. the thalamus, cingulate gyrus, and superior frontal gyrus, suggesting that ANT-DBS engages this network.

Higher DBS amplitude consistently evoked higher magnitude responses, without altering EP latency. Furthermore, the reconstructed source locations varied between the high vs. low DBS amplitude, with the high amplitude evoking responses within more subcortical structures. Stimulated contacts C0 and C1 evoked higher magnitude EPs than stimulated C2 and C3. EP latencies were influenced by the DBS contact, as their GMFP showed distinct patterns, with stimulated contacts C0 and C1 (and sometimes C2) showing similar patterns. Similar EP magnitudes and latencies were observed in stimulated left (and right) DBS implantation, suggesting symmetrical network activation. Reconstructed dipoles across the time series suggested sequential activation of structures related to the Papez circuit (e.g. the thalamus, cingulate gyrus, superior frontal gyrus, and basal ganglia).

There are several limitations that should be addressed in future research. First, the small sample size limits the generalizability. Expanding the sample size would provide a better understanding of the inter- and intra-individual variability. Additionally, this study assumes a single equivalent dipole model, which might oversimplify the complex dynamics of neural activity. Comparing these dipole fitting results with other inverse models (e.g. beamforming or sequential dipole fitting) could increase the robustness. This study highlights the need for further investigation into the Papez circuit's role in epilepsy.

These findings underscore the importance of optimizing the DBS parameters and advancing our understanding of thalamocortical networks, such as the Papez circuit, to improve patient-specific therapy for epilepsy.

Bibliography

[1] H. E. Scharfman, "The neurobiology of epilepsy," *Current Neurology and Neuroscience Reports*, vol. 7, no. 4, pp. 348–354, 7 2007.

[2] R. S. Fisher, C. Acevedo, A. Arzimanoglou, A. Bogacz, J. H. Cross, C. E. Elger, J. Engel, L. Forsgren, J. A. French, M. Glynn, D. C. Hesdorffer, B. I. Lee, G. W. Mathern, S. L. Moshé, E. Perucca, I. E. Scheffer, T. Tomson, M. Watanabe, and S. Wiebe, "ILAE official report: a practical clinical definition of epilepsy," *Epilepsia*, vol. 55, no. 4, pp. 475–482, 2014.

[3] WHO (World Health Organisation), "Epilepsy," 2024.

[4] E. B. Bromfield, J. E. Cavazos, and J. I. Sirven, "Basic Mechanisms Underlying Seizures and Epilepsy," in *An Introduction to Epilepsy*. American Epilepsy Society, 2006, ch. 1.

[5] R. D. Thijs, R. Surges, T. J. O'Brien, and J. W. Sander, "Epilepsy in adults," *The Lancet*, vol. 393, no. 10172, pp. 689–701, 2 2019.

[6] E. Burakgazi and J. A. French, "Treatment of epilepsy in adults," *Epileptic Disorders*, vol. 18, no. 3, pp. 228–239, 9 2016.

[7] V. Salanova, "Deep brain stimulation for epilepsy," *Epilepsy & Behavior*, vol. 88, pp. 21–24, 11 2018.

[8] G. L. Morris and W. M. Mueller, "Long-term treatment with vagus nerve stimulation in patients with refractory epilepsy," *Neurology*, vol. 53, no. 8, pp. 1731–1735, 11 1999.

[9] P. Ryvlin, S. Rheims, L. J. Hirsch, A. Sokolov, and L. Jehi, "Neuromodulation in epilepsy: state-of-the-art approved therapies," *The Lancet Neurology*, vol. 20, no. 12, pp. 1038–1047, 12 2021.

[10] R. Fisher, V. Salanova, T. Witt, R. Worth, T. Henry, R. Gross, K. Oommen, I. Osorio, J. Nazzaro, D. Labar, M. Kaplitt, M. Sperling, E. Sandok, J. Neal, A. Handforth, J. Stern, A. DeSalles, S. Chung, A. Shetter, D. Bergen, R. Bakay, J. Henderson, J. French, G. Baltuch, W. Rosenfeld, A. Youkilis, W. Marks, P. Garcia, N. Barbaro, N. Fountain, C. Bazil, R. Goodman, G. McKhann, K. B. Krishnamurthy, S. Papavassiliou, C. Epstein, J. Pollard, L. Tonder, J. Grebin, R. Coffey, N. Graves, M. Dichter, W. Elias, P. Francel, R. Frysinger, K. Graber, J. Grant, G. Heit, S. Herman, P. Kandula, A. Kanner, J. A. King, E. Kobylarz, K. Lapp, S. LaRoche, S. Lippmann, R. Maganti, T. Mapstone, D. Sabau, L. Schrader, A. Sharan, M. Smith, D. Treiman, S. Wilkinson, S. Wong, A. Zangaladze, S. Adderley, B. Bridges, M. Callanan, D. Cordero, C. Fields, M. Johnson, M. A. Kavalir, P. Kretschmar, C. Macpherson, K. Mancl, M. Manley, S. Marsh, J. Montgomery, P. Mundt, P. P. Nekkalapu, B. Nikolov, B. Palmer, L. Perdue, A. Randall, D. Smith, L. Smith, K. Strybing, L. Stott, R. Taylor, S. Thompson, Z. Timenova, B. Vogelsong, V. Balbona, D. Broshek, D. Cahn-Weiner, L. Clift, M. Davidson, E. Drake, S. Frutiger, L. Featherstone, C. Grote, D. Han, D. Henry, J. Horsfall,

A. Hovick, J. Gray, D. Kareken, K. Kirlin, D. Livingood, M. Meyer, N. Minniti, J. M. Strupinsky, W. Schultz, J. Scott, J. Tracy, S. Waltonen, P. Ziefert, C. Van Amburg, M. Burdelle, S. Clements, R. Cox, R. Dolin, M. Fulk, H. R. Kaur, L. Hirsch, T. Hoeppner, A. Hurt, M. Komosa, S. Krahl, L. Ponticello, M. Quigg, H. Quinn, M. Rossi, P. Schaefer, C. Skidmore, D. Sundstrom, P. Trudeau, M. Volz, N. Wang, L. Will, and C. Young, "Electrical stimulation of the anterior nucleus of thalamus for treatment of refractory epilepsy," *Epilepsia*, vol. 51, no. 5, pp. 899–908, 5 2010.

[11] J. Gardner, "A history of deep brain stimulation: Technological innovation and the role of clinical assessment tools," *Social Studies of Science*, vol. 43, no. 5, p. 707, 10 2013. [Online]. Available: https://pmc.ncbi.nlm.nih.gov/articles/PMC3785222/

[12] P. Limousin and I. Martinez-Torres, "Deep Brain Stimulation for Parkinson's Disease," *Neurotherapeutics*, vol. 5, no. 2, pp. 309–319, 4 2008.

[13] A. L. Benabid, S. Chabardes, J. Mitrofanis, and P. Pollak, "Deep brain stimulation of the subthalamic nucleus for the treatment of Parkinson's disease," *The Lancet Neurology*, vol. 8, no. 1, pp. 67–81, 1 2009.

[14] M. Figee, P. Riva-Posse, K. S. Choi, L. Bederson, H. S. Mayberg, and B. H. Kopell, "Deep Brain Stimulation for Depression," *Neurotherapeutics*, vol. 19, no. 4, pp. 1229–1245, 7 2022.

[15] P. Blomstedt, R. L. Sjöberg, M. Hansson, O. Bodlund, and M. I. Hariz, "Deep Brain Stimulation in the Treatment of Obsessive-Compulsive Disorder," *World Neurosurgery*, vol. 80, no. 6, pp. e245–e253, 12 2013.

[16] V. Salanova, T. Witt, R. Worth, T. R. Henry, R. E. Gross, J. M. Nazzaro, D. Labar, M. R. Sperling, A. Sharan, E. Sandok, A. Handforth, J. M. Stern, S. Chung, J. M. Henderson, J. French, G. Baltuch, W. E. Rosenfeld, P. Garcia, N. M. Barbaro, N. B. Fountain, W. J. Elias, R. R. Goodman, J. R. Pollard, A. I. Tröster, C. P. Irwin, K. Lambrecht, N. Graves, and R. Fisher, "Long-term efficacy and safety of thalamic stimulation for drug-resistant partial epilepsy," *Neurology*, vol. 84, no. 10, pp. 1017–1025, 3 2015.

[17] J. J. Van Gompel, B. T. Klassen, G. A. Worrell, K. H. Lee, C. Shin, C. Z. Zhao, D. A. Brown, S. J. Goerss, B. A. Kall, and M. Stead, "Anterior nuclear deep brain stimulation guided by concordant hippocampal recording," *Neurosurgical Focus*, vol. 38, no. 6, p. E9, 6 2015.

[18] A. Vetkas, A. Fomenko, J. Germann, C. Sarica, C. Iorio-Morin, N. Samuel, K. Yamamoto, V. Milano, C. Cheyuo, A. Zemmar, G. Elias, A. Boutet, A. Loh, B. Santyr, D. Gwun, J. Tasserie, S. Kalia, and A. M. Lozano, "Deep brain stimulation targets in epilepsy: Systematic review and meta-analysis of anterior and centromedian thalamic nuclei and hippocampus," *Epilepsia*, vol. 63, no. 3, pp. 513–524, 3 2022. [Online]. Available: https://onlinelibrary.wiley.com/doi/full/10.1111/epi.17157https://onlinelibrary.wiley.com/doi/abs/10.1111/epi.17157https://onlinelibrary.wiley.com/doi/10.1111/epi.17157

[19] A. M. Lozano, N. Lipsman, H. Bergman, P. Brown, S. Chabardes, J. W. Chang, K. Matthews, C. C. McIntyre, T. E. Schlaepfer, M. Schulder, Y. Temel, J. Volkmann, and J. K. Krauss, "Deep brain stimulation: current challenges and future directions," *Nature reviews. Neurology*, vol. 15, no. 3, p. 148, 3 2019.

[20] T. J. Foutz and M. Wong, "Brain stimulation treatments in epilepsy: Basic mechanisms and clinical advances," *Biomedical Journal*, vol. 45, no. 1, p. 27, 2 2022.

[21] N. Zangiabadi, L. D. Ladino, F. Sina, J. P. Orozco-Hernández, A. Carter, and J. F. Téllez-Zenteno, "Deep brain stimulation and drug-resistant epilepsy: A review of the literature," *Frontiers in Neurology*, vol. 10, no. JUN, p. 433066, 6 2019. [Online]. Available: www.frontiersin.org

[22] H. Oikawa, M. Sasaki, Y. Tamakawa, and A. Kamei, "The circuit of Papez in mesial temporal sclerosis: MRI," *Neuroradiology*, vol. 43, no. 3, pp. 205–210, 2001.

[23] J. W. Papez, "A proposed mechanism of emotion," *Archives of Neurology & Psychiatry*, vol. 38, no. 4, pp. 725–743, 10 1937.

[24] B. C. Lega, C. H. Halpern, J. L. Jaggi, and G. H. Baltuch, "Deep brain stimulation in the treatment of refractory epilepsy: Update on current data and future directions," *Neurobiology of Disease*, vol. 38, no. 3, pp. 354–360, 6 2010.

[25] A. Kamali, S. Milosavljevic, A. Gandhi, K. R. Lano, P. Shobeiri, F. G. Sherbaf, H. I. Sair, R. F. Riascos, and K. M. Hasan, "The Cortico-Limbo-Thalamo-Cortical Circuits: An Update to the Original Papez Circuit of the Human Limbic System," *Brain Topography*, vol. 36, no. 3, p. 371, 5 2023. [Online]. Available: https://pmc.ncbi.nlm.nih.gov/articles/PMC10164017/

[26] Y. J. Choi, E. J. Lee, and J. E. Lee, "The Fornix: Functional Anatomy, Normal Neuroimaging, and Various Pathological Conditions," *Investigative Magnetic Resonance Imaging*, vol. 25, no. 2, pp. 59–75, 6 2021. [Online]. Available: https://doi.org/10.13104/imri.2021.25.2.59

[27] M. A. Mirski, L. A. Rossell, J. B. Terry, and R. S. Fisher, "Anticonvulsant effect of anterior thalamic high frequency electrical stimulation in the rat," *Epilepsy Research*, vol. 28, no. 2, pp. 89–100, 9 1997.

[28] C. Hamani, M. Hodaie, and A. M. Lozano, "Present and future of deep brain stimulation for refractory epilepsy." *Acta neurochirurgica*, vol. 147, no. 3, pp. 227–229, 1 2005.

[29] R. S. Fisher, W. Van Emde Boas, W. Blume, C. Elger, P. Genton, P. Lee, and J. Engel, "Epileptic seizures and epilepsy: definitions proposed by the International League Against Epilepsy (ILAE) and the International Bureau for Epilepsy (IBE)," *Epilepsia*, vol. 46, no. 4, pp. 470–472, 4 2005. [Online]. Available: https://pubmed.ncbi.nlm.nih.gov/15816939/

[30] A. Pitkänen and J. Engel, "Past and present definitions of epileptogenesis and its biomarkers," *Neurotherapeutics : the journal of the American Society for Experimental NeuroTherapeutics*, vol. 11, no. 2, pp. 231–241, 4 2014. [Online]. Available: https://pubmed.ncbi.nlm.nih.gov/24492975/

[31] A. Keller, K. Arissian, and H. Asanuma, "Synaptic proliferation in the motor cortex of adult cats after long-term thalamic stimulation," *Journal of neurophysiology*, vol. 68, no. 1, pp. 295–308, 1992.

[32] K. D. Graber and R. S. Fisher, "Deep Brain Stimulation for Epilepsy: Animal Models," *Jasper's Basic Mechanisms of the Epilepsies*, 7 2012.

[33] Y. C. Wang, V. Kremen, B. H. Brinkmann, E. H. Middlebrooks, B. N. Lundstrom, S. S. Grewal, H. Guragain, M. H. Wu, J. J. Van Gompel, B. T. Klassen, M. Stead, and G. A. Worrell, "Probing circuit of Papez with stimulation of anterior nucleus of the thalamus and hippocampal evoked potentials," *Epilepsy Research*, vol. 159, p. 106248, 1 2020.

[34] V. Kremen, V. Sladky, F. Mivalt, N. M. Gregg, I. Balzekas, V. Marks, B. H. Brinkmann, B. N. Lundstrom, J. Cui, E. K. S. Louis, P. Croarkin, E. C. Alden, J. Fields, K. Crockett, J. Adolf, J. Bilderbeek, D. Hermes, S. Messina, K. J. Miller, J. V. Gompel, T. Denison, and G. A. Worrell, "A platform for brain network sensing and stimulation with quantitative behavioral tracking: Application to limbic circuit epilepsy," *medRxiv*, p. 2024.02.09.24302358, 4 2024.

[35] K. H. Chiappa and A. H. Ropper, "Evoked Potentials in Clinical Medicine," *New England Journal of Medicine*, vol. 306, no. 19, pp. 1140–1150, 5 1982.

[36] R. Oostenveld, P. Fries, E. Maris, and J. M. Schoffelen, "FieldTrip: Open Source Software for Advanced Analysis of MEG, EEG, and Invasive Electrophysiological Data," *Computational Intelligence and Neuroscience*, vol. 2011, no. 1, p. 156869, 1 2011.

[37] B. Hjorth, "An on-line transformation of EEG scalp potentials into orthogonal source derivations," *Electroencephalography and Clinical Neurophysiology*, vol. 39, no. 5, pp. 526–530, 11 1975.

[38] B. A. Moore and J. E. Barnett, "Niedermeyer's Electroencephalography: Basic Principles, Clinical Applications, and Related Fields," *Case Studies in Clinical Psychological Science: Bridging the Gap from Science to Practice*, no. August, pp. 1–7, 11 2017.

[39] T. R. Knösche and J. Haueisen, *EEG/MEG Source Reconstruction: Textbook for Electro-and Magnetoencephalography*. Springer International Publishing, 1 2022.

[40] J. Peeters, A. Boogers, T. Van Bogaert, H. Davidoff, R. Gransier, J. Wouters, B. Nuttin, and M. Mc Laughlin, "Electrophysiologic Evidence That Directional Deep Brain Stimulation Activates Distinct Neural Circuits in Patients With Parkinson Disease," *Neuromodulation: Technology at the Neural Interface*, vol. 26, no. 2, pp. 403–413, 2 2023.

[41] L. Loosveld, "Source reconstruction of ANT-DBS induced evoked potentials and epileptiform discharges in patients with refractory epilepsy," 2024.

[42] M. R. Nuwer, "EEG topographic mapping and frequency analysis: Techniques and studies in clinical setting," *Seminars in Neurology*, vol. 10, no. 2, pp. 166–177, 1990.

[43] C. M. Michel and D. Brunet, "EEG source imaging: A practical review of the analysis steps," *Frontiers in Neurology*, vol. 10, no. APR, p. 446653, 4 2019.

[44] J. Vorwerk, R. Oostenveld, M. C. Piastra, L. Magyari, and C. H. Wolters, "The FieldTrip-SimBio pipeline for EEG forward solutions," *BioMedical Engineering OnLine*, vol. 17, no. 1, p. 37, 3 2018.

[45] P. H. Schimpf, C. Ramon, and J. Haueisen, "Dipole models for the EEG and MEG," *IEEE Transactions on Biomedical Engineering*, vol. 49, no. 5, pp. 409–418, 2002.

[46] T. A. Bouwens van der Vlis, O. E. Schijns, F. L. Schaper, G. Hoogland, P. Kubben, L. Wagner, R. Rouhl, Y. Temel, and L. Ackermans, "Deep brain stimulation of the anterior nucleus of the thalamus for drug-resistant epilepsy," pp. 287–296, 6 2019.

[47] "Evaluation of ANT-DBS Neuromodulation with Sensing Electrodes (EANSkE) — Research with human participants." [Online]. Available: https://onderzoekmetmensen.nl/en/trial/56397

[48] A. Thielscher, A. Antunes, and G. B. Saturnino, "Field modeling for transcranial magnetic stimulation: A useful tool to understand the physiological effects of TMS?" *Proceedings of the Annual International Conference of the IEEE Engineering in Medicine and Biology Society, EMBS*, vol. 2015-November, pp. 222–225, 11 2015.

[49] A. Horn and A. A. Kühn, "Lead-DBS: A toolbox for deep brain stimulation electrode localizations and visualizations," *NeuroImage*, vol. 107, pp. 127–135, 2 2015.

[50] A. Devergnas and T. Wichmann, "Cortical potentials evoked by deep brain stimulation in the subthalamic area," *Frontiers in Systems Neuroscience*, vol. 5, no. MAY 2011, p. 10278, 5 2011.

[51] A. Delorme, J. Palmer, J. Onton, R. Oostenveld, and S. Makeig, "Independent EEG sources are dipolar," *PLoS ONE*, vol. 7, no. 2, 2 2012.

[52] S. Pati, S. Agashe, A. Kheder, K. Riley, J. Gavvala, R. McGovern, S. Suresh, G. Chaitanya, and S. Thompson, "Stereoelectroencephalography of the Deep Brain: Basal Ganglia and Thalami," *Journal of Clinical Neurophysiology*, vol. 41, no. 5, pp. 423–429, 7 2024. [Online]. Available: https://journals.lww.com/clinicalneurophys/fulltext/2024/07000/stereoelectroencephalography_of_the_deep_brain_.7.aspx

[53] F. Pizzo, N. Roehri, B. Giusiano, S. Lagarde, R. Carron, D. Scavarda, A. McGonigal, C. Filipescu, I. Lambert, F. Bonini, A. Trebuchon, C. G. Bénar, and F. Bartolomei, "The Ictal Signature of Thalamus and Basal Ganglia in Focal Epilepsy: A SEEG Study," *Neurology*, vol. 96, no. 2, pp. e280–e293, 1 2021.

[54] I. Rektor, R. Kuba, M. Brázdil, and J. Chrastina, "Do the basal ganglia inhibit seizure activity in temporal lobe epilepsy?" *Epilepsy & Behavior*, vol. 25, no. 1, pp. 56–59, 9 2012.

[55] S. Miocinovic, C. de Hemptinne, W. Chen, F. Isbaine, J. T. Willie, J. L. Ostrem, and P. A. Starr, "Cortical Potentials Evoked by Subthalamic Stimulation Demonstrate a Short Latency Hyperdirect Pathway in Humans," *The Journal of Neuroscience*, vol. 38, no. 43, p. 9129, 10 2018. [Online]. Available: https://pmc.ncbi.nlm.nih.gov/articles/PMC6199405/

[56] S. L. Schmidt, D. T. Brocker, B. D. Swan, D. A. Turner, and W. M. Grill, "Evoked potentials reveal neural circuits engaged by human deep brain stimulation," *Brain Stimulation*, vol. 13, no. 6, pp. 1706–1718, 11 2020. [Online]. Available: http://www.brainstimjrnl.com/article/S1935861X20302679/fulltexthttp://www.brainstimjrnl.com/article/S1935861X20302679/abstracthttps://www.brainstimjrnl.com/article/S1935-861X(20)30267-9/abstract

[57] D. Zumsteg, A. M. Lozano, H. G. Wieser, and R. A. Wennberg, "Cortical activation with deep brain stimulation of the anterior thalamus for epilepsy," *Clinical Neurophysiology*, vol. 117, no. 1, pp. 192–207, 1 2006.

[58] R. Ramasubbu, S. Lang, and Z. H. Kiss, "Dosing of Electrical Parameters in Deep Brain Stimulation (DBS) for Intractable Depression: A Review of Clinical Studies," *Frontiers in Psychiatry*, vol. 9, no. JUL, p. 302, 7 2018. [Online]. Available: https://pmc.ncbi.nlm.nih.gov/articles/PMC6050377/

[59] W. Xu, G. S. Russo, T. Hashimoto, J. Zhang, and J. L. Vitek, "Subthalamic Nucleus Stimulation Modulates Thalamic Neuronal Activity," *Journal of Neuroscience*, vol. 28, no. 46, pp. 11 916–11 924, 11 2008. [Online]. Available: https://www.jneurosci.org/content/28/46/11916https://www.jneurosci.org/content/28/46/11916.abstract

[60] I. Osorio, J. Overman, J. Giftakis, and S. B. Wilkinson, "High Frequency Thalamic Stimulation for Inoperable Mesial Temporal Epilepsy," *Epilepsia*, vol. 48, no. 8, pp. 1561–1571, 8 2007. [Online]. Available: https://onlinelibrary.wiley.com/doi/full/10.1111/j.1528-1167.2007.01044.xhttps://onlinelibrary.wiley.com/doi/abs/10.1111/j.1528-1167.2007.01044.xhttps://onlinelibrary.wiley.com/doi/10.1111/j.1528-1167.2007.01044.x

[61] D. Purves, G. J. Augustine, D. Fitzpatrick, L. C. Katz, A.-S. LaMantia, J. O. McNamara, and S. M. Williams, "Increased Conduction Velocity as a Result of Myelination," 2001. [Online]. Available: https://www.ncbi.nlm.nih.gov/books/NBK10921/

[62] D. M. Goldenholz, S. P. Ahlfors, M. S. Hämäläinen, D. Sharon, M. Ishitobi, L. M. Vaina, and S. M. Stufflebeam, "Mapping the signal-to-noise-ratios of cortical sources in magnetoencephalography and electroencephalography," *Human Brain Mapping*, vol. 30, no. 4, pp. 1077–1086, 4 2009. [Online]. Available: https://onlinelibrary.wiley.com/doi/full/10.1002/hbm.20571https://onlinelibrary.wiley.com/doi/abs/10.1002/hbm.20571https://onlinelibrary.wiley.com/doi/10.1002/hbm.20571

[63] M. Hämäläinen, R. Hari, R. J. Ilmoniemi, J. Knuutila, and O. V. Lounasmaa, "Magnetoencephalography—theory, instrumentation, and applications to noninvasive studies of the working human brain," *Reviews of Modern Physics*, vol. 65, no. 2, p. 413, 4 1993. [Online]. Available: https://journals.aps.org/rmp/abstract/10.1103/RevModPhys.65.413

[64] N. B. Bangera, D. L. Schomer, N. Dehghani, I. Ulbert, S. Cash, S. Papavasiliou, S. R. Eisenberg, A. M. Dale, and E. Halgren, "Experimental validation of the influence of white matter anisotropy on the intracranial EEG forward solution," *Journal of Computational Neuroscience*, vol. 29, no. 3, pp. 371–387, 1 2010. [Online]. Available: https://link.springer.com/article/10.1007/s10827-009-0205-z

[65] W. H. Lee, Z. Liu, B. A. Mueller, K. Lim, and B. He, "Influence of white matter anisotropic conductivity on EEG source localization: Comparison to fMRI in human primary visual cortex," *Clinical Neurophysiology*, vol. 120, no. 12, pp. 2071–2081, 12 2009.

[66] S. Homölle and R. Oostenveld, "Using a structured-light 3D scanner to improve EEG source modeling with more accurate electrode positions," *Journal of Neuroscience Methods*, vol. 326, p. 108378, 10 2019.

Appendix A

EP latencies

This Appendix provides all tables including the manually selected EP latencies for all parameter configurations.

Table A.1: Latencies for each EP component across the contacts (implantation 1 at high amplitude)

	EP 1	EP 2	EP 3	EP 4
C0	8.25	19.5	48.5	71.25
C1	9.0	20.0	50.5	68.0
C2	7.25	20.0	40.25	87.5
C3	8.75	20.25	35.5	65.75

Table A.2: Latencies for each EP component across the contacts (implantation 1 at low amplitude)

	EP 1	EP 2	EP 3	EP 4
C0	9.5	20.0	58.5	69.5
C1	8.75	20.0	50.0	67.75
C2	9.75	22.0	47.75	72.0
C3	7.5	16.75	46.75	77.5

Table A.3: Latencies for each EP component across the contacts (implantation 3 at high amplitude)

	EP 1	EP 2	EP 3	EP 4
C0	3.0	38.5	53.0	116.0
C1	3.0	44.0	53.0	117.25
C2	5.75	38.0	77.0	109.0
C3	6.5	26.5	49.5	91.25

Table A.4: Latencies for each EP component across the contacts (implantation 4 at high amplitude)

	EP 1	EP 2	EP 3	EP 4
C0	3.75	21.5	40.5	93.5
C1	3.0	19.0	46.0	75.5
C2	9.25	21.0	48.25	103.5
C3	5.25	21.25	46.25	106.0

Table A.5: Latencies for each EP component across the contacts (implantation 4 at low amplitude)

	EP 1	EP 2	EP 3	EP 4
C0	3.0	19.0	48.75	103.0
C1	3.5	20.25	45.5	100.0
C2	4.75	23.0	42.5	98.0
C3	6.0	16.75	44.75	96.75

Appendix B

RV values

This appendix provides all tables that summarize the RV values for the reconstructed dipoles across all parameter configurations.

Table B.1: RV values for implantation 1 (high amplitude).

	EP 1	**EP 2**	**EP 3**	**EP 4**
C3	0.31	0.30	0.07	0.16
C2	0.04	0.10	0.27	0.12
C1	0.09	0.12	0.09	0.16
C0	0.06	0.10	0.05	0.19

Table B.2: RV values for implantation 1 (low amplitude).

	EP 1	**EP 2**	**EP 3**	**EP 4**
C3	0.43	0.29	0.42	0.19
C2	0.15	0.10	0.15	0.06
C1	0.13	0.43	0.16	0.07
C0	0.16	0.12	0.07	0.08

Table B.3: RV values for implantation 3 (high amplitude).

	EP 1	**EP 2**	**EP 3**	**EP 4**
C3	0.10	0.08	0.05	0.07
C2	0.09	0.04	0.25	0.17
C1	0.12	0.04	0.07	0.04
C0	0.37	0.49	0.54	0.33

Table B.4: RV values for implantation 3 (low amplitude).

	EP 1	**EP 2**	**EP 3**	**EP 4**
C3	0.16	0.04	0.11	0.28
C2	0.09	0.04	0.25	0.17
C1	0.12	0.04	0.07	0.04
C0	0.37	0.49	0.54	0.33

Table B.5: RV values for implantation 4 (high amplitude).

	EP 1	**EP 2**	**EP 3**	**EP 4**
C3	0.18	0.09	0.08	0.12
C2	0.14	0.15	0.05	0.10
C1	0.27	0.13	0.06	0.04
C0	0.23	0.08	0.06	0.07

Table B.6: RV values for implantation 4 (low amplitude).

	EP 1	**EP 2**	**EP 3**	**EP 4**
C3	0.16	0.12	0.15	0.07
C2	0.41	0.16	0.10	0.18
C1	0.22	0.23	0.10	0.25
C0	0.37	0.19	0.06	0.17

Appendix C

GMFP comparisons

This Appendix provides additional figures of GMFP plots, comparing high and low amplitude stimulation and stimulation across different contacts.

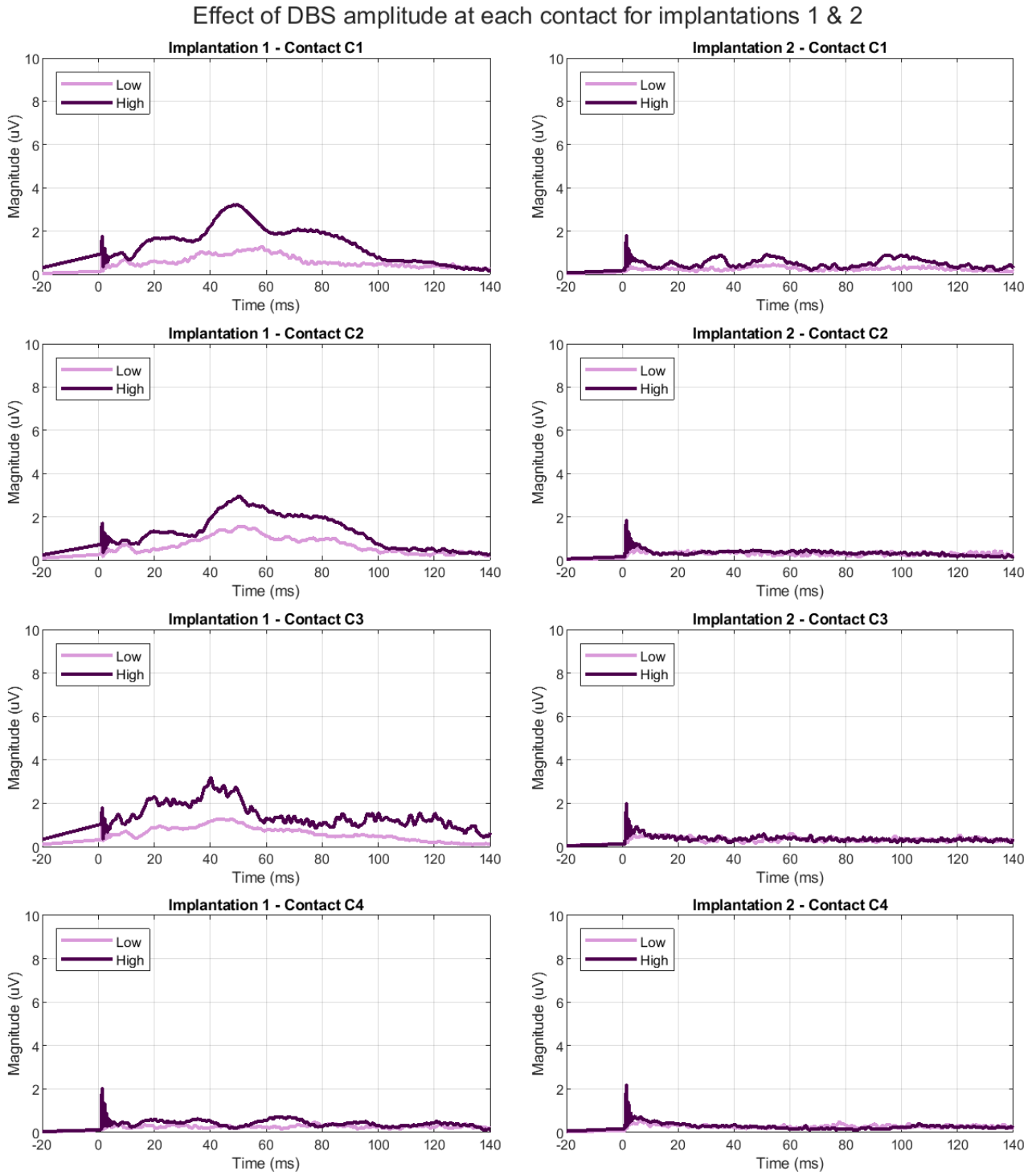

Figure C.1: Effect of DBS amplitude on evoked response across contacts (C0 to C3) for two separate implantation (same patient). Each plot compares the responses to high and low-amplitude stimulation over time (ms). Contacts C0 to C3 are arranged from deepest to most superficial.

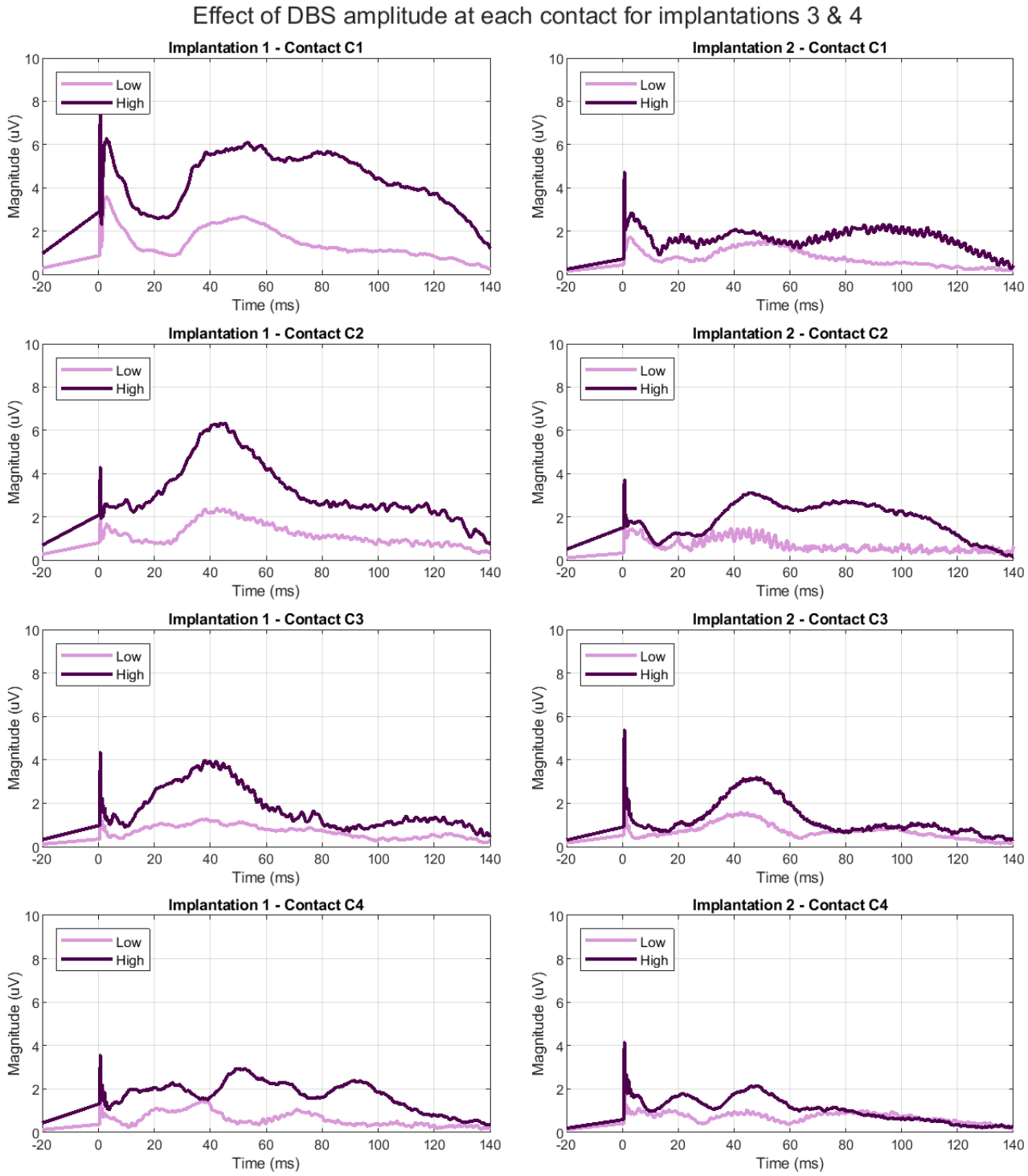

Figure C.2: Effect of DBS amplitude on evoked response across contacts (C0 to C3) for two separate implantation (same patient). Each plot compares the responses to high and low-amplitude stimulation over time (ms). Contacts C0 to C3 are arranged from deepest to most superficial.

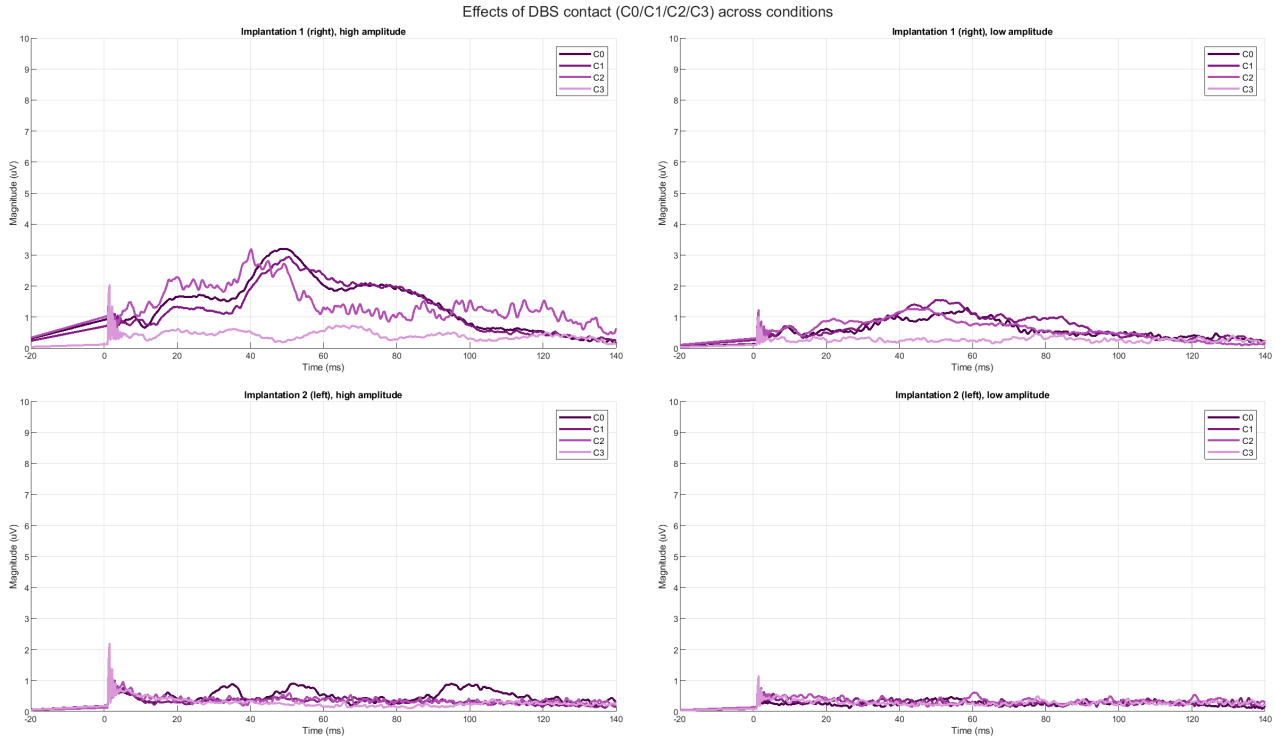

Figure C.3: Effects of DBS contact points (C0, C1, C2, C3) on the evoked response across different implantations and high/low amplitude (subject DBS011).

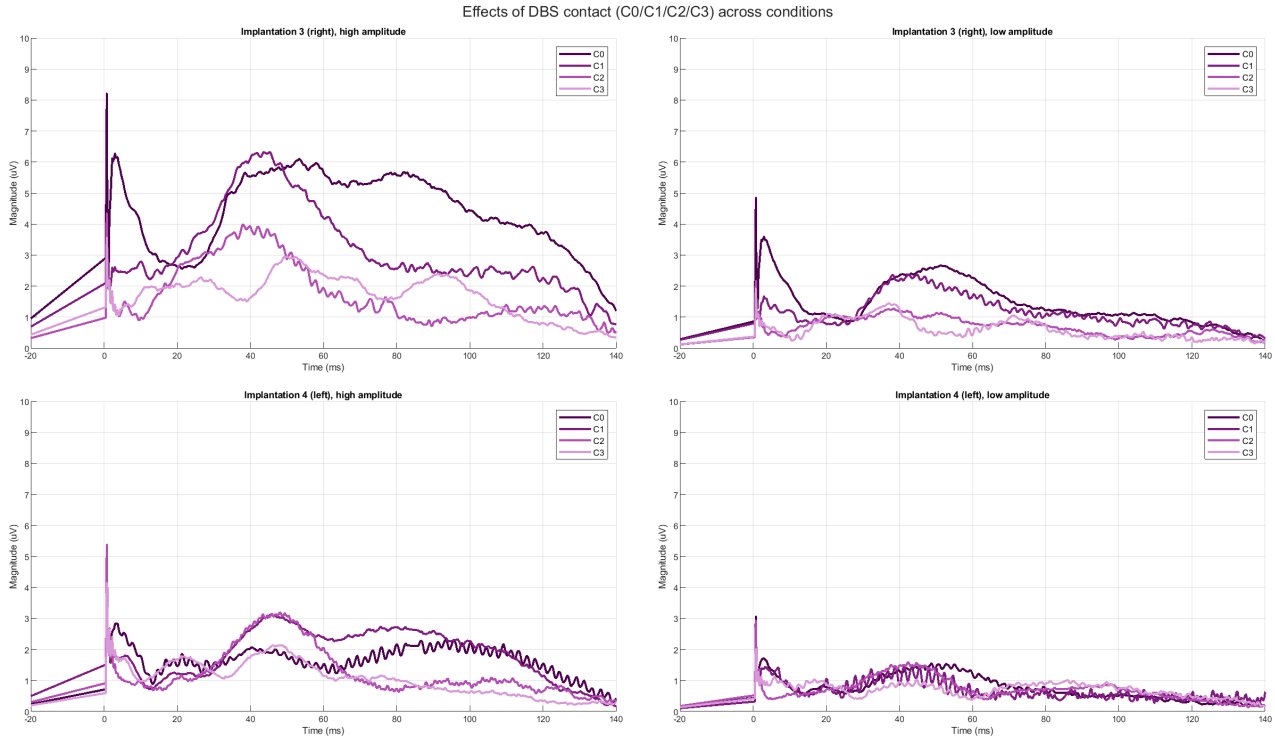

Figure C.4: Effects of DBS contact points (C0, C1, C2, C3) on the evoked response across different implantations and high/low amplitude (subject DBS014).

Appendix D

GMFP plots + topographical maps

This appendix provides additional figures of the GMFP plots and topographies at the corresponding contact and EP. The GMFP plot shows the amplitude of the responses over time for each contact (C0, C1, C2, and C3), with distinct intervals highlighting for EPs: 1 (red), 2 (green), 3 (blue), and 4 (yellow). Below the plot are the corresponding topographies for each EP across different contacts, demonstrating the spatial distribution of the activation on the scalp. It should be noted that the color scale is not fixed across the different topographic maps, resulting in variations in intensity representation. As a result, although the color patterns may visually appear comparable across maps, the actual intensity values are not directly comparable.

For implantation 2 (high amplitude, C1-C3 stimulation, and low amplitude), the GMFP amplitude is minimal, indicating that source reconstruction is unfeasible for these data.

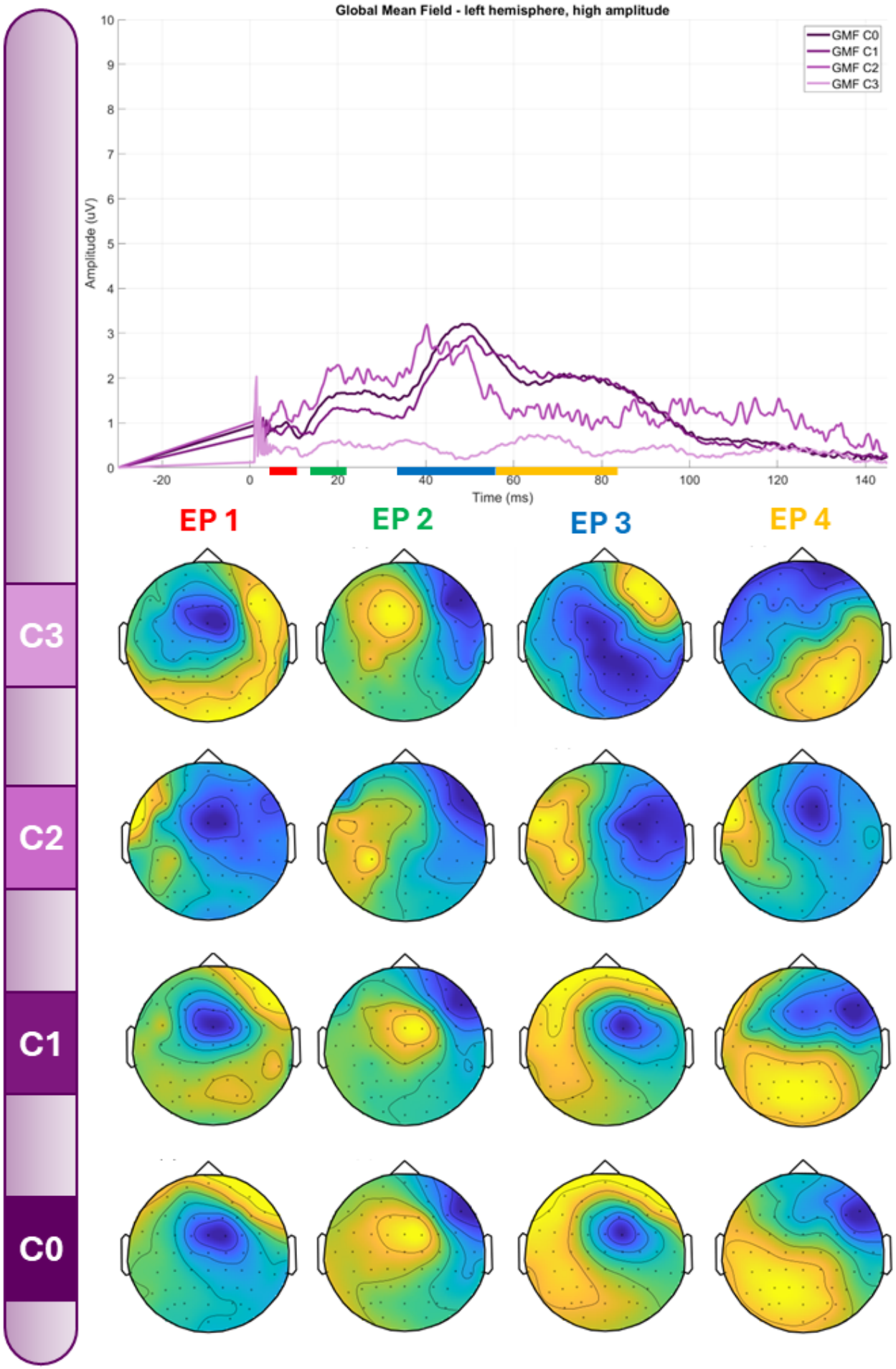

Figure D.1: GMFP plot and topographic maps of the EPs for implantation 1 (high amplitude).

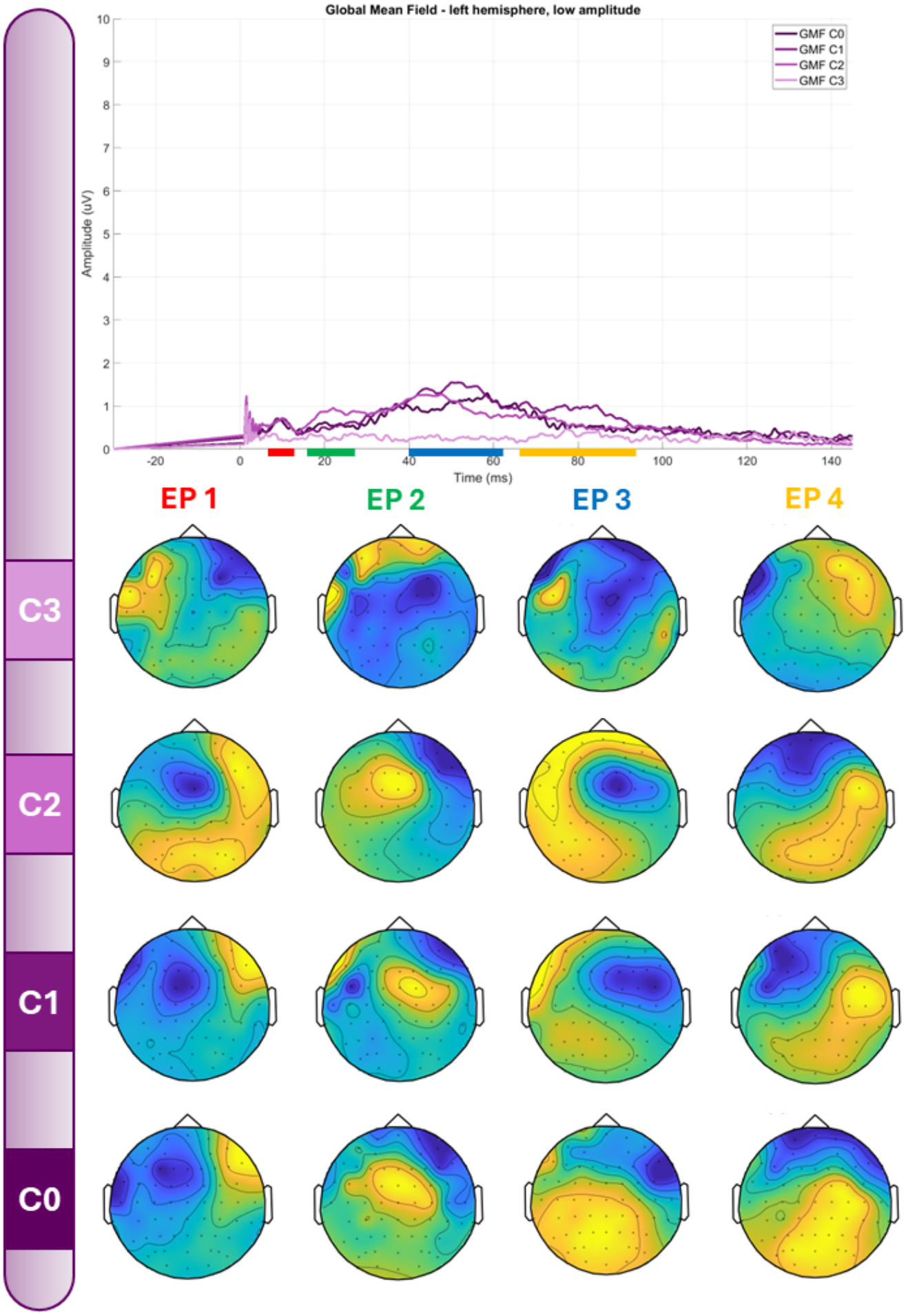

Figure D.2: GMFP plot and topographic maps of the EPs for implantation 1 (low amplitude).

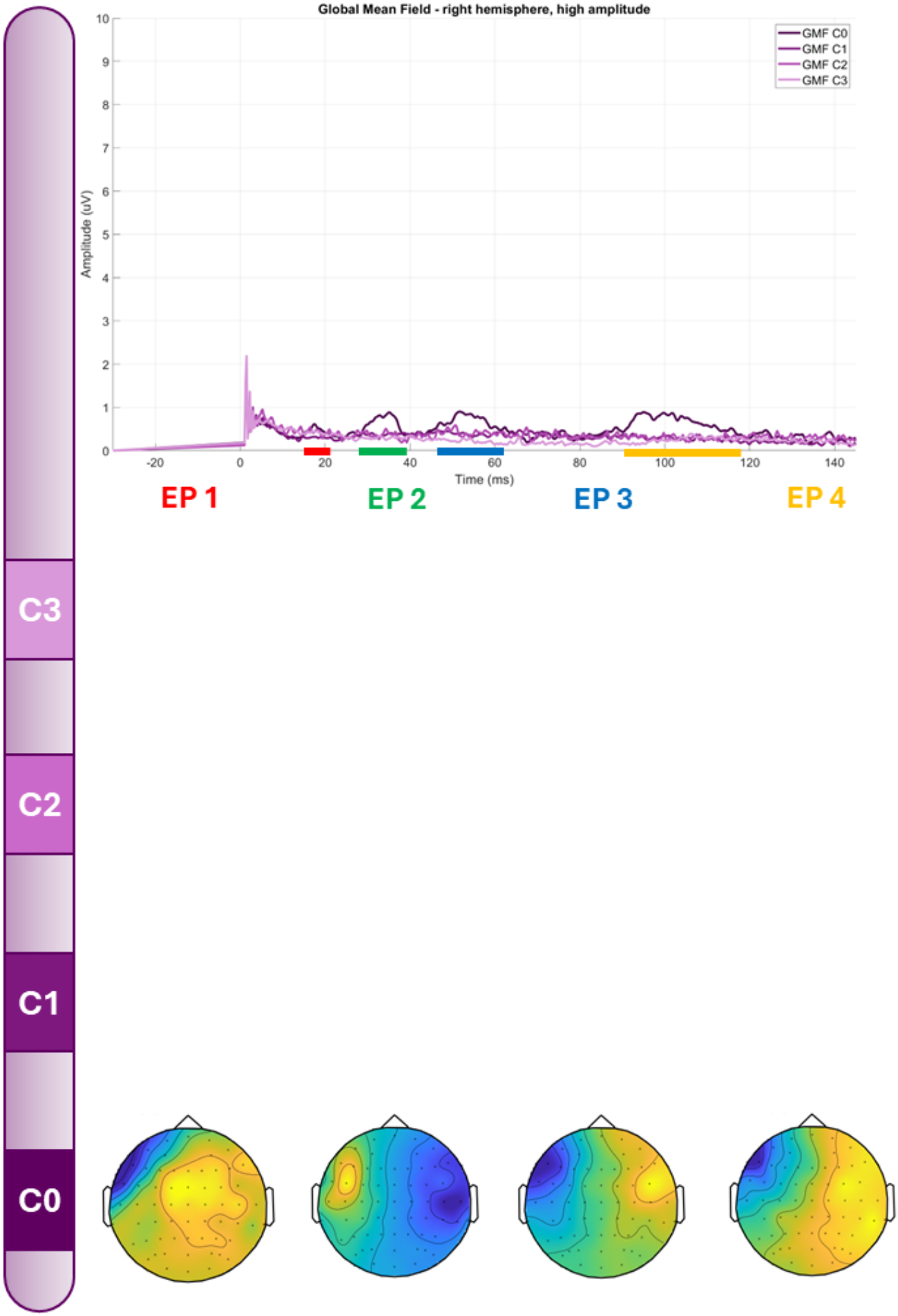

Figure D.3: GMFP plot and topographic maps of the EPs for implantation 2 (high amplitude).

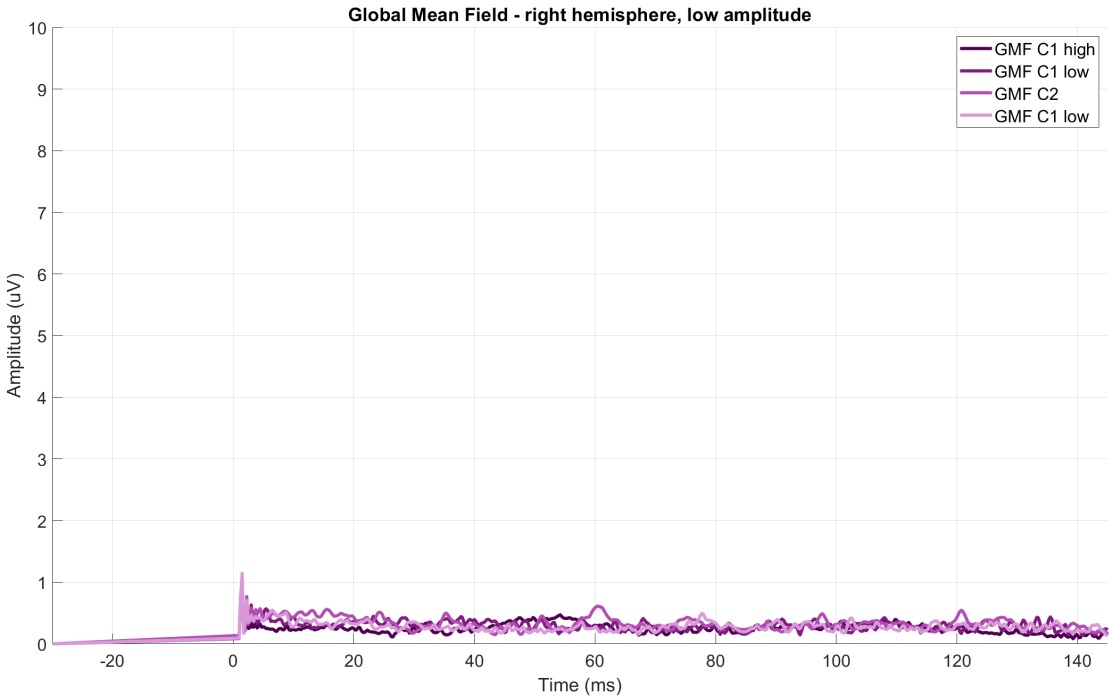

Figure D.4: GMFP plot for implantation 2 (low amplitude).

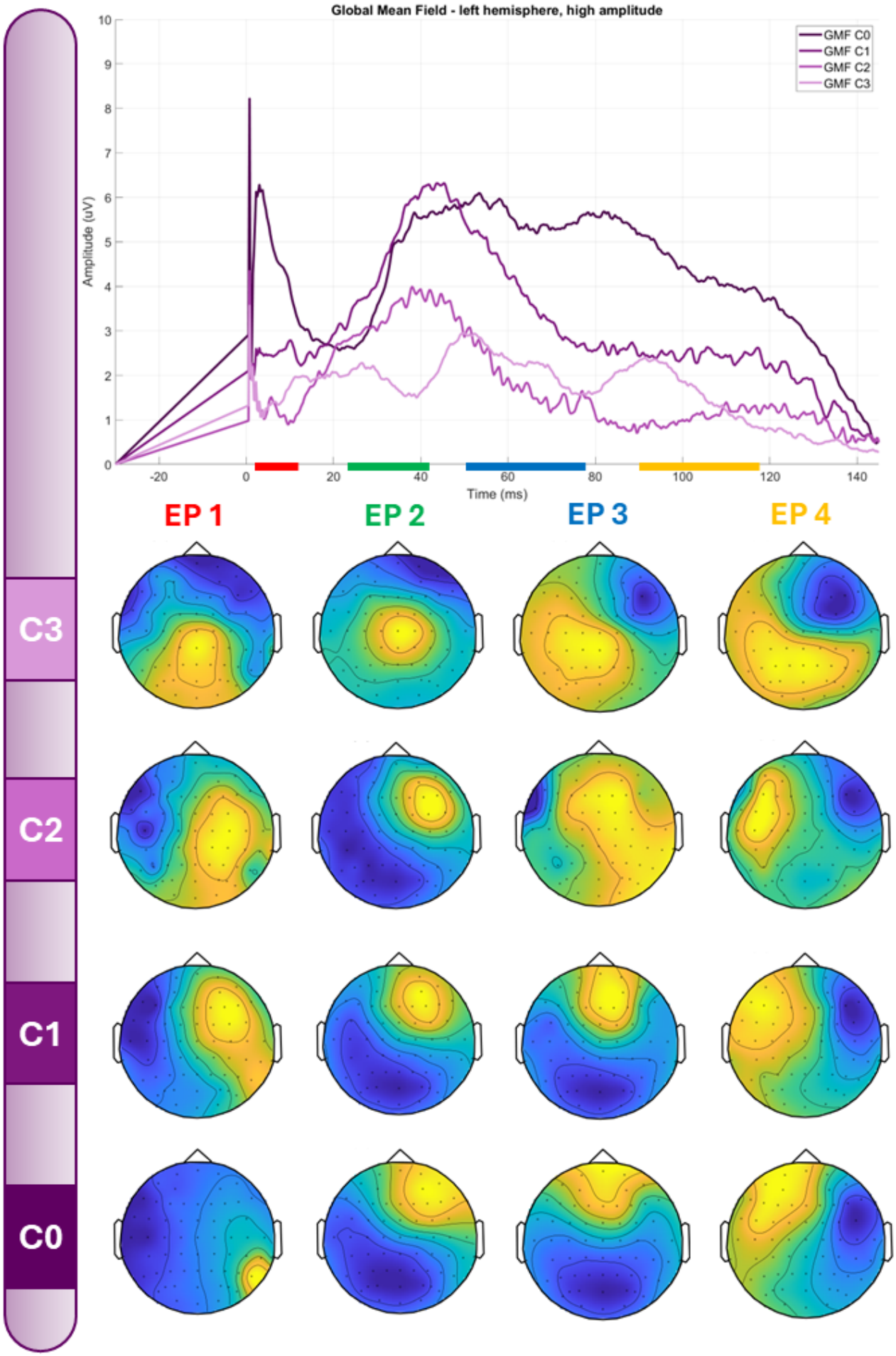

Figure D.5: GMFP plot and topographic maps of the EPs for implantation 3 (high amplitude).

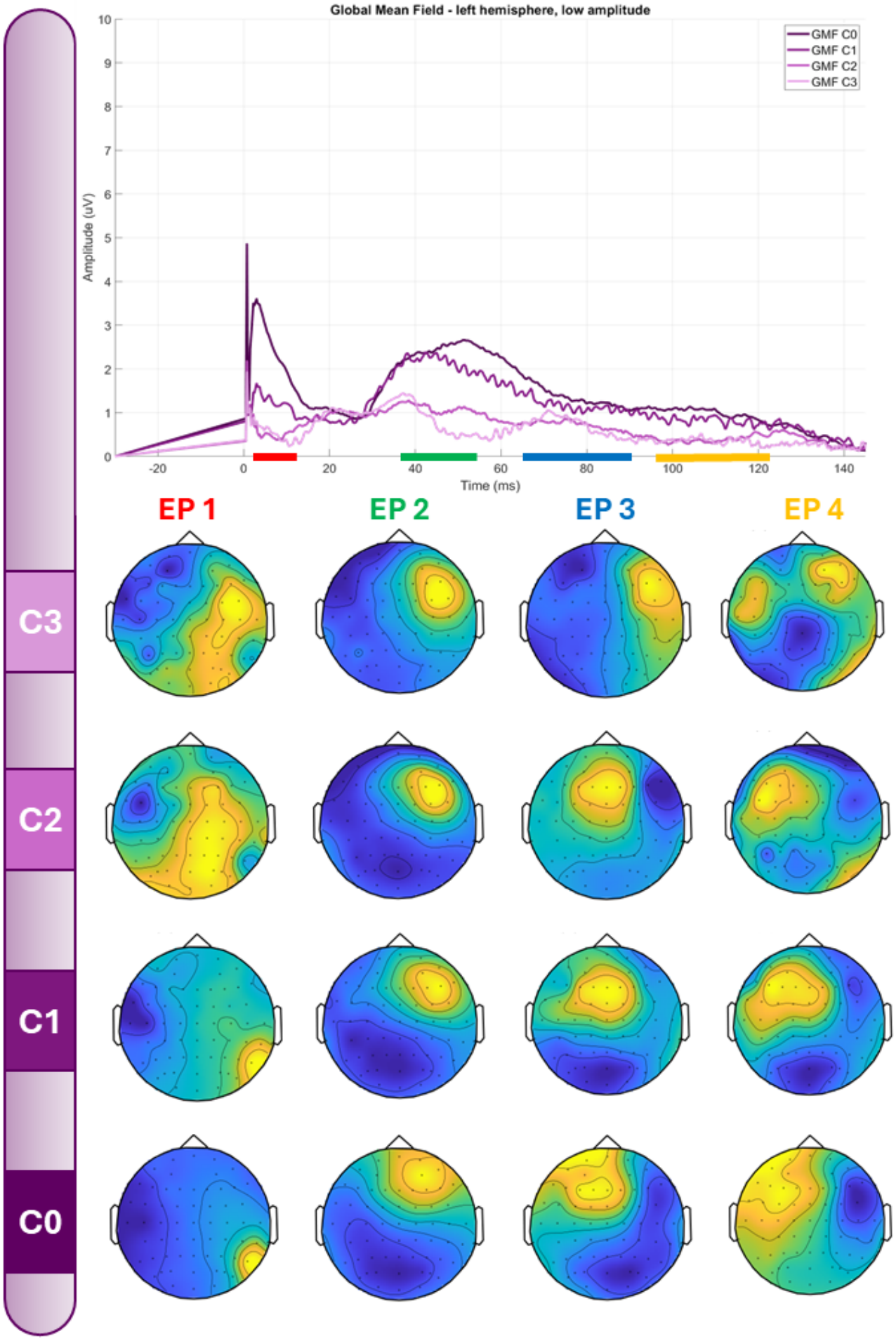

Figure D.6: GMFP plot and topographic maps of the EPs for implantation 3 (low amplitude).

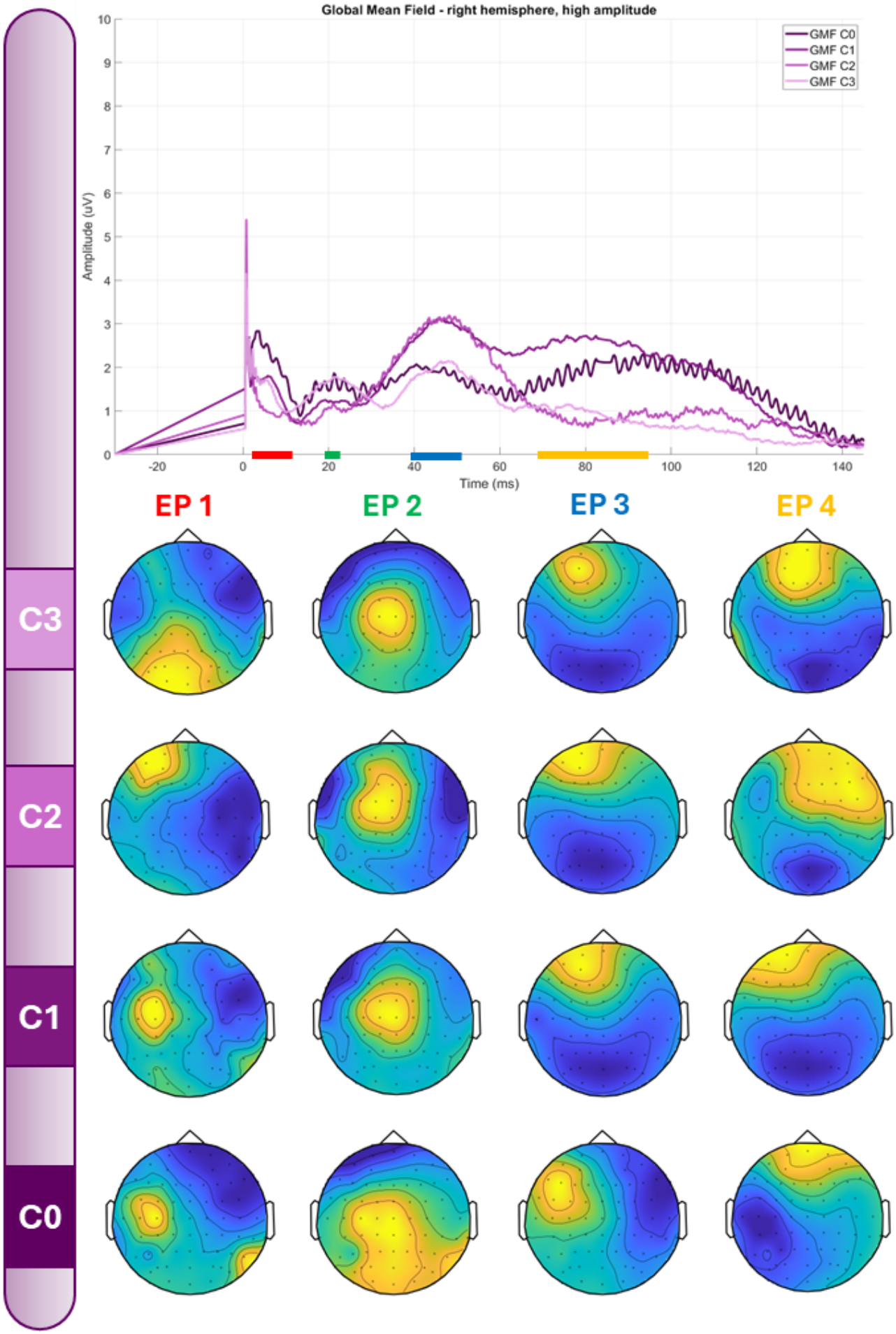

Figure D.7: GMFP plot and topographic maps of the EPs for implantation 4 (high amplitude).

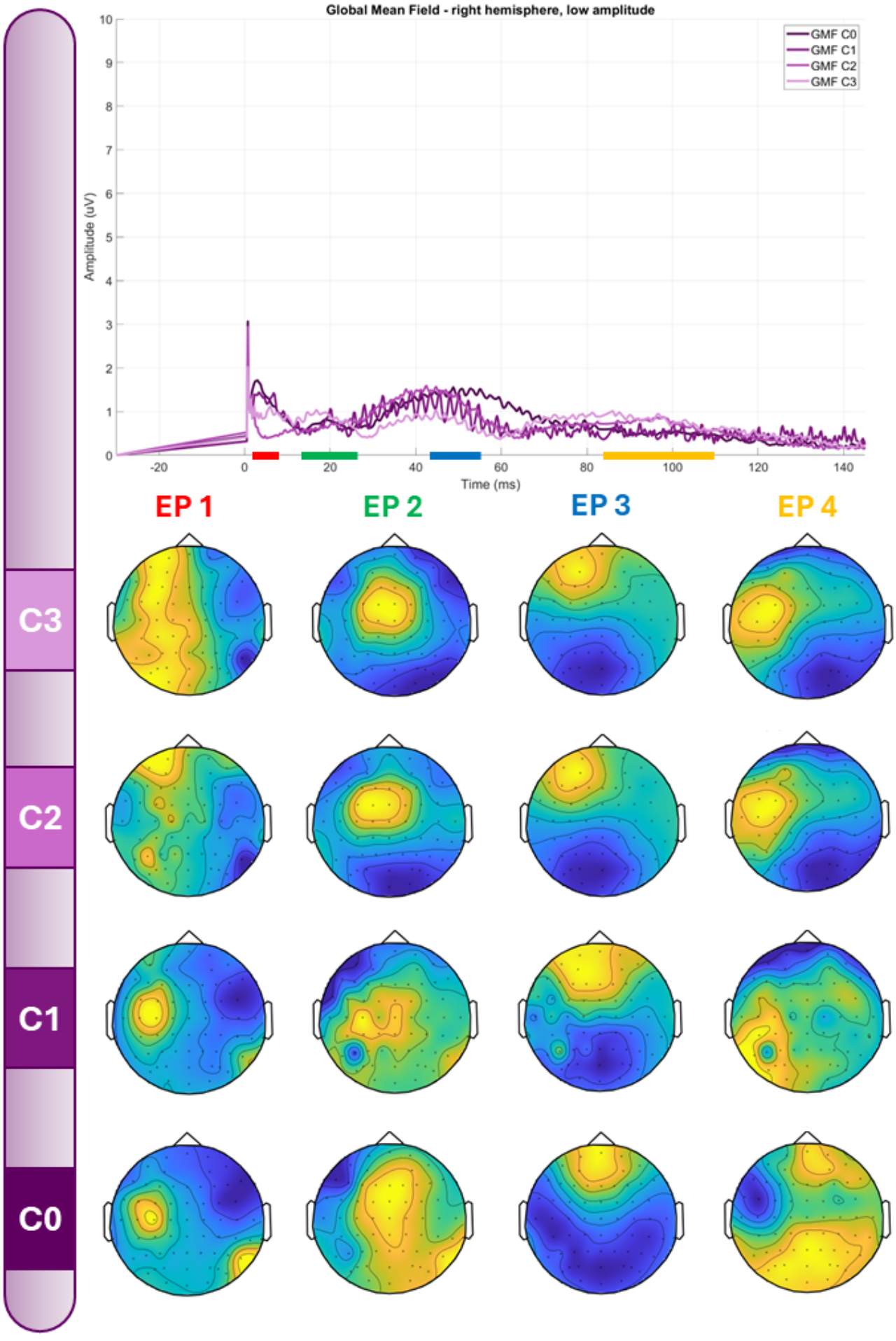

Figure D.8: GMFP plot and topographic maps of the EPs for implantation 4 (low amplitude).

Appendix E

Reconstructed Dipole Plots

This appendix provides additional plots, including the dipoles of each implantation (high and low amplitude). The color of the dipole (red-green-blue-yellow) corresponds to the EP (1-2-3-4), and the brightness (bright color to light color) corresponds to the contact (C0 to C3), as stated in Figure 3.7.

Dipole plots of each condition are available on GitHub (`https://github.com/jillbay/lowfrequency_DBS_epilepsy`). These figures are provided in MATLAB format, enabling 3D viewing and rotation when accessed through MATLAB.

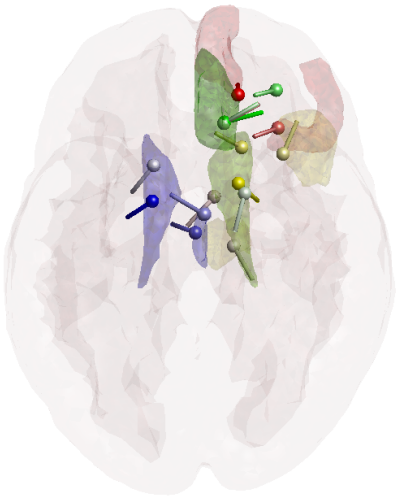

Figure E.1: 3D visualization of dipole sources for implantation 1 (high amplitude) within a brain mesh.

Figure E.2: 3D visualization of dipole sources for implantation 1 (low amplitude) within a brain mesh.

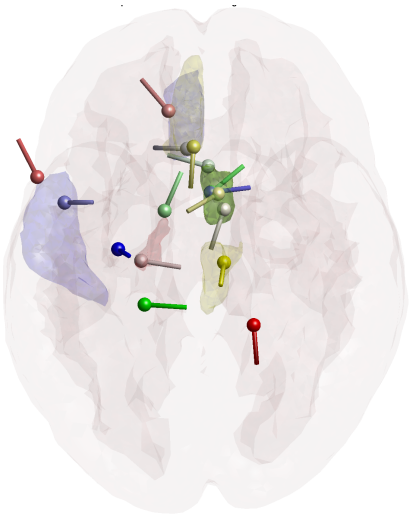

Figure E.3: 3D visualization of dipole sources for implantation 3 (high amplitude) within a brain mesh.

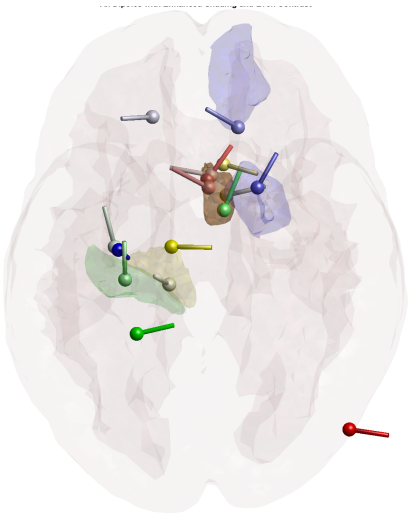

Figure E.4: 3D visualization of dipole sources for implantation 3 (low amplitude) within a brain mesh.

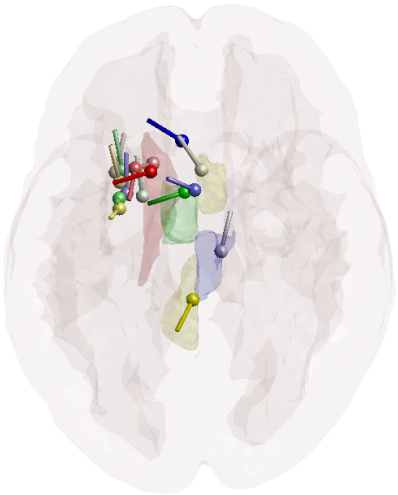

Figure E.5: 3D visualization of dipole sources for implantation 4 (high amplitude) within a brain mesh.

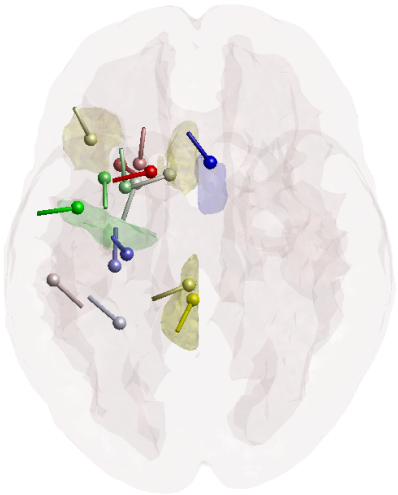

Figure E.6: 3D visualization of dipole sources for implantation 4 (low amplitude) within a brain mesh.

Appendix F

Anatomical Labels

This appendix provides additional tables with information regarding the anatomical labels of the reconstructed dipoles based on SimNIBS segmentation, FSL segmentation, and the Brainnetome atlas. The SimNIBS segmentation was included in the generation of the head model; the source model is based on this segmentation. The FSL segmentation was also included with the generation of the head model, providing more detailed tissue types. The Brainnetome atlas includes parcellations of cortical and subcortical structures.

Table F.1: Anatomical labels of the reconstructed dipole sources, corresponding to implantation 1 (high amplitude)

Contact	EP	SimNIBS	FSL Segmentation	Brainnetome Atlas
C0	**EP 1**	Gray Matter	Right Cerebral Cortex	Right Superior Frontal Gyrus, medial area 10
	EP 2	Gray Matter	Right Cerebral Cortex	Right Orbital Gyrus A12/47l, lateral area 12/47
	EP 3	Gray Matter	Right Cerebral Cortex	Right Superior Frontal Gyrus A9m, medial area 9
	EP 4	Gray Matter	Right Caudate	Right Basal Ganglia, nucleus accumbens
C1	**EP 1**	Gray Matter	Right Cerebral Cortex	Right Superior Frontal Gyrus A9m, medial area 9
	EP 2	Gray Matter	Right Cerebral Cortex	Right Middle Frontal Gyrus A46, area 46
	EP 3	Gray Matter	Right Cerebral Cortex	Right Superior Frontal Gyrus A9m, medial area 9
	EP 4	Gray Matter	Right Caudate	Right Basal Ganglia, dorsal caudate
C2	**EP 1**	Gray Matter	Left Lateral Ventricle	Left Basal Ganglia, dorsal caudate
	EP 2	Gray Matter	Left Thalamus	Right Thalamus, rostral temporal thalamus
	EP 3	Gray Matter	Right Cerebral WM	Right Thalamus, rostral temporal thalamus
	EP 4	Gray Matter	Left Caudate	Left Basal Ganglia, dorsal caudate
C3	**EP 1**	Gray Matter	Right Caudate	Right Basal Ganglia, dorsal caudate
	EP 2	Gray Matter	WM-hypointensities	Right Basal Ganglia, dorsal caudate
	EP 3	Gray Matter	Right Cerebral Cortex	Right Inferior Frontal Gyrus, opercular area 44
	EP 4	Gray Matter	Right Thalamus	Right Thalamus, pre-motor thalamus

Table F.2: Anatomical labels of the reconstructed dipole sources, corresponding to implantation 1 (low amplitude)

Contact	EP	SimNIBS	FSL Segmentation	Brainnetome Atlas
C0	**EP 1**	Gray Matter	Right Cerebral WM	Right Cingulate Gyrus A24rv, rostroventral area 24
	EP 2	Gray Matter	Right Cerebral Cortex	Right Superior Frontal Gyrus A10m, medial area 10
	EP 3	Gray Matter	Right Caudate	Right Basal Ganglia dCa, dorsal caudate
	EP 4	Gray Matter	Right Lateral Ventricle	Right Basal Ganglia dCa, dorsal caudate
C1	**EP 1**	Gray Matter	Right Cerebral WM	Right Cingulate Gyrus A24rv, rostroventral area 24
	EP 2	Gray Matter	Right Cerebral Cortex	Right Middle Frontal Gyrus A9/46d, dorsal area 9/46
	EP 3	Gray Matter	Right Caudate	Right Basal Ganglia dCa, dorsal caudate
	EP 4	Gray Matter	Right Cerebral Cortex	Right Cingulate Gyrus A24rv, rostroventral area 24
C2	**EP 1**	Gray Matter	Left Caudate	Left Cingulate Gyrus A24rv, rostroventral area 24
	EP 2	Gray Matter	Right Cerebral Cortex	Right Cingulate Gyrus A24rv, rostroventral area 24
	EP 3	Gray Matter	Right Cerebral Cortex	Right Superior Frontal Gyrus A9m, medial area 9
	EP 4	Gray Matter	Right Cerebral WM	Right Cingulate Gyrus A24rv, rostroventral area 24
C3	**EP 1**	Gray Matter	Right Cerebral WM	Right Superior Temporal Gyrus A38l, lateral area 38
	EP 2	Gray Matter	Left Cerebral Cortex	Left Cingulate Gyrus A32sg, subgenual area 32
	EP 3	Gray Matter	Right Cerebral Cortex	Right Cingulate Gyrus A32sg, subgenual area 32
	EP 4	Gray Matter	Left Cerebral Cortex	Left Orbital Gyrus A11m, medial area 11

Table F.3: Anatomical labels of the reconstructed dipole sources, corresponding to implantation 3 (high amplitude)

Contact	EP	SimNIBS	FSL Segmentation	Brainnetome Atlas
C0	**EP 1**	Gray Matter	Right Thalamus	Right Thalamus PPtha, posterior parietal thalamu
	EP 2	Gray Matter	Cortical CSF	BG, Left Superior Temporal Gyrus A38l, lateral are
	EP 3	Gray Matter	Cortical CSF	Left Cingulate Gyrus A32p, pregenual area 32
	EP 4	Gray Matter	Left Amygdala	Left Amygdala mAmyg, medial amygdala
C1	**EP 1**	Gray Matter	Left Thalamus	Left Thalamus PPtha, posterior parietal thalamu
	EP 2	Gray Matter	Right Lateral Ventricle	Right Basal Ganglia dCa, dorsal caudate
	EP 3	Gray Matter	Left Cerebral Cortex	Left Cingulate Gyrus A24rv, rostroventral area 2
	EP 4	Gray Matter	Right Cerebral WM	Right Basal Ganglia dCa, dorsal caudate
C2	**EP 1**	Gray Matter	Left Caudate	Left Basal Ganglia dCa, dorsal caudate
	EP 2	Gray Matter	Right Lateral Ventricle	Right Basal Ganglia dCa, dorsal caudate
	EP 3	Gray Matter	Cortical CSF	Left Insular Gyrus vId/vIg, ventral dysgranular and granu
	EP 4	Gray Matter	Right Cerebral Cortex	Right Cingulate Gyrus A24rv, rostroventral area
C3	**EP 1**	Gray Matter	Right Caudate	Right Basal Ganglia dCa, dorsal caudate
	EP 2	Gray Matter	Right Cerebral Cortex	Right Cingulate Gyrus A24rv, rostroventral area
	EP 3	Gray Matter	Right Caudate	Right Basal Ganglia dCa, dorsal caudate
	EP 4	Gray Matter	Right Caudate	Right Basal Ganglia dCa, dorsal caudate

Table F.4: Anatomical labels of the reconstructed dipole sources, corresponding to implantation 3 (low amplitude)

Contact	EP	SimNIBS	FSL Segmentation	Brainnetome Atlas
C0	**EP 1**	Gray Matter	Right Cerebellum Cortex	No label found within radius
	EP 2	Gray Matter	Right Caudate	Right Basal Ganglia dCa, dorsal caudate
	EP 3	Gray Matter	Right Cerebral WM	Right Basal Ganglia dCa, dorsal caudate
	EP 4	Gray Matter	Right Cerebral WM	Right Basal Ganglia dCa, dorsal caudate
C1	**EP 1**	Gray Matter	Cortical CSF	No label found within radius
	EP 2	Gray Matter	Right Caudate	Right Basal Ganglia dCa, dorsal caudate
	EP 3	Gray Matter	Left Cerebral WM	Left Cingulate Gyrus A23c, caudal area 23
	EP 4	Gray Matter	Left Caudate	Right Basal Ganglia dCa, dorsal caudate
C2	**EP 1**	Gray Matter	Left Caudate	Left Basal Ganglia dCa, dorsal caudate
	EP 2	Gray Matter	Right Cerebral Cortex	Right Middle Frontal Gyrus IFJ, inferior frontal junctio
	EP 3	Gray Matter	Right Cerebral Cortex	Right Middle Frontal Gyrus A9/46d, dorsal area 9/46
	EP 4	Gray Matter	Left Cerebral Cortex	Left Cingulate Gyrus A32p, pregenual area 32
C3	**EP 1**	Gray Matter	Left Thalamus	Left Thalamus rTtha, rostral temporal thalamus
	EP 2	Gray Matter	Right Caudate	Right Basal Ganglia dCa, dorsal caudate
	EP 3	Gray Matter	Right Caudate	Right Basal Ganglia dCa, dorsal caudate
	EP 4	Gray Matter	Right Cerebral Cortex	Right Cingulate Gyrus A23c, caudal area 23

Table F.5: Anatomical labels of the reconstructed dipole sources, corresponding to implantation 4 (high amplitude)

Contact	EP	SimNIBS	FSL Segmentation	Brainnetome Atlas
C0	**EP 1**	Gray Matter	Left Cerebral Cortex	Left Cingulate Gyrus A24rv, rostroventral area 24
	EP 2	Gray Matter	Left Caudate	Left Basal Ganglia dCa, dorsal caudate
	EP 3	Gray Matter	Left Caudate	Left Basal Ganglia vCa, ventral caudate
	EP 4	Gray Matter	Left Putamen	Left Basal Ganglia GP, globus pallidus
C1	**EP 1**	Gray Matter	Right Cerebral Cortex	Right Cingulate Gyrus A24rv, rostroventral area 24
	EP 2	Gray Matter	Left Cerebral WM	Left Basal Ganglia dCa, dorsal caudate
	EP 3	Gray Matter	Left Caudate	Left Basal Ganglia dCa, dorsal caudate
	EP 4	Gray Matter	Left Caudate	Left Basal Ganglia dCa, dorsal caudate
C2	**EP 1**	Gray Matter	Cortical CSF	Right Cingulate Gyrus A24rv, rostroventral area 24
	EP 2	Gray Matter	Right Cerebral Cortex	Right Cingulate Gyrus A24cd, caudodorsal area 24
	EP 3	Gray Matter	Left Caudate	Left Basal Ganglia dCa, dorsal caudate
	EP 4	Gray Matter	Right Caudate	Right Basal Ganglia dCa, dorsal caudate
C3	**EP 1**	Gray Matter	Cortical CSF	Right Thalamus rTtha, rostral temporal thalamus
	EP 2	Gray Matter	Left Caudate	Left Basal Ganglia dCa, dorsal caudate
	EP 3	Gray Matter	Left Caudate	Left Basal Ganglia dCa, dorsal caudate
	EP 4	Gray Matter	Right Caudate	Right Basal Ganglia dCa, dorsal caudate

Table F.6: Anatomical labels of the reconstructed dipole sources, corresponding to implantation 4 (low amplitude)

Contact	EP	SimNIBS	FSL Segmentation	Brainnetome Atlas
C0	**EP 1**	Gray Matter	Left Cerebral Cortex	Left Cingulate Gyrus A24rv, rostroventral area 24
	EP 2	Gray Matter	Left Caudate	Left Basal Ganglia dCa, dorsal caudate
	EP 3	Gray Matter	Left Caudate	Left Basal Ganglia dCa, dorsal caudate
	EP 4	Gray Matter	Left Cerebral Cortex	Left Inferior Parietal Lobule A40rv, rostroventral area 40
C1	**EP 1**	Gray Matter	Left Cerebral Cortex	Left Middle Frontal Gyrus A6vl, ventrolateral area
	EP 2	Gray Matter	Left putamen	Left Basal Ganglia dlPu, dorsolateral putamen
	EP 3	Gray Matter	Left Caudate	Left Basal Ganglia dCa, dorsal caudate
	EP 4	Gray Matter	Left Putamen	Left Basal Ganglia NAC, nucleus accumbens
C2	**EP 1**	Gray Matter	Right Caudate	Right Basal Ganglia dCa, dorsal caudate
	EP 2	Gray Matter	Left Cerebral Cortex	Left Cingulate Gyrus A23c, caudal area 23
	EP 3	Gray Matter	Left Caudate	Left Basal Ganglia dCa, dorsal caudate
	EP 4	Gray Matter	Left Lateral Ventricle	Left Hippocampus cHipp, caudal hippocampus
C3	**EP 1**	Gray Matter	Cortical CSF	Right Thalamus rTtha, rostral temporal thalamus
	EP 2	Gray Matter	Right Thalamus	Right Thalamus rTtha, rostral temporal thalamus
	EP 3	Gray Matter	Left Cerebral WM	Left Inferior Frontal Gyrus A44op, opercular area 4
	EP 4	Gray Matter	Right Cerebral Cortex	Right Cingulate Gyrus A24rv, rostroventral area 24